Advanced Patterning Process Developments for Various Optical Applications

by

Shinhyuk Choi

A Dissertation Presented in Partial Fulfillment
of the Requirements for the Degree
Doctor of Philosophy

Approved November 2022 by the
Graduate Supervisory Committee:

Chao Wang, Chair
Hongbin Yu
Zachary Holman
Yoon Hwa

ARIZONA STATE UNIVERSITY

December 2022

ABSTRACT

Patterning technologies for micro/nano-structures have been essentially used in a variety of discipline research areas, including electronics, optics, material science, and biotechnology. Therefore their importance has dramatically increased over the past decades.

This dissertation presents various advanced patterning processes utilizing cross-discipline technologies, e.g., photochemical deposition, transfer printing (TP), and nanoimprint lithography (NIL), to demonstrate inexpensive, high throughput, and scalable manufacturing for advanced optical applications.

The polymer-assisted photochemical deposition (PPD) method is employed in the form of additive manufacturing (AM) to print ultra-thin (< 5 nm) and continuous film in micro-scaled (> 6.5 μm) resolution. The PPD film acts as a lossy material in the Fabry-Pérot cavity structures and generates vivid colored images with a micro-scaled resolution by inducing large modulation of reflectance. This PPD-based structural color printing performs without photolithography and vacuum deposition in ambient and room-temperature conditions, which enables an accessible and inexpensive process (Chapter 1).

In the TP process, germanium (Ge) is used as the nucleation layer of noble metallic thin films to prevent structural distortion and improve surface morphology. The developed Ge-assisted transfer printing (GTP) demonstrates its feasibility transferring sub-100 nm features with up to 50 nm thickness in a centimeter scale. The GTP is also capable of transferring arbitrary metallic nano-apertures with minimal pattern distortion, providing relatively less expensive, simpler, and scalable manufacturing (Chapter 2).

NIL is employed to fabricate the double-layered chiral metasurface for polarimetric imaging applications. The developed NIL process provides multi-functionalities with a single NIL, i.e., spacing layer, planarized surface, and formation of dielectric gratings, respectively, which significantly reduces fabrication processing time and potential cost by eliminating several steps in the conventional fabrication process. During the integration of two metasurfaces, the Moiré fringe based alignment method is employed to accomplish the alignment accuracy of less than 200 nm in both x- and y-directions, which is superior to conventional photolithography. The dramatically improved optical performance, e.g., highly improved circular polarization extinction ratio (CPER), is also achieved with the developed NIL process (Chapter 3).

DEDICATION

To my father, with Love.

ACKNOWLEDGMENTS

First, I greatly appreciate Prof. Chao Wang, who brought me to open a new path in my research life. In the past five years, I have benefitted much from his appropriate advice, guidance to unknown research areas, encouragement, and continuous financial support. This dissertation would only be completed with those helps.

I sincerely appreciate Prof. Yu Yao for her continuous support and valuable advice in conducting research. I also appreciate the guidance of my Ph.D. committee members, Prof. Hongbin Yu, Prof. Zachary Holman, and Prof. Yoon Haw.

I appreciate many help from my group members. Jiawei Zuo greatly helped me with spectrometer measurements, FDTD simulation, and polarimetric imaging project. Dr. Pengkun Xia helped me with cleanroom work. Dr. Xiahui Chen trained me on the nanoimprinter. Dr. Zhi Zhao gave me proper comments when I struggled with metal printing. Dr. MD Ashif Ikbal helped me to maintain lab supplies. Also, thanks to other members, Jing Bai, Hossain Mansur Resalat Faruque, and Nabasindhu Das, in Prof. Yu Yao`s group.

Many of ASU`s core facilities members, including Carrie Sinclair, Kevin Nordquist, Scott Ageno, Jaime Quintero, Arthur Handugan, and Diana Convey, have helped me a lot in the past years. I also appreciate Dr. Roland Himmelhuber at the University of Arizona for training and help in NIL mold fabrication.

My parents and parents-in-law deserve my deepest appreciation. Their endless love, encouragement, and support have always been together, even across the ocean. Lastly, I would like to express my deepest appreciation to my lovely wife, Jooyoung Kim, for her

love, support, and dedication throughout my Ph.D. study. Being with her, I have finally reached the finale of my dissertation without frustration or giving up.

TABLE OF CONTENTS

Page

LIST OF TABLES ix

LIST OF FIGURES x

CHAPTER

1 INTRODUCTION..........1

2 STRUCTURAL COLOR PRINTING VIA POLYMER-ASSISTED PHOTOCHEMICAL DEPOSITION 3

2.1 Abstract 3

2.2 Introduction 4

2.3 Results 7

2.4 Discussion 24

2.5 Materials and methods 25

2.5.1 Materials 25

2.5.2 Preparation of Ag Printing Precursor..........25

2.5.3 Preparation of Substrates..........26

2.5.4 Ag and SiO_2 Film Deposition 27

2.5.5 FP Cavity-based Structural Color Printing Using PPD..........27

2.5.6 Film Characterization..........28

2.5.7 Simulation..........29

2.5.8 Effective Medium Theory..........30

2.6 References 31

CHAPTER Page

3 GE-ASSISTED TRANSFER PRINTING (GTP) OF METALLIC APERTURES FOR OPTICAL APPLICATIONS 37

3.1 Introduction 37

3.2 Effect of Ge on Metallic Thin Film 39

3.3 GTP Process for Metallic Nano-apertures 40

3.4 Demonstration of GTP 43

3.4.1 Nano-gratings for Silver (Ag) Transfer 43

3.4.2 Nano-gratings for Gold (Au) Transfer 45

3.5 GTP for Arbitrary Bow-tie Nano-aperture 47

3.5.1 Dielectric Nano-aperture Fabrication 47

3.5.2 Characterization of Transferred Ag Nano-aperture 49

3.6 Summary 52

4 SCALABLE MANUFACTURING FOR ULTRA-COMPACT POLARIMETRIC IMAGING SYSTEM USING NANOIMPRINT LITHOGRAPHY 53

4.1 Introduction 53

4.2 Chip-Integrated Polarimetric CMOS Imaging Sensor 56

4.3 Multi-Functional-Direct Nanoimprint Lithography (MFD-NIL) 57

4.4 Mold Fabrication for NIL 60

4.4.1 Mold for a-Si Metasurface 60

4.4.2 Mold for Vertically Coupled Al Double-layered Gratings (VCADGs) 61

4.5 Fabrication of Metasurfaces Using NIL 63
4.5.1 a-Si Metasurface by T-NIL 63
4.5.2 VCADGs by UV-NIL 67
4.5.2.1 MFD-NIL 67
4.5.2.2 Al Thickness Optimization 70
4.6 Uniformity of Fabricated Metasurfaces 72
4.7 Integration of Double-Layered Chiral Metasurface (DLCM) 74
4.7.1 Introduction – Moiré Fringe 74
4.7.2 Metasurface Alignment Using Moiré Fringe 76
4.8 Characterization of Integrated DLCM 79
4.9 Summary 85
5 CONCLUSION 86
REFERENCES 89
APPENDIX
A SUPPLEMENTARY FIGURES FOR CHAPTER 2 96
B COLOR RETENTION TIME TESTS 101
C EFFECTIVE MEDIUM THEORY 104
D BONDING PROCESS DEVELOPMENT FOR CMOS INTEGRATION 110
E PERMISSION FOR PREVIOUSLY PUBLISHED WORK IN A CULMINATING EXPERIENCE DOCUMENT 113

LIST OF TABLES

Table Page

4.1 Total Estimated Fabrication Processing Time for DLCM Structures 59

4.2 Measured Linewidth Dimensions for Uniformity Study................................73

4.3 Measured Gap Dimensions for Alignment Study 78

LIST OF FIGURES

Figure Page

2.1 Structural Color Printing (SCP) Technology 7

2.2 Structural and Optical Characterization of Polymer-Assisted Chemical Deposition (PPD) Printed Ultra-Thin Film...9

2.3 FDTD Simulated Reflectance Spectra for Design of Structural Colors 14

2.4 Experimental Demonstrations of Color Printing with Micro-Meter Resolution 17

2.5 Demonstration of Feasibility of Printing Complex Structures with Various Colors 19

2.6 Photolithography and Vacuum-Free SCP...21

3.1 Effect of Ge Nucleation Layer on Ag Thin Film..40

3.2 Ge-Assisted Transfer Printing (GTP) 42

3.3 Demonstration of GTP: Ag Nano-gratings...43

3.4 SEM Images of Ag Nano-gratings on Donor & Acceptor Substrates 44

3.5 Demonstration of GTP: Au Nano-gratings...46

3.6 Fabrication Flow for Dielectric Bow-tie Nano-apertures................................47

3.7 Demonstration of GTP: Ag Nano-apertures & Surface Morphology Characterization...49

3.8 SEM Images of Various Metallic Structures Fabricated via GTP 50

3.9 FDTD Simulated & Measured Tansmittance 51

4.1 Chip-Integrated Polarimetric CMOS Imaging Sensor 56

Figure Page

4.2 Multi-Functional-Direct Nanoimprint Lithography (MFD-NIL) for Fabrication of Double-Layered Chiral Metasurface (DLCM) 57

4.3 Mold Fabrication for a-Si Metasurface 60

4.4 Mold Fabrication for Vertically Coupled Al Double-layered Gratings (VCADGs) 62

4.5 Effect of MESA Structure on NIL 63

4.6 a-Si Metasurface Fabrication Using Thermal NIL with Tri-layer Structure ..65

4.7 SEM images for Individual Steps of T-NIL Process 66

4.8 VCADG Fabrication Using Ultra-Violet NIL 67

4.9 Measured Refractive Index of SiO_2 and UV Resist 68

4.10 Effect of Chamber Base Pressure on VCADG Surface Morphology 70

4.11 Experimentally Measured Transmission Efficiency & LPER of VCADG with Various Al Thicknesses 71

4.12 Photographic & SEM Images of Fabricated Metasurfaces for Uniformity Study 72

4.13 Moiré Fringe Based Alignment Technique for DLCM 76

4.14 Processed Microscopic Images for Alignment Study 77

4.15 Integrated DLCM using MFD-NIL 80

4.16 FDTD Simulated & Measured Transmission Efficiency, LPER, and CPER of RCP detector 82

4.17 Measured Transmission Efficiency and CPER of LCP detector 82

4.18 SEM Images of DLCM Integrated by NIL & EBL 83

Figure Page

4.19 Cross-Sectional SEM Images of VCADG 84

A.1 Structure Dependent Printing Behavior 97

A.2 Characterization of the Printed PPD Film 98

A.3 FDTD Simulation of the Printed PPD Film 98

A.4 FDTD Simulated Reflectance Spectra for Structural Colors 99

A.5 Time-Dependent Characteristics of the PPD Reflector 99

A.6 Characterization of the PPD Reflector 100

A.7 Measured Refractive Index of SiO_2 and PMMA 100

B.1 Effect of Encapsulation Layer on Color Retention Time 103

C.1 Size-Dependent Complex Permittivity of Spherical AgNPs 106

C.2 Measured and Calculated Effective Permittivity 108

C.3 Effect of pAAm Concentration on PPD Film 108

D.1 Developed CMOS Bonding Process 112

CHAPTER 1

INTRODUCTION

In this dissertation, the development process of various advanced patterning technologies will be presented with practical optical applications for each of them.

Chapter 2 studies a new way of structural color printing (SCP) application using the polymer-assisted photochemical deposition (PPD) process. The printed PPD films are examined with a variety of methodology techniques, i.e., scanning electron microscopy (SEM), atomic force microscopy (AFM), and ultra-violet (UV) visible (Vis) spectrometer, to investigate their optical and morphological characteristics. The finite-difference time-domain (FDTD) simulations are conducted using the extracted optical properties of PPD film to design Fabry-Pérot cavity structures for SCP. Based on the design parameters, SCP is performed on the prepared substrates, and the resolution and quality of colored structures are examined using various methodologies. The SCP is also carried out with complex structures on the rigid and flexible substrates to demonstrate its versatility and capability of generating colors.

Chapter 3 presents the advanced transfer printing technology utilizing germanium (Ge) as a nucleation layer of the metallic thin film. The effect of Ge on the silver (Ag) surface morphology is examined using SEM. The transfer printing is performed using various materials, i.e., silver (Ag) and gold (Au), and pre-fabricated SiO_2 nano-gratings over a centimeter-scale to investigate its versatility, scalability, and capability of transferrable

feature resolution, respectively. To demonstrate the capability of transferring arbitrary shapes, the dielectric bowtie structures are fabricated on the donor substrate, then transferred to the acceptor substrate, followed by Ag and Ge metal deposition. The resolution and surface morphology of transferred structures are precisely examined by various methodologies, e.g., SEM and AFM, respectively, and the optical characteristics are measured by UV-Vis spectrometer. The FDTD simulation is conducted according to the structural dimensions to verify their optical performance.

Chapter 4 introduces a new fabrication method for scalable manufacturing of the double-layered chiral metasurface for polarimetric imaging applications using the nanoimprint lithography (NIL) process. The development processes of NIL for each metasurface, i.e. a-Si metasurface and vertically coupled aluminum (Al) double-layered gratings (VCADGs) are summarized and demonstrated via the actual device fabrication. The scalability and uniformity are examined using the SEM images taken from various points of the mm-scaled fabricated samples. The integration of two metasurfaces is demonstrated using the developed multi-functional-direct NIL and the advanced alignment method, and the integrated device is investigated by optical microscopy and SEM to characterize the alignment accuracy and surface morphology. The spectra measurements are performed to examine its optical performance.

Chapter 5 summarizes the developed patterning technologies and highlights the main achievements of this dissertation. It concludes the dissertation with potential opportunities for future studies.

CHAPTER 2

STRUCTURAL COLOR PRINTING VIA POLYMER-ASSISTED PHOTOCHEMICAL DEPOSITION

2.1 Abstract

Structural color printings have attracted tremendous attentions due to their advantages of long-term sustainability, eco-friendly manufacturing, and ultra-high resolution. However, most of them require costly and time-consuming fabrication processes from nanolithography to vacuum deposition and etching. Here, we demonstrate a new color printing technology based on polymer-assisted photochemical metal deposition (PPD), a room-temperature, ambient, and additive manufacturing process without requiring any heating, vacuum deposition or etching steps. The PPD-printed silver films comprise densely aggregated silver nanoparticles filled with a small amount (estimated <20 % volume) of polymers, producing a smooth surface (roughness 2.5 nm) even better than vacuum-deposited silver films (roughness 2.8 nm) at ~ 4 nm thickness. Further, the printed composite films have a much larger effective refractive index n (~1.90) and a smaller extinction coefficient k (~0.92) than PVD ones in the visible wavelength range (400 nm to 800 nm), therefore modulating the surface reflection and the phase accumulation. The capability of PPD in printing both ultra-thin (~5 nm) composite films and highly reflective thicker metallic film greatly benefit design and construction of multi-layered Fabry-Perot (FP) cavity structures to exhibit vivid and saturated colors. Indeed, we demonstrated programmed printing of complex pictures of different color schemes and at a high spatial

resolution of ~6.5 μm by three-dimensionally modulating the top composite film geometries and dielectric spacer thicknesses (75 nm to 200 nm). Finally, PPD-based color picture printing is demonstrated on a wide range of substrates, including glass, PDMS, and plastic, proving its broad potential in future applications from security labelling to color displays.

2.2 Introduction

Colorful pigments from pictures serve to selectively absorb light within a spectral range, thus modulating the light reflection and color display. Conventional pigments, however, are usually toxic and relatively large. They also tend to degrade over time and lose their brightness and resolution. As an alternative, structural color makes use of micro- or nano-structured materials, such as plasmonic nanoantennas (i.e. disks, holes and rods) [1-3], metasurfaces [4-6], photonic crystals [7,8], and thin-film interferometer [9-11], to modulate the light absorption, scattering, and interference and accordingly display color. For example, plasmonic nanoantennas make use of localized surface plasmon resonance (LSPR) to engineer light absorption and scattering at sub-wavelength scale, capable of achieving ultra-high printing resolution. Dielectric (e.g. silicon [12,13], titanium oxide [14], etc.) nanoantennas exploit geometry-dependent electric dipole and magnetic dipole resonances that generates strong Mie resonance in the visible wavelength range, while exhibiting much lower optical losses compared to plasmonic nanostructures. Fabry-Perot (FP) cavity [15], typically employing a sandwich thin-film structure compromising a dielectric spacer between two reflectors, produces interferences between the top and

bottom reflectors, leading to a strong resonance in reflection magnified as a color change [16-21]. These metallic and dielectric structures are more durable than organic pigments [22,23], and can be scalably produced using eco-friendly manufacturing technologies [24,25]. As a result, structural color has emerged as a promising alternative for various color-display applications including filters [26-28], holograms [29,30], colorimetric sensors [31,32], anti-counterfeiting [33,34], and decoration [35,36].

To engineer optical resonance at particular wavelengths, structural color technologies based on plasmonic and dielectric nanoantennas require precise definition of structural dimensions at nanometer scale. The nanofabrication processes, such as electron beam lithography (EBL), focused ion beam (FIB), physical vapor deposition (PVD) and reactive ion etching (RIE), however, can seriously increase the cost and limit the applications. In comparison, conventional FP cavity structures use much simpler fabrication processes, mainly involving vacuum deposition of metal-dielectric-metal film stacks. Additionally, the optical resonance and color display can be conveniently tuned by modifying the thickness and/or refractive indexes of dielectric and metallic layers. However, there are still several remaining challenges for low-cost, high-resolution, and at-demand color printing of the FP cavity structures. First, conventional metal-based high-quality FP cavity presents a very sharp absorption with a broadband non-resonant reflection as background, which leads to low brightness and poor color purity in reflection [37-39]. The color saturation performance could be greatly improved by intentionally lowering the qualify (Q) factor of the cavity resonance, e.g. by using an absorbing material such as germanium and nickel (Ni) as the top reflector [40,41]. Further, the fabrication of such thin-film stack

comprising different materials requires multiple vacuum-based deposition processes in specialized facilities. This typically results in long processing time and increased cost. Additionally, metal deposition process generally is associated with high temperature but not always compatible with organic and soft materials, thus constraining the color printing applications on flexible substrates. Lastly, high-resolution printing requires micro-lithography in a well-controlled cleanroom environment, which is not readily accessible and potentially costly.

In this work, we will demonstrate the use of accessible, inexpensive, additive manufacturing (AM) technology to create colored pictures without photolithography, vacuum deposition, or etching processes. Here, we utilize our recently developed polymer-assisted photochemical deposition (PPD) process [42] to print the metallic reflectors in a FP cavity. The PPD technology is a room-temperature, non-toxic, solution-based additive manufacturing process, and used to print ultrathin (~5 nm) and smooth silver (Ag) films as the top absorptive reflector and also thick and reflective films as the back reflector. As a result, the printed metal-dielectric-metal FP structures exhibited vivid and saturated colors from blue to green and red on a variety of substrates, including glass, PDMS, and plastics. Importantly, PPD is capable of directly structure writing with a spatial resolution down to 6.5 μm, which is comparable with current colorant based color printing. This new printing technology is expected to have broad use in anti-counterfeit labels, colorimetric sensors, flexible structural color membranes, and decorations. The resolution can be further improved by improving the numerical aperture of the projection system to reduce the beam spot size on sample surface in future development.

2.3 Results

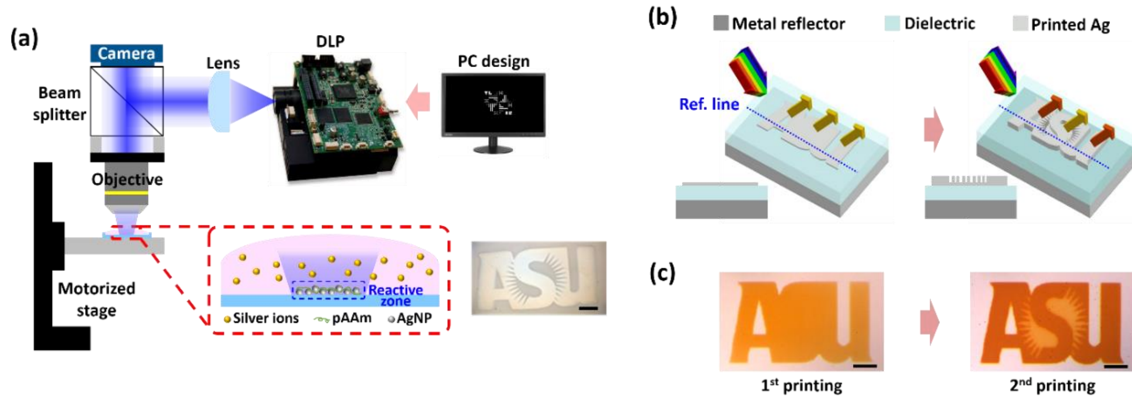

Figure 2.1: Structural color printing technology. (a) Schematic illustration of the polymer-assisted photochemical deposition (PPD) printing setup and an example of printed ASU logo (scale bar: 500 μm). (b) Three-dimensional scheme showing printing of multi-layered film stack into microstructures. (c) Optical images showing an example of printed colored ASU logo corresponding to (b). Scale bar: 100 μm.

The metal thin-film deposition was performed at room-temperature using our PPD system (Figure 2.1(a)). UV dynamic light projector (DLP) is used as the light source to photochemically induce metal reduction from a precursor solution. Our PPD system has been demonstrated capable of printing different metals, including gold, silver, and platinum [42]. Silver was chosen in this work owing to its high reflectance (>95 %) in the visible wavelength range [43]. Here, the precursor contains a metal salt (silver nitrate), reductant (sodium citrate dihydrate) and polymer reactant (pAAm). UV illumination (385 nm) triggers reduction of silver (Ag) ions to silver nanoparticles (AgNPs), which are then connected into continuous films assisted by the pAAm polymer. Uniquely, this AM system is therefore capable of adjusting both the lateral dimensions of printed metallic structure at micrometer scale, by selectively turning on and off the digital micro-mirror (DMD) pixels,

and also the film thickness at nanometer level, through controlling the film growth rate and time. For example, the spatial light intensity distribution is controlled by a DMD device within the DLP, and flexibly programmed by computer-generated layout. The light pattern guides the Ag film growth at targeted areas and in designed shapes, exemplified by an Arizona State University (ASU) logo (Figure 2.1(a) insert). The capability of metal printing with precise control in both lateral and vertical dimensions is particularly useful for the creation of an asymmetric FP cavity to simultaneously display multiple structural colors (Figure 2.1(b)). The FP cavity structure consists of an Ag reflector at the bottom, a dielectric spacer in the middle and printed Ag thin film on the top. In one example, three different colors can be printed simultaneously, that is a background layer without the top Ag films, a middle ground layer with a very thin (e.g. <10 nm) Ag film, and a foreground layer with slightly thicker (e.g. >10 nm) Ag film. This multi-thickness film stack can be produced in a single print without moving the substrate or refilling the precursor, but rather simply by overlaying two computer-generated image patterns in consecutive illumination steps. For instance, maroon-colored letters of ASU as the foreground can be revealed on and distinguished from the gold-colored middle ground layer (Figure 2.1(c)), creating a high contrast with micrometer scale structural resolution.

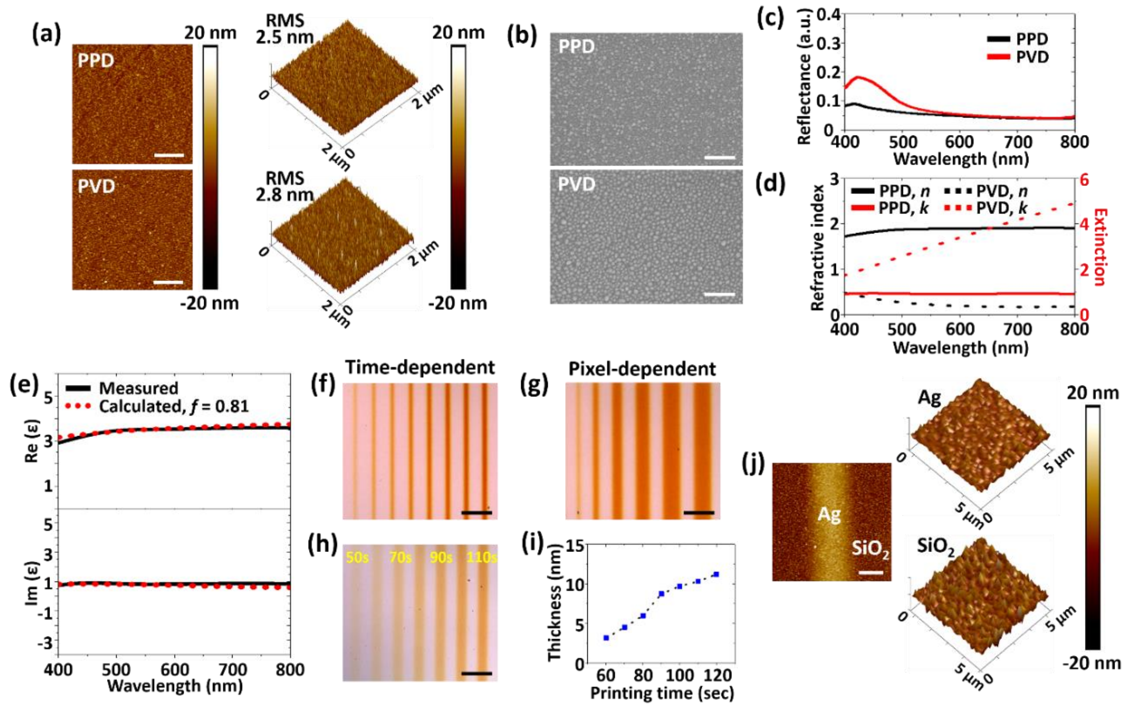

Figure 2.2: Structural and optical characterization of PPD-printed ultra-thin films. (a-c): Surface morphology and optical response of 4 nm-thick Ag films prepared on fused silica substrate by PPD and PVD: (a) 2D (left, scale bar: 500 nm) and 3D (right) profile of AFM images, (b) SEM images (scale bar: 200 nm), and (c) measured relative reflectance. (d) Measured optical properties (*n*, in black; *k*, in red) of 15 nm Ag films prepared on fused silica substrate by PPD (solid lines) and PVD (dot lines), respectively. (e) Measured (black solid line) and calculated (red dotted line) permittivities of PPD film. Top: real part. Bottom: Imaginary part. (f-h) Optical images of PPD-printed lines on SiO_2 (200 nm)/PVD-Ag (85 nm) substrate: (f) single-pixel lines printed from 150 sec (left) to 360 sec (right), (g) single-pixel (left) to 6-pixel (right most) lines printed at 150 sec, and (h) four-pixel lines printed from 50 sec to 110 sec. Scale bar: 50 μm. (i) Printed PPD film thickness as a function of printing time extracted from (h). (j) Surface morphology of PPD film on SiO_2 (200 nm)/PVD-Ag (85 nm) substrate. Left: 2D profile of AFM image of 70 s printed four pixel line from (h) (scale bar: 5 μm). Right: 3D profile of AFM images of the printed PPD Ag and sputtered SiO_2.

To design the FP cavities for desired color printing, we first experimentally investigated the film morphology and optical response of PPD-printed ultra-thin Ag films, and compared these to thermally evaporated PVD films (Figure 2.2). First, atomic force microscopy (AFM) (Figure 2.2(a)) and scanning electron microscopy (SEM) (Figure. 2.2(b)) imaging were used to study the morphology and surface roughness of PPD- and PVD-deposited thin films (both ~4 nm thick on fused silica substrate, and deposited at similar rate of 2.4 nm min^{-1}). The PPD film was found comparable to but slightly smoother (root-mean-square (RMS) surface roughness 2.5 nm) than PVD film (RMS roughness 2.8 nm). This is attributed to the fact that noble metals such as gold and silver tend to migrate on the surface and nucleate into MNPs, resulting in relatively rough and sometimes discontinuous films when deposited at sub 20 nm by PVD [44,45]. In comparison, reduced MNPs in PPD are stabilized by chemical capping agents and pAAm polymers [46], which produce continuous thin film even at sub 10 nm thickness. These phenomena were evidently observed by SEM imaging (Figure 2.2(b)). Further, the reflectance spectra of both thin films were examined by UV-visible spectrometer (Figure 2.2(c)). Despite similar reflectance in the longer wavelength range (600 – 800 nm), PVD film displayed a higher reflectance with a peak at 430 nm compared to PPD film, which was due to LSPR scattering of silver nanoparticles (AgNPs) [47]. These results again confirmed the formation of AgNPs islands rather than continuous structures via PVD deposition. Indeed, the capability of PPD to print ultrathin yet continuous films is much desired in this FP cavity based color printing demonstration.

To compare the optical refractive indexes (n, k) of PPD- and PVD-films, 15 nm thick Ag was prepared on fused silica substrates, and examined by UV-near infrared (NIR) spectroscopic ellipsometry (Figure 2.2(d)). Notably, PPD film had a higher refractive index (n ~1.90) and lower extinction coefficient (k ~0.92) than PVD one in the visible wavelength range (400 nm – 800 nm). Clearly, the optical permittivity of aggregated nanoparticles behaved significantly different from ideal metallic films or isolated nanoparticles [48]. This is thought to be due to the presence of polymer (e.g. pAAm has n ~1.38, k ~0) residue within the printed PPD thin films, effectively forming MNPs/polymer nanocomposite with its optical properties strongly affected by the MNP and polymer material compositions [49,50]. To further investigate the printed PPD film, we employed effective medium theory (EMT) to set up a numerical model that can precisely predict the optical properties of the nanocomposite (details in Appendix C) [51]. Importantly, the unique optical response of PPD-printed composite film can be successfully interpreted by EMT, evidenced by the fact that EMT-calculated effective permittivity agrees very well with the empirical values with a filling factor of AgNPs fit as 0.81, i.e. 81 % of the total volume of nanocomposites (Figure 2.2(e)). This indicated very high concentration of AgNPs in the nanocomposite matrices.

Then, we studied the impact of printing conditions, particularly printing time and pixel sizes, on the structural lateral resolution and film thickness (Figure 2.2(f)-(i)). The dielectric-coated metallic substrates, i.e. 200 nm SiO_2 dielectric layer on 85 nm PVD Ag back reflector, were used in this study. First, the impact of printing time (150 s to 360 s) on linewidth was studied using single-pixel straight lines (Figure 2.2(f)). Noticeably, the printing rate on dielectric-coated metal substrate (6.5 nm min^{-1}) was ~2.7 times higher than

bare fused silica substrate (2.4 nm min^{-1}) (Figure. A.1 (c) and (d)). This is attributed to a ~2.5 times higher electromagnetic field intensity at the printing surface resulting from the reflection of illuminating UV light at the PVD Ag reflector, estimated from FDTD simulation (Figure A.1(e)). Additionally, the printed lines were found to expand with increased printing time, e.g. 4.6 µm at 150 s (film thickness of 8.6 nm) compared to 8.2 µm at 360 s (thickness 22.5 nm). The observed linewidth broadening is thought attributed to the metal structure nucleation and growth process. It is understood that the reduced MNPs in the solution can go through a diffusion process as printing proceeds, which resulted in wider linewidth. On the other hand, it is also possible the initially printed metal lines would serve as nucleation seeds to guide subsequent metal growth at all directions, including from the line edges, which further enhanced the linewidth increase. Besides the dependence on printing time, the linewidth was also found dependent on pixel sizes (Figure 2.2(g)). Interestingly, single-pixel and two-pixel lines were significantly narrower (4.6 µm and 7.8 µm, respectively) than larger-pixel (3 to 6) ones (14 µm to 24.3 µm), despite the same printing time (150 s). This trend is consistent with our observation of Ag printing on bare fused silica (Figure A.2). In both cases, the metal film thickness (Figure A.2) and film-stack color contrast (Figure 2.2(g)) of printed lines gradually increased with pixel size, and reached a plateau with four or more pixels. The correlation between pixel size and film thickness is a unique characteristic of our PPD process. It is attributed to the fact that the metal film growth rate is strongly dependent on the effective electromagnetic field intensity at the nucleation side, which is not only controlled by illumination but also affected by the reflection from just printed metallic thin-film structures. The optical scattering from the rougher edges is expected significantly higher at narrow lines, thus rendering less strong

effective electromagnetic field intensity and slower film growth compared to wider lines. Such scattering effect, however, could become less dominant when the linewidth is significantly larger than the illumination wavelength, i.e. 20.3 µm at 4 pixels compared to 385 nm illumination. Such feature size dependent printing phenomena bring extra flexibility for PPD to produce multi-colored structures within a single printing process, for example by design structures of different widths and altering the printing time.

Further, these studies allow calibration of film thickness at different pixel sizes and different printing time for accurate structural design in color printing. For example, four-pixel lines were printed from 50 s to 110 s with 10 s step size on the prepared dielectric (sputtered SiO_2) on silver substrate (Figure 2.2(h)). The PPD-printed nanocomposite film thicknesses were examined by AFM, and displayed almost linear dependence on the printing time (Figure 2.2(i)). Interestingly, the 3D profile of AFM images also indicated a much smoother surface (RMS = 1.7 nm) for the ultra-thin nanocomposite film (6 nm from 70 s printing) than the SiO_2/silver substrate itself (RMS = 3.2 nm) (Figure 2.2(j)). This can be understood from the unique PPD printing mechanism that photochemically reduced, pAAm-capped, small AgNPs (estimated 5-10 nm from AFM and SEM) could easily attach to the substrate surface via Van der Waals interactions [42], thus filling the voids with pAAm and AgNPs and favorably reducing substrate surface roughness [52].

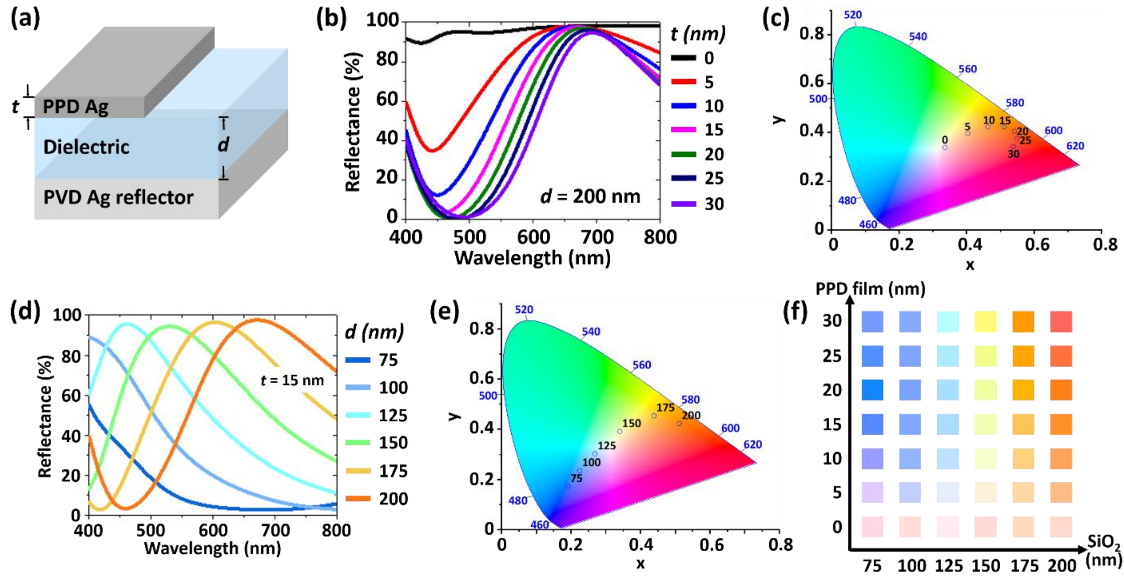

Figure 2.3: FDTD simulated reflectance spectra for design of structural colors. (a) Three-dimensional schematic of the FP cavity, with the top-layer PPD-printed thin film thickness *t* and dielectric spacer thickness *d* as variables. (b) Reflectance spectra with variable *t* and fixed *d* = 200 nm). (c) 1931 CIE color coordinates corresponding to (b). (d) Reflectance spectra for variable *d* and fixed *t* = 15 nm. (e) CIE color coordinates corresponding to figure d. (f) The color palettes based on the simulated reflectance spectra with varying *d* and *t*.

To guide our color printing design, FDTD simulations were conducted with empirically measured optical indexes of nanocomposite and dielectric (SiO_2) films to understand their thickness impact on the color display. We started with investigation into the impact of material effect of top metal film materials, i.e. PPD-printed or PVD-deposited, using the same cavity structure, consisting of 85 nm PVD Ag back reflector at the bottom, 200 nm SiO_2 dielectric layer in the middle and a variable metal film thickness *t* (0 to 30 nm, 5 nm step size) on the top (Figure 2.3(a)), was used in this study. Here the change in the thickness of the PPD-printed nanocomposite film directly affects both the reflection (and according

the transmission into the FP cavity) and also the phase accumulation (Figure A.3). Therefore, the film thickness can strongly modulate the interference effects in the FP cavity, shifting both the amplitude and resonance of reflected light (Figure 2.3(b)). Using 15 nm PPD film as a top layer, significantly broaden reflectance spectra (~300 nm at full width half maximum (FWHM)) and relatively high reflectance (98 % at 670 nm) were calculated in the visible wavelength range (Figure 2.3(b) – solid pink line), which facilitated highly-contrast and bright color printing in selected wavelength ranges [17]. As aforementioned, PPD film effectively acted as an absorptive composite material composed of highly concentrated absorbing AgNPs [53] and non-absorbing pAAm polymer [54]. This behavior differs significantly from using PVD Ag films as the top layer of the FP cavity (Figure A.4), which was calculated to display a high reflectance with a much narrower resonance in the visible wavelength range and much less effective to produce saturated colors. In comparison, the predicted equivalent colors from our simulated reflectance spectra were illustrated on the 1931 International Commission on Illumination (CIE) chromaticity diagram by using colorimetric transformations (Figure 2.3(c) for PPD top film and Figure A.4(c) for PVD film), clearly showing a much broader range of color tuning by PPD printing compared to PVD film that barely displayed color differences by changing the film thickness.

Similarly, we conducted FDTD simulation with various dielectric layer thicknesses (*d*) to obtain wider color gamut (Figure 2.3(d)-(e)). The cavity structure was composed of 85 nm PVD Ag back reflector, 75 to 200 nm SiO_2 dielectric spacer (*d*, 25 nm step size) in the middle, and 15 nm PPD film on the top. As the SiO_2 thickness *d* increases, the resonance

peak wavelength redshifted from 330 nm to 400 nm, 460 nm, 530 nm, 600 nm and 670 nm, respectively (Figure 2.3(d)). Compared to the color tuning effect of PPD-printed metal film thickness (Figure 2.3(b)), the dielectric layer spacer has a more pronounced impact in modulating the reflectance amplitude and resonance peak wavelengths. The predicted colors corresponding to the reflectance spectra on the CIE chromaticity diagram (Figure 2.3(e)) further clearly indicated broader color gamut than that with varying PPD film thickness *t* (Figure 2.3(c)). This can be understood as the result of significant change in optical path and accumulated phase in the cavity [16-18]. To visualize the printed colors, a two-dimensional color palette was created with varying SiO_2 dielectric layer and the top PPD film thicknesses (Figure 2.3(f)). For example, the palette showed highly saturated vivid colors of blue, light blue, cyan, light green, orange and blood orange, respectively, as *d* increases while keeping $t = 20$ nm. Noticeably, distinguishable colors were also obtained by simply modifying *t* with the same dielectric layer, which provides more degrees of freedom for tunable color printing.

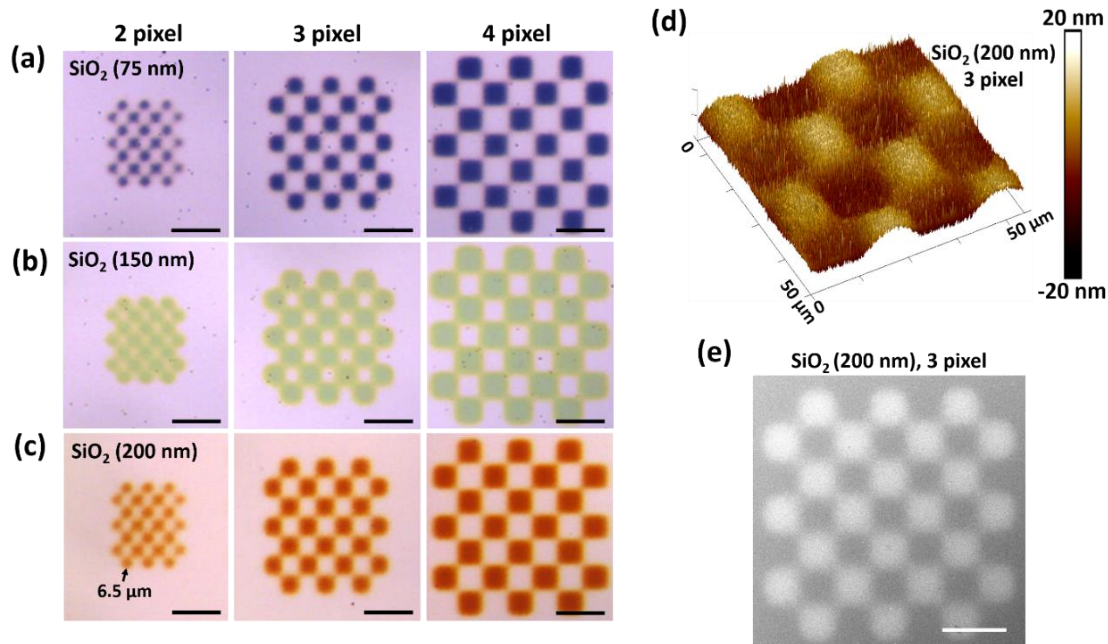

Figure 2.4: Experimental demonstrations of color printing with micro-meter resolution. (a – c) Optical images of various pixel-sized checkerboard printed on the SiO_2/PVD Ag substrate with the SiO_2 thickness as 75 nm, 150 nm, 200 nm, respectively. Scale bar: 30 µm. (d) AFM image and (e) SEM image (scale bar: 30 µm) of the printed 3 pixel-checkerboard on 200 nm SiO_2 layer. The PPD film was ~20 nm thick.

Based on the above simulation results, we employed various thicknesses of SiO_2 dielectric layer (d = 75 nm, 150 nm and 200 nm, respectively) on the 85 nm PVD Ag back reflector to experimentally demonstrate the color generation (Figure 2.4). The printing was carried out for 180 s (thickness ~20 nm) with checkerboard patterns to characterize the spatial resolution of our PPD system for color printing. The experimentally produced colors were consistent with the simulation-predicted color palette with a spatial resolution down to 6.5 µm (Figure 2.4(a)–(c)). The 3D profile of AFM image again confirmed a much smoother surface (RMS roughness 1.5 nm) of PPD film than sputtered SiO_2 dielectric layer

(RMS roughness 3.2 nm) with sufficiently distinguishable micro scale features (Figure 2.4(d)). Interestingly, distinct structures were well preserved even at the corners and boundaries of neighboring areas (Figure 2.4(a)–(c)), indicating the printing faithfully produced microstructured patterns as confirmed by SEM image (Figure 2.4(e)). This demonstration implies that our PPD based AM technology distinguishes itself from conventional structural color printing methods in its capability of creating micro-scaled colored features without any photolithography processes.

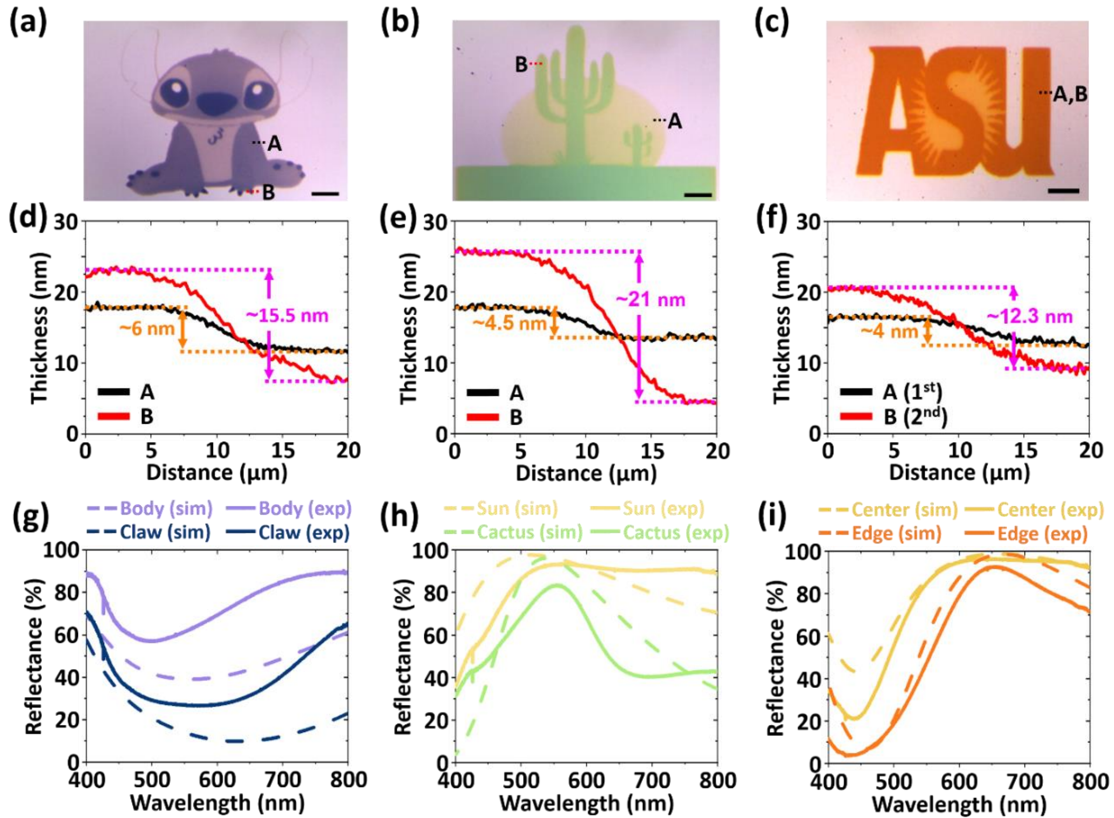

Figure 2.5: Demonstration of the feasibility of printing complex structures with various colors. (a) A cartoon character 'Stitch' (d = 75 nm), (b) a symbol of Arizona 'Cactus' (d = 150 nm), and (c) a logo of 'ASU' (d = 200 nm). Scale bar: 100 μm. (d – f) AFM measured PPD film thicknesses t for each structures corresponding to (a – c), respectively. (g – i) FDTD simulated reflectance spectra (dashed lines) and experimentally measured reflectance spectra (solid lines) for each structures corresponding to (a – c), respectively.

To investigate the feasibility of color printing of complex structures, three different images were used on dielectric-coated silver substrates (Figure 2.5). Given the layer-by-layer nature of the PPD process, those images were divided into several layers for printing. A colored microscale cartoon image of 'Stitch' was printed on 75 nm SiO_2 dielectric layer to represent blue-color over an area of 670 μm × 610 μm (Figure 2.5(a)). A multi-step

printing, i.e. 100 s for belly and ears, 150 s for head, arms and legs, and 210 s for eyes, nose and claws, was found to achieve the best color contrast. Besides, a ‘Cactus’, the symbol of Arizona state, was printed over an 860 µm × 620 µm area on 150 nm SiO_2 dielectric layer as the representative for green-color (Figure 2.5(b)). To obtain the best printing quality, the printing time was set as 45 s for sun and 210 s for cactus, respectively. Additionally, a colored microscale logo of ‘ASU’ was printed over an area of 720 µm × 450 µm on 200 nm SiO_2 dielectric layer to demonstrate red and orange color printing (Figure 2.5(c)). The printing time was 60 s for ASU logo background and 180 s for ASU letters, respectively. Our AFM analysis (Figure 2.5(d)–(f)) further confirmed the highly saturated and high-contrast colors were created from as thin as 4 nm PPD films. Lastly, FDTD simulations were conducted with the empirically measured film thicknesses and refractive indexes to calculate the reflectance spectra, and compared to the spectra measured by UV-Vis spectrometer (Figure 2.5(g)–(i)). Noticeably, the measured reflectance spectra (solid lines) showed large modulation in the reflectance similar to simulated spectra (dashed lines), despite small discrepancies possibly attributed to differences in film geometries and material properties between simulations and experiments. We also investigated the effect of polymer encapsulation layer on color retention time using the same structures (details in Appendix B). Although the reflectance spectra was slightly red-shifted after 14 days of printing (Figure B.1(d)) possibly due to additional reaction between AgNPs and PMMA, the encapsulation layer significantly improved the color retention time of printed image (Figure B.1(b)). Nevertheless, these results convincingly demonstrate that the PPD based structural color printing is an alternative and cost-effective solution for high-quality and micro-scaled color printing

applications. In future studies, it is possible to print multiple colors by engineering the FP-cavity dielectric layers at different thicknesses on one sample. AM technology also allows photo-initiated polymerization that can be used to print dielectric spacers at designed thicknesses [55].

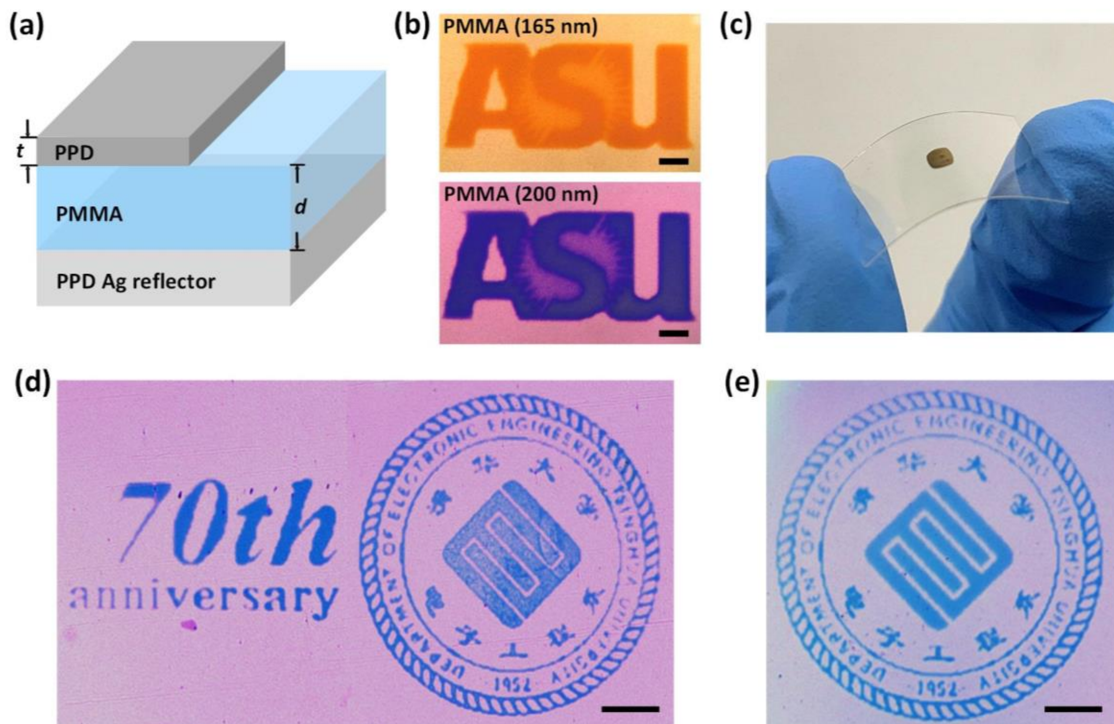

Figure 2.6: Photolithography and vacuum-free structural color printing. (a) Three-dimensional schematic of the FP cavity. (b) An exhibited colored ASU logo on the dielectric-coated metallic layer with various PMMA thicknesses using fused silica as a substrate. Scale bar: 50 µm. (c) Camera image of fabricated FP cavity on PET substrate with slight bending capability. (d and e) Optical images of produced colored DEETHU logo on the dielectric-coated metallic layer using PET and PDMS as substrates, respectively. Scale bar: 100 µm.

The above color printing demonstrations were achieved without photolithography, yet they still required several vacuum deposition processes for substrate preparation. To eliminate any vacuum depositions altogether, we further utilized PPD films to print both the bottom metal reflector and top-layer thin film, and used spin-coated PMMA as a dielectric layer (Figure 2.6(a)). The reflectance from a back reflector strongly influences the FP cavity optical performance and directly affects the color saturation [56]. Here we examined the PPD-printed back reflector on the fused silica substrates after 8 min, 9 min and 10 min printing by UV-Vis spectrometer, using a protected silver mirror as a reference (Figure A.5(a)). Interestingly, 8 min printed PPD film showed the highest relative reflectance (79 % at 600 nm) compared to longer time (9 min and 10 min, with 77 % and 74 %, respectively) printed films, possibly attributed to increased surface roughness (Figure A.5(b)) due to undesired particle growth and resultant undesired scattering loss [50]. Therefore, 8 min printed PPD back reflector was chosen for our printing on different substrate materials. The PPD back reflector was characterized by surface profiler, UV-Vis spectrometer, AFM and SEM. Remarkably, the film surface was smoother (RMS roughness 3.5 nm) than the PVD back reflector (RMS roughness 5.5 nm) at the same thickness (85 nm) (Figure A.6(a)–(c)), despite lower reflectance (Figure A.6(d)). Then PMMA was spin-coated on the back reflector, with its thickness adjusted by changing spin coating speed. The PMMA refractive index was characterized by ellipsometry and found similar to that of SiO_2 in the visible wavelength range (Figure A.7). The PMMA was solidified overnight and briefly treated by oxygen plasma prior to the top-layer metal printing. A microscale logo of ‘ASU’ with a size of 410 μm × 160 μm was printed on 165 nm- and 200 nm-thick PMMA layers (Figure 2.6(b)), producing different colors with a

spatial resolution of ~7 μm. Both the color saturation and printing resolution were comparable to using PVD-deposited back reflectors. A lower contrast was observed, possibly because of the lower reflectance of back reflector, which could negatively affect the optical reflectance from the FP cavity.

Printing on flexible substrate is desired in many color printing applications, yet it could be problematic when using conventional fabrication processes (e.g. PVD and photolithography) due to the instability of the substrates when exposed to vacuum, heat or organic solvent environments [57,58]. An unique advantage of PPD printing is its room-temperature, ambient, and solvent-free printing process that allows it to be compatible to various substrates, as demonstrated in our previous work [40]. Here we further demonstrate micro-scaled structural color printing onto flexible PET and PDMS, the most well-known flexible substrates. We printed the logo of the department of electronic engineering of Tsinghua University (DEETHU) in order to celebrate their 70th anniversary, which is the theme of this special issue. Clearly, the FP cavity was well fabricated on PET and intact with slight bending test (Figure 2.6(c)). The optical images of the colored DEETHU logo on PET and PDMS substrates (Figure 2.6(d) and (e)), respectively, strongly demonstrated the feasibility of color printing with a spatial resolution about 6.3 μm, completely comparable to our printing on rigid silica substrates.

2.4 Discussion

In summary, we have developed a new approach to print micro-scaled structural colors using room-temperature, ambient, and low-cost PPD process. The ultra-thin PPD-printed film showed satisfactory surface morphology characteristics in surface roughness and continuity, and acted as an absorptive layer in a FP cavity structure. The FP cavity designs were optimized by coupling experimental studies and FDTD simulations to modulate the reflectance in the visible wavelength range and to produce highly saturated and bright colors. We have further demonstrated printing of complex structures in logos and pictures of different colors with a spatial resolution down to 6.5 µm, on both rigid fused silica and flexible substrates Our demonstrations show that the PPD color printing technology can eliminate complex photolithography and vacuum deposition processes, thus opening new windows to a wide variety of applications including colorimetric sensors, surface decoration, wearable optical devices, and flexible display with high resolution and low cost.

2.5 Materials and methods

2.5.1 Materials

Silver nitrate (ACS reagent, ≥99.0 %), sodium citrate dihydrate (≥99.0 %), allylamine (AAm, ≥99.0 %), 2-hydroxy-4'-(2-hydroxyethoxy)-2-methylpropiophenone (Irgacure 2959, 98 %) and trichloro(1*H*,1*H*,2*H*,2*H*-perfluorooctyl)silane were purchased from Sigma-Aldrich. PMMA (950K A4) was purchased from MicroChem. Dow Corning Sylgard 184 silicone elastomer was purchased from VWR. Polyethylene terephthalate (PET) film (PF-40/1.5-X4) was acquired from Gel-Pak. DLP® LightCrafter™ E4500 MKII™ UV (385 nm, 2 W) was purchased from EKB Technologies Ltd. Motorized stage (100 mm motorized linear translation stage, stepper motor, 1/4"-20 taps) and CMOS camera (1280×1024 pixels) were purchased from Thorlabs. All chemicals used as received without further purification.

2.5.2 Preparation of Ag Printing Precursor

The Ag printing precursor was prepared by mixing silver nitrate, sodium citrate dihydrate and poly(allylamine) (pAAm). Silver nitrate and sodium citrate dihydrate solid powders were dissolved in DI water respectively, to obtain 100 mM stock solution for each chemical. pAAm stock solution was prepared by photo-polymerization of AAm. 200 μL AAm stock solution which contained 1 M AAm and 0.57 mg mL^{-1} of Irgacure 2959 was illuminated under UV light (BlueWave® 200 UV curing spot lamp, 365 nm, 3.0 W cm^{-2})

for 15 min. The polymerized solution was used as it is. To produce Ag printing precursor, 80 µL silver nitrate stock solution, 60 µL sodium citrate dihydrate stock solution and 16 µL pAAm stock solution were added into 844 µL DI water. The prepared precursor should be consumed immediately.

2.5.3 Preparation of Substrates

Bare Si wafer was used as a substrate to prepare ultra-smooth polydimethysilane (PDMS) sheets. Self-assembled monolayers (SAMs) were formed on the substrate surface by using trichloro(1*H*,1*H*,2*H*,2*H*-perfluorooctyl)silane at 100 ℃ for 30 min as anti-sticking layer followed by solvent and RCA-1 cleaning. After cooling the Si substrate, a mixture of Sylgard 184 silicone elastomer and its curing agent (10:1 wt/wt) was poured onto it, degassed and further cured at 70 ℃ for 3 h. The prepared PDMS was gently peeled off from the substrate, cut into rectangles and transferred onto solvent cleaned coverslip for easy handling during the printing process. The PET substrate was delaminated from commercially available Gel-film and used as it is. Fused silica substrate was solvent and RCA-1 cleaned to remove absorbed organic and inorganic contaminants. All the substrates were nitrogen blown and cleaned with oxygen plasma cleaning system (Tergeo plasma cleaner, 75 W, 5 sccm) for 30 s prior to further fabrication process.

2.5.4 Ag and SiO_2 Film Deposition

Sub-5 nm Ag film was deposited onto fused silica substrate by thermal evaporator (Denton Benchtop turbo) to compare the quality of ultra-thin printed PPD Ag film with conventionally evaporated PVD one. Ultra-pure silver pellet (99.999 % purity, Materion) was used with deposition rate of 0.4 Å s^{-1} which is identical to the printed Ag deposition rate with the same thickness. This deposition was carried out without adhesion layer for a precise comparison to printed Ag film. Metal/dielectric substrate was prepared using conventional deposition process to demonstrate the feasibility of structural color printing using PPD. 3 nm chromium was evaporated as an adhesion layer, then 85 nm Ag film was deposited as back reflector onto fused silica substrate at 1.7 Å s^{-1} with the same evaporator. The deposition rate was identical to printed Ag film with the same thickness. SiO_2 dielectric layer was deposited at 0.5 Å s^{-1} using the radio frequency (RF) sputtering system (Kurt J. Lesker) with various thicknesses to adjust resonance peak of the cavity.

2.5.5 FP cavity based structural color printing using PPD

The aforementioned metal/dielectric substrate was used for demonstration of structural color printing. Desired printing patterns were designed in software Paint due to its pixel-based interface. A reservoir was made by PDMS in the same manner as described in *preparation of substrates* section was placed onto the substrate, then filled with the printing precursor. Designed patterns were illuminated by digital mirrors in DLP® LightCrafter™ E4500 MKII™ system (385 nm, output power of 2 W) from the top through the precursor using a 10x objective lens with numerical aperture (NA) of 0.3 to print Ag on the substrate

surface (Figure 2.1(a)). The sample height was precisely controlled by motorized stage to achieve the best printing quality. The illuminated patterns were dynamically changed by PC software after the certain amount of time for the first layer printing. After the completion of printing, the reservoir was removed from the substrate, and the substrate was rinsed with DI water and dried with nitrogen blow. To prove photolithography and vacuum deposition-free structural color printing on rigid and flexible substrates, fused silica, PDMS and PET substrates were used. To begin with, 85 nm thick PPD Ag film was printed as back reflector, then PMMA was spin coated onto printed film as dielectric layer. The substrates were left at room temperature for overnight to evaporate solvent and solidify PMMA. Oxygen plasma treatment (Tergeo plasma cleaner, 25 W, 10 sccm) was employed for 30 s to make PMMA surface be hydrophilic, that the printing surface became more attractive to the printing precursor. Finally, designed patterns were printed on the top of PMMA surface in the same manner to complete structural color printing.

2.5.6 Film Characterization

Atomic force microscopy (AFM, Bruker Multimode 8) was used to examine the thickness and surface roughness of both PPD and PVD films. A tapping mode was employed at ambient condition with various scan size and at a scan rate of 1 Hz. The detailed surface morphology was inspected by scanning electron microscopy (SEM, Hitachi S-4700 FESEM) with an acceleration voltage of 5 keV and current of 10 μA. A thin layer of Au/Pd was sputtered (Cressington sputter coater 108) on the samples to enhance imaging resolution prior to SEM measurements. Optical properties (refractive

index n, extinction coefficient k) of PPD and PVD films and dielectric layers were measured by UV-NIR spectroscopic ellipsometry (J.A. Woollam, M-2000). Olympus BX53 fluorescent microscope coupled Horiba iHR320 imaging spectrometer was utilized to record all the optical images and reflectance spectra of fabricated samples. A protected silver mirror (Thorlabs, PF10-03-P01) was used as reference to calculate relative reflectance of the samples, which has optical reflectance over 97.5 % in the visible wavelength range.

2.5.7 Simulation

The finite-difference time-domain (FDTD) simulations were carried out to calculate reflectance spectra in the visible wavelength range. Various thickness of printed PPD film and SiO_2 dielectric layer were employed to design the structural geometry of the FP cavity for structural color printing. Periodic boundary conditions ($\pm x$, $\pm y$ direction) and perfectly matched layers ($\pm z$ direction, parallel to the propagation of electromagnetic waves) were used within a unit cell of 200 nm along the $\pm x$ and $\pm y$ direction. The unit cell consisted of 85 nm thick PVD back reflector, d nm SiO_2 dielectric layer and t nm PPD or PVD Ag films. The plane wave in the visible wavelength range (400 – 800 nm) was used as the light source, which was incident perpendicular to the unit cell. The mesh sizes were set as 2 nm along the $\pm x$ and $\pm y$ direction and 1 nm along $\pm z$ direction. The measured optical properties (n, k) of each material were used for simulation. The reflectance was monitored in the x–y plane, ~1000 nm away from the top surface of structure. Using colorimetric transformations, the simulated reflectance spectra were mapped on the CIE 1931

chromaticity diagram to display the corresponding colors. They were compared with experimental observations.

2.5.8 Effective Medium Theory

Effective medium theory (EMT) was utilized to numerically calculate the effective permittivity (ε_{eff}) of the printed PPD film to characterize its optical properties. Bruggeman`s EMT model was employed for calculation due to the aggregated structure of AgNPs and pAAm in the nanocomposites. The formula for ε_{eff} read:

$$\varepsilon_{eff} = \varepsilon_p \left[1 + \frac{f(\varepsilon_{np} - \varepsilon_p)}{\varepsilon_p + n(1-f)(\varepsilon_{np} - \varepsilon_p)}\right],$$

where ε_{np} and ε_p were the permittivities of AgNPs and pAAm, respectively, and f was the filling factor of AgNPs in the nanocomposite. A shape factor n was introduced as a fitting parameter to generalize the equation. To investigate the average AgNP size, we performed pAAm concentration dependent PPD printing. From the SEM images with various pAAm concentration (Figure C.3), we observed particles from sub-5 nm to 10 nm with distinguishable contrast, particularly in 30 mM of pAAm concentration, which probably attributed to higher pAAm capping efficiency for AgNPs (Figure C.3(e)). Therefore, the average size of AgNPs was set as 10 nm in diameter for the purpose of calculating ε_{np} using our model.

2.6 References

[1] Wang, H. Wang, X., Yan, C., Zhao, H., Zhang, J., Santschi, C. & J. F. Martin, O. Full color generation using silver tandem nanodisks. ACS Nano, **11**(5), 4419-4427 (2017).

[2] Kumar, K., Duan, H., Hegde, R. S., Koh, S. C. W., Wei, J. N. & Yang, J. K. W. Printing colour at the optical diffraction limit. Nature Nanotechnology, **7**, 557-561 (2012).

[3] Hail, C. U., Schnoering, G., Damak, M., Poulikakos, D. & Eghlidi, H. A plasmonic painter's method of color mixing for a continuous red-green-blue palette. ACS Nano, **14**(2), 1783-1791 (2020).

[4] Liu, X., Huang, Z. & Zang, J. F. All-dielectric silicon nanoring metasurface for full-color printing. Nano Letters, **20**(12), 8739-8744 (2020).

[5] Kim, M., Kim, I., Jang, J., Lee, D., Nam, K. T. & Rho, J. Active color control in a metasurface by polarization rotation. Applied Sciences, **8**(6), 982 (2018).

[6] Huang, Y., Zhu, J., Jin, S., Wu, M., Chen, X. & Wu, W. Polarization-controlled bifunctional metasurface for structural color printing and beam deflection. Optics Letters, **45**(7), 1707-1710 (2020).

[7] Nam, H., Song, K., Ha, D. & Kim, T. Inkjet printing based mono-layered photonic crystal patterning for anti-counterfeiting structural colors. Scientific Reports, **6**, 30885 (2016).

[8] Chen, K., Fu, Q., Ye, S. & Ge, J. Multicolor printing using electric-field-responsive and photocurable photonic crystals. Advanced Functional Materials, **27**(43), 1702825 (2017).

[9] Yakovlev, A. V., Milichko, V. A., Vinogradov, V. V. & Vinogradov, A. V. Inkjet color printing by interference nanostructures. ACS Nano, **10**(3), 3078-3086 (2016).

[10] Rana, A. S., Zubair, M., Anwar, M. S., Saleem, M. & Mehmood, M. Q. Engineering the absorption spectra of thin film multilayer absorbers for enhanced color purity in CMY color filters. Optical Materials Express, **10**(2), 268-281 (2020).

[11] Yakovlev, A. V., Milichko, V. A., Pidko, E. A., Vinogradov, V. V. & Vinogradov, A. V. Inkjet printing of TiO_2/AlOOH heterostructures for the formation of interference color images with high optical visibility. Scientific Reports, **6**, 37090 (2016).

[12] Nagasaki, Y., Suzuki, M. & Takahara, J. All-dielectric dual-color pixel with subwavelength resolution. Nano Letters, **17**(12), 7500-7506 (2017).

[13] Yang, W., Xiao, S., Song, Q., Liu, Y., Wu, Y., Wang, S., Yu, J., Han, J. & Tsai, D.-P. All-dielectric metasurface for high-performance structural color. Nature Communications, **11**, 1864 (2020).

[14] Sun, S., Zhou, Z., Zhang, C., Gao, Y., Duan, Z., Xiao, S. & Song, Q. All-dielectric full-color printing with TiO_2 metasurfaces. ACS Nano, **11**(5), 4445-4452 (2017).

[15] Hodgson, N. & Weber, H. The Fabry Pérot resonator. in Laser Resonators and Beam Propagation 2nd edn, vol. 108 (eds Hodgson, N. & Weber, H) Ch. 4 (New York: Springer, 2005).

[16] Yang, Z., Zhou, Y., Chen, Y., Wang, Y., Dai, P., Zhang, Z. & Duan, H. Reflective color filters and monolithic color printing based on asymmetric Fabry-Perot cavities using nickel as a broadband absorber. Advanced Optical Materials, **4**(8), 1196-1202 (2016).

[17] Lee, J., Kim, J. & Lee, M. High-purity reflective color filters based on thin film cavities embedded with an ultrathin $Ge_2Sb_2Te_5$ absorption layer. Nanoscale Advances, **2**(10), 4930-4937 (2020).

[18] Yang, Z., Chen, Y., Zhou, Y., Wang, Y., Dai, P., Zhu, X. & Duan, H. Microscopic interference full-color printing using grayscale-patterned Fabry-Perot resonance cavities. Advanced Optical Materials, **5**(10), 1700029 (2017).

[19] Kim, S. J., Choi, H. K., Lee, H. & Hong, S. H. Solution-processable nanocrystal-based broadband Fabry-Perot absorber for reflective vivid color generation. ACS Applied Materials & Interfaces **11**(7), 7280-7287 (2019).

[20] Lee, I. H., Li, G., Lee, B. Y., Kim, S. U., Lee., B., Oh, S. H. & Lee, S. D. Selective photonic printing based on anisotropic Fabry-Perot resonators for dual-image holography and anti-counterfeiting. Optics Express, **27**(17), 24512-24523 (2019).

[21] Wang, Y., Zhu, X., Chen, Y., Shi, H., Li, Z., Zhang, S., Liu, Q., Li, Y., Xiang, Q. & Duan, H. Fabrication of Fabry-Perot-cavity-based monolithic full-color filter arrays using a template-confined micro-reflow process. Journal of Micromechanics and Microengineering **29**(2), 025008 (2019).

[22] Hedayati, M. K. & Elbahri, M. Review of metasurface plasmonic structural color. Plasmonics, **12**, 1463-1479 (2017).

[23] Yang, B., Cheng, H., Chen, S. & Tian, J. Structural colors in metasurfaces: principle, design and applications. Materials Chemistry Frontiers, **3**(5), 750-761 (2019).

[24] Furukawa, S., Masui, T. & Imanaka, N. Synthesis of new environment-friendly yellow pigments. Journal of Alloys and Compounds, **418**(37), 255-258 (2006).

[25] Fang, Y., Liu, X., Zheng, H. & Liu, H. Eco-friendly colorization of textile originating from polydopamine nanofilm structural color with high colorfastness. Journal of Cleaner Production, **295**(1), 126523 (2021).

[26] Li, Z. B., Clark, A. W. & Cooper, J. M. Dual color plasmonic pixels create a polarization controlled nano color palette. ACS Nano, **10**(1), 492-498 (2016).

[27] Xu, T., Wu, Y. K., Luo, X. & Guo, L. J. Plasmonic nanoresonators for high-resolution colour filtering and spectral imaging. Nature Communications, **1**, 59 (2010).

[28] Shrestha, V. R., Lee, S. S., Kim, E. S. & Choi, D. Y. Polarization-tuned dynamic color filters incorporating a dielectric-loaded aluminum nanowire array. Scientific Reports, **5**, 12450 (2015).

[29] Lim, K. T. P., Liu, H., Liu, Y. & Yang J. K. W. Holographic colour prints for enhanced optical security by combined phase and amplitude control. Nature Communications, **10**, 25 (2019).

[30] Zhang, F., Pu, M., Gao, P., Jin, J., Li, X., Guo, Y., Ma, X., Luo, J., Yu, H. & Luo, X. Simultaneous full-color printing and holography enabled by centimeter-scale plasmonic metasurfaces. Advanced Science, **7**(10), 1903156 (2020).

[31] Kim, D. Y., Choi, S., Cho, H. & Sun, J. Y. Electroactive soft photonic devices for the synesthetic perception of color and sound. Advanced Materials, **31**(2), 1804080 (2019).

[32] Banisadr, S., Oyefusi, A. & Chen, J. A versatile strategy for transparent stimuli-responsive interference coloration. ACS Applied Materials & Interfaces, **11**(7), 7415-7422 (2019).

[33] Wu, Y. K. R., Hollowell, A. E., Zhang, C. & Guo, L. J. Angle-insensitive structural colours based on metallic nanocavities and coloured pixels beyond the diffraction limit. Scientific Reports, **3**, 1194 (2013).

[34] Ellenbogen, T., Seo, K. & Crozier, K. B. Chromatic plasmonic polarizers for active visible color filtering and polarimetry. Nano Letters, **12**(2), 1026-1031 (2012).

[35] Odintsova, G. V., Vlasova, E. A., Andreeva, Y. M., Moskvin, M. K., Krivonosov, A. S., Gorbunova, E. V., Pankin, D. V., Medvedev, O. S., Sergeev, M. M., Shchedrina, N. N., Lutoshina, D. S. & Veiko, V. P. High-resolution large-scale plasmonic laser color printing for jewelry applications. Optical Express, **27**(3), 3672-3681 (2019).

[36] Rezaei, S. D., Ho, J., Naderi, A., Yaraki, M. T., Wang, T., Dong, Z., Ramakrishna, S. & Yang, J. K. W. Tunable, cost-effective, and scalable structural colors for sensing and consumer products. Advanced Optical Materials, **7**(20), 1900735 (2019).

[37] Kenanakis, G., Mavidis, Ch. P., Vasilaki, E., Katsarakis, N., Kafesaki, M., Economou, E. N. & Soukoulis, C. M. Perfect absorbers based on metal-insulator-metal structures in the visible region: a simple approach for practical applications. Applied Physics A, **123**, 77 (2017).

[38] Li, Z. Y., Butun, S. & Aydin, K. Large-area, lithography-free super absorbers and color filters at visible frequencies using ultrathin metallic films. ACS Photonics, **2**(2), 183-188 (2015).

[39] Kajtár, G., Kafesaki, M., Economou, E. N. & Soukoulis, C. M. Theoretical model of homogeneous metal-insulator-metal perfect multi-band absorbers for the visible spectrum. Journal of Physics D: Applied Physics, **49**(5), 055104 (2016).

[40] Kats, M. A., Byrnes, S. J., Blanchard, R., Kolle, M., Genevet, P., Aizenberg, J. & Capasso, F. Enhancement of absorption and color contrast in ultra-thin highly absorbing optical images. Applied Physics Letters, **103**, 101104 (2013).

[41] Kats, M. A. & Capasso, F. Optical absorbers based on strong interference in ultra-thin films. Laser & Photonics Reviews, **10**(5), 735-749 (2016).

[42] Zhao, Z., Bai, J., Yao, Y. & Wang, C. Printing continuous metal structures via polymer-assisted photochemical deposition. Materials Today, **37**, 10-17 (2020).

[43] Barrie, J. D., Fuqua, P. D., Folgner, K. A. & Chu, C. T. Control of stress in protected silver mirrors prepared by plasma beam sputtering. Applied Optics, **50**(9), C135-C140 (2011).

[44] Jeong, E., Zhao, G., Yu, S. M., Lee, S. G., Bae, J. S., Park, J., Rha, J., Lee, G. H. & Yun, J. Minimizing optical loss in ultrathin Ag films based on Ge wetting layer: insights on Ge-mediated Ag growth. Applied Surface Science, **528**, 146989 (2020).

[45] Chen, W., Thoreson, M. D., Ishii, S., Kildishev, A. V. & Shalaev, V. M. Ultra-thin ultra-smooth and low-loss silver films on a germanium wetting layer. Optics Express, **18**(5), 5124-5134 (2010).

[46] Jiran, E. & Thompson, C. V. Capillary instabilities in thin films. Journal of Electronic Materials **19**, 1153-1160 (1990).

[47] Barman, B., Dhasmana, H., Verma, A., Kumar, A., Chaudhary, S. P. & Jain, V. K. Formation of plasmonic silver nanoparticles using rapid thermal annealing at low temperature and study in reflectance reduction of Si surface. Advances in Natural Sciences: Nanoscience and Nanotechnology, **8**(3), 035010 (2017).

[48] Reshetnyak, V. Y, Pinkevych, I. P., Sluckin, T. J., Urbas, A. M. & Evans, D. R. Effective medium theory for anisotropic media with plasmonic core-shell nanoparticle inclusions. The European Physical Journal Plus, **133**, 373 (2018).

[49] Vodnik, V., Bozanic, D. K., Dzunuzovic, J. V., Vukoje, I. & Nedelijkovic, J. Silver/polystyrene nanocomposites: optical and thermal properties. Polymer Composites, **33**(5), 782-788 (2012).

[50] Al-Ramadhan, Z. A., Salman, J. A. & Humd, H. A. K. Optical and morphological properties of (PVA-PVP-Ag) nanocomposites. International Journal of Science and Research (IJSR), **5**(3), 1828-1836 (2016).

[51] Albaladejo, S., Marqués, M. I. & Sáenz, J. J. Light control of silver nanoparticle's diffusion. Optics Express, **19**(12), 11471-11478 (2011).

[52] Dahmouchène, N., Coppee, S., Voue, M. & Coninck, J. D. Silver nanoparticles embedded in polymer matrices-a FTIR-SE study. Physica Status Solidi (c), **5**(5), 1210-1214 (2008).

[53] Wankhede, Y. B., Kondawar, S., Thakare, S. R. & More, P. Synthesis and characterization of silver nanoparticles embedded in polyaniline nanocomposite. Advanced Materials Letters, **4**(1), 89-93 (2013).

[54] Li, W. D., Wang, C., Jiang, Z. H., Chen, L. J., Wei, Y. H., Zhang, L. Y., Chen, M. Y., Yang, X. & Zhang, G. J. Stereolithography based additive manufacturing of high-k polymer matrix composites facilitated by thermal plasma processed barium titanate microspheres. Materials & Design, **192**, 108733 (2020).

[55] Jang, J., Badloe, T., Yang, Y., Lee, T., Mun, J. & Rho, J. Spectral modulation through the hybridization of Mie-scatterers and quasi-guided mode resonances: realizing full and gradients of structural color. ACS Nano, **14**(11), 15317-15326 (2020).

[56] Yu, Y., Yan, C. & Zheng, Z. J. Polymer-assisted metal deposition (PAMD): a full-solution strategy for flexible, stretchable, compressible, and wearable metal conductors. Advanced Materials, **26**(31), 5508-5516 (2014).

[57] Chou, N., Jeong, J. & Kim, S. Crack-free and reliable lithographical patterning methods on PDMS substrate. Journal of Micromechanics and Microengineering, **23**(12), 125035 (2013).

[58] Loo, Y. L., Willett, R. L., Baldwin, K. W. & Rogers, J. A. Additive, nanoscale patterning of metal films with a stamp and a surface chemistry mediated transfer process: Applications in plastic electronics. Applied Physics Letters, **81**(3), 562 (2002).

CHAPTER 3

GE-ASSISTED TRANSFER PRINTING (GTP) OF METALLIC APERTURES FOR OPTICAL APPLICATIONS

3.1 Introduction

Transfer printing has been widely studied as an economical approach for the direct fabrication of micro- and nano-scaled metallic structures without employing conventional patterning processes [59,60], including physical vapor deposition (PVD), photo- or electron-beam lithography (EBL), metal lift-off, and/or dry-etching, which are usually complicated, time-consuming, and potentially costly. Furthermore, the transfer printing process does not necessarily require elevated temperature and complex chemistry, e.g., photoresist, organic solvent, developer, etc. [60]. Therefore, this technology can be utilized for various ranging of applications such as micro/nano-electro-mechanical systems (MEMS/NEMS) [61-63], biological sensors [64,65], plastic display devices [66,67], and optoelectronic devices [68,69]. In a typical transfer printing process, a noble metal, i.e., gold (Au) and silver (Ag), is first deposited on the pre-structured stamp/donor substrates. The metal layer only on the protruded structures is delaminated using the intermediate template, e.g. polydimethysilane (PDMS), then the metal on the template is transferred to the target/acceptor substrates using external forces such as heat or pressure. Due to this unique mechanism, transfer printing usually avoids the deposition of an adhesion layer, e.g. chromium (Cr) and titanium (Ti), to allow the ease of delamination of metal from the donor substrate, which bounds its structural shapes in simple geometries such as gratings,

disks, and squares [70-73] due to the challenge in maintaining complex shapes without adhesion layer. Recently, the transfer printing process for arbitrary shapes has been reported, however, it required EBL for each transfer process, which is unsuitable for cost-effective manufacturing [74].

Arbitrary metallic nano-aperture structures, e.g., bowtie nano-aperture, consisting of two triangular arms pointing to each other and separated by a nano-sized gap, have great attention due to their geometrical advantages, i.e., significantly enhanced electromagnetic field and light confinement at the nano-sized gap via strong coupling effect [75-77]. Therefore, these unique structures can be potentially used for various optical applications such as optical lithography [78,79], single photon emission [80,81], data storage [82], and others where high-efficiency near-field enhancement are essential. Despite those theoretical advantages, scalable manufacturing of metallic apertures still remained challenging due to the required complicated fabrication processes, e.g., EBL, Focus-ion-beam (FIB) milling, and reactive-ion-etching (RIE) of metallic film, which possibly induced lengthy process and high-cost in manufacturing.

In this chapter, the use of inexpensive and scalable transfer printing technology will be demonstrated for the fabrication of arbitrary metallic nano-aperture structures. An ultra-thin germanium (Ge) is utilized as a nucleation layer prior to the deposition of noble metals to minimize the migration of metal atoms during the initial deposition process, which yields a smoother surface and prevents pattern distortion. A water-soluble polymer (polyvinyl alcohol, PVA) is used as a dominant metal transfer layer, which facilitates avoiding any

form of chemistry during the printing process. Importantly, the demonstrated transfer printing has the capability of direct patterning of metallic structures from simple gratings to arbitrary bowtie structures with a sub-100 nm resolution and up to 50 nm thickness. This new printing technology is expected to have broad use in high throughput optical lithography, bio-sensors, and quantum emitter system with high resolution and low cost. The transferable resolution and thickness limits will be further investigated in the future studies.

3.2 Effect of Ge on Metallic Thin Film

Germanium (Ge) has been widely utilized as a nucleation (or wetting) layer for noble metals, especially Ag, in various optical applications [83-85]. Due to its relatively higher surface energy than that of Ag and SiO_2, it effectively suppresses the migration of Ag atoms at the surfaces during the initial stage of metal deposition [83]. Consequently, the deposited Ag thin film on the Ge nucleation layer tends to be significantly smoother and exhibits a lower percolation threshold than the Ag film on SiO_2. In addition to this advantage, it was experimentally observed that Ge also allowed maintaining arbitrary shapes when Ag was deposited on the pre-fabricated dielectric nano-apertures as it provided sufficient nucleation sites at the edge of bowtie to avoid the accumulation of Ag atoms at the edges (Figure 3.1). Furthermore, the Ag film without a Ge nucleation layer indicated a much larger grain size than the one with Ge and generated many nano-cracks on the deposited film surface, which would potentially behave as scattering sites of the incident light, resulting in huge optical loss [86]. Therefore, it is essential to use the Ge nucleation layer

to successfully transfer intact arbitrary metallic nano-apertures with improved optical performance in this demonstration.

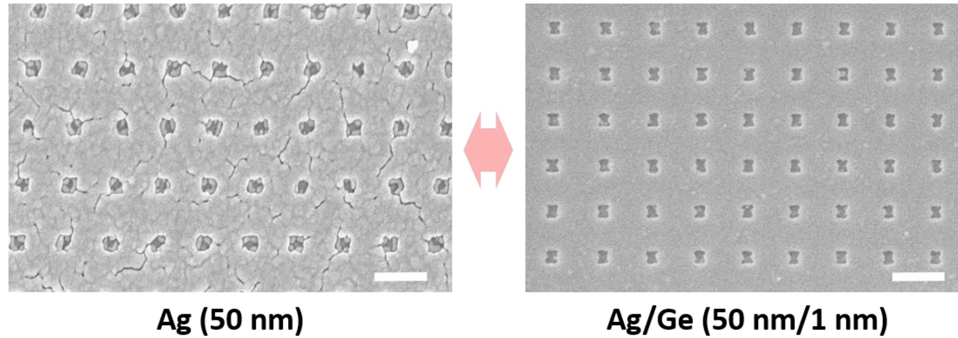

Figure 3.1: The effect of Ge nucleation (or wetting) layer. Left: Ag (50 nm) deposited without Ge on the fabricated SiO_2 apertures, right: Ag (50 nm) deposited with Ge (1 nm) on the same apertures. Scale bar: 500 nm.

3.3 GTP Process for Metallic Nano-apertures

The Ge-assisted transfer printing (GTP) was developed by employing a polymeric bi-layer (PVA/poly(methyl-methacrylate) (PMMA)) on a PDMS substrate as the intermediate template. To prepare PDMS, self-assembled monolayers (SAMs) were formed on the bare Si substrate using trichloro(1*H*,1*H*,2*H*,2*H*-perfluorooctyl)silane at 100 ℃ for 30 min as an anti-sticking layer followed by solvent and RCA-1 cleaning. A mixture of Sylgard 184 silicone elastomer and its curing agent (10:1 wt/wt) was poured onto it after cooling the Si substrate, degassed, and further cured at 70 ℃ for 6 h. The cured PDMS (1 ~ 1.5 mm thickness) was gently peeled off from the substrate, and cut into squares for easy handling during the printing process. A µm-thick PVA layer was used as a dominant contact layer to metallic structures, and it was later dissolved in water [87,88]. A 100 nm-thick PMMA

layer was utilized to promote the adhesion between PVA and PDMS substrate for easier delamination of the metallic layer with the template. The GTP process was carried out using the pre-fabricated dielectric nano-apertures as a donor substrate to demonstrate its feasibility of transferring arbitrary metallic nano-apertures (Figure 3.2). First, the SAMs were formed on the donor substrate surface as the same as the aforementioned, then the ultra-thin Ge nucleation layer and Ag film, respectively, were deposited onto the substrate with the thermal evaporator (Denton Benchtop turbo). 4 wt% PMMA was spin-coated on PDMS substrate as an adhesion promoter layer, subsequently, 20 wt% aqueous solution of PVA (Sigma-Aldrich, M_w 9,000 – 10,000, 80 % hydrolyzed) was applied by spin coating on the PMMA layer immediately, and air dried for 1 min to semi-solidify the film. Then, the PVA/PMMA/PDMS template was placed on the donor substrate and gently rubbed by a tweezer at a moderate temperature (60 ℃) to induce slight melting of the PVA film, which resulted in strong contact of the template onto the top metal layer. The template was quickly delaminated from the donor substrate and transferred to a pre-cleaned acceptor substrate. Since the adhesion of Ge to semiconductor or dielectric substrates was relatively lower than other adhesion layers, e.g., Cr and Ti, it allowed the ease of delamination of the whole template with metal layer [84]. The elevated heating (90 ℃) and pressure (750 KPa) were applied to the acceptor substrate and template assembly using the nanoimprinter (THU400, Zhenjiang Lehua Electronic Technology Co. Ltd.) for 5 min to increase the bonding strength of transferred metal to the substrate. After cooling down the assembly, a small amount of water was applied at the edge of the assembly to detach the template. Remarkably, water penetrated between hydrophobic metal and hydrophilic PVA surfaces, which facilitated the delamination of the template without damaging transferred metal film

[89]. Finally, the acceptor substrate was immersed in warm water (60 ℃) for 2 hours to remove the PVA residual completely. Importantly, the donor substrate could be reused followed by metal stripping and substrate cleaning for another GTP process utilizing either the same material or different ones without additional patterning processes such as EBL and FIB, which would be also considered as the superior advantage of the developed GTP process.

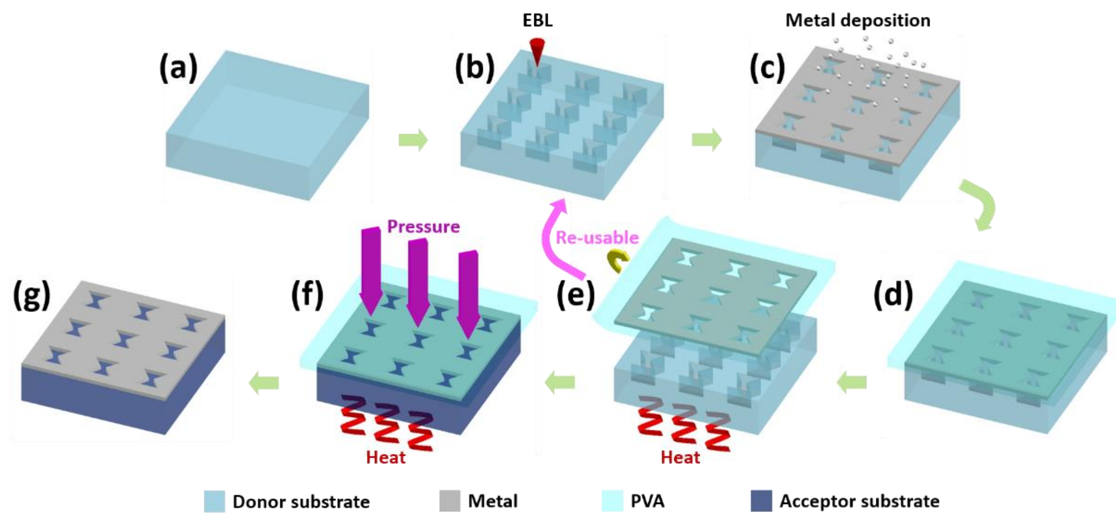

Figure 3.2: Schematic illustration of Ge-assisted transfer printing (GTP). (a-b) Fused silica wafers were carefully cleaned, and nano-structures were fabricated, followed by EBL and sequential RIE steps. (c) SAM layer was formed on the donor substrate, then Ag/Ge (50 nm/1 nm) was deposited. (d) PVA/PMMA on PDMS template was placed on the donor substrate. (e-f) The template was carefully peeled off and transferred to the acceptor substrate. Elevated temperature and pressure were applied for the bonding process. (g) The template was removed by water penetration between metal and PVA surfaces. Residual PVA was removed in warm water (60 ℃) for 2 hours.

3.4 Demonstration of GTP

3.4.1 Nano-gratings for Silver (Ag) Transfer

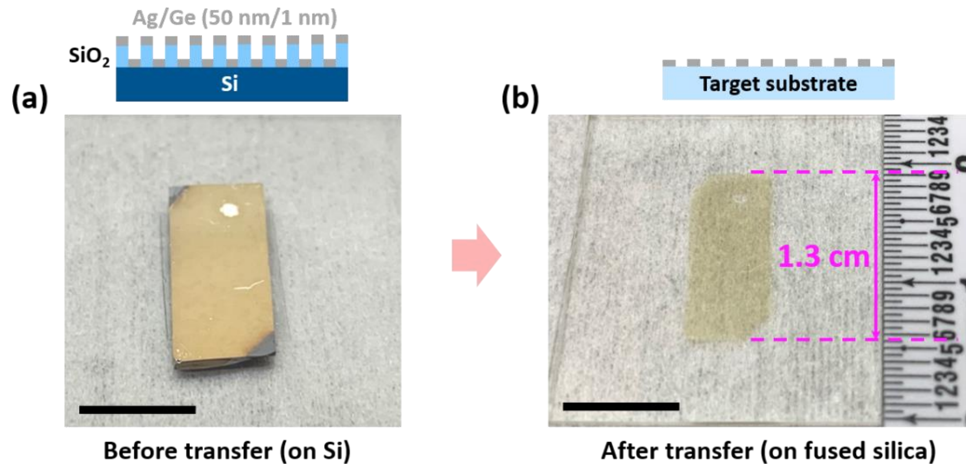

Figure 3.3: Experimental demonstration of GTP using pre-fabricated nano-gratings. Photographic images of Ag/Ge (50 nm/1 nm) on (a) SiO_2/Si donor substrate (before transfer) and (b) fused silica acceptor substrate (after transfer). Scale bar: 1 cm.

To demonstrate the GTP process for transferring nano-scaled features, the pre-fabricated dielectric, i.e., SiO_2, nano-grating structures (period of 200 nm & height of 130 nm) was used as a donor substrate. 1 nm Ge and 50 nm Ag were deposited on the pre-cleaned donor substrate, followed by the formation of SAMs, then the GTP process was carried out as the above elucidation. Remarkably, the Ag nano-gratings were successfully transferred from the donor to the acceptor substrate in centimeter scale (0.7 cm × 1.3 cm) (Figure 3.3), which strongly implied the capability of the GTP process for scalable manufacturing of nano-scaled metallic structures.

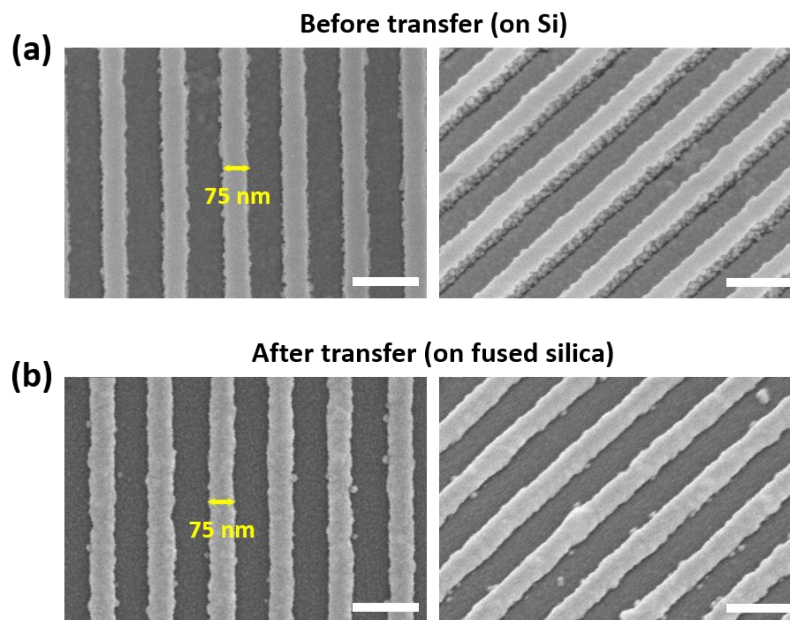

Figure 3.4: SEM images of (a) SiO_2/Si donor substrate (before transfer) and (b) fused silica acceptor substrate (after transfer). Scale bar: 200 nm.

Scanning electron microscopy (SEM, Hitachi S-4700 FESEM) was employed for further characterize of the GTP process. The linewidth of transferred Ag nano-gratings, i.e., 75 nm, on the acceptor substrate was observed to be consistent with the one on the donor substrate according to the SEM images (Figure 3.4), indicating good pattern transfer feasibility of the developed GTP process. Noticeably, the transferred Ag nano-gratings had relatively small defect density within 1 μm^2 area (less than 1 %) due to the advantage of using water-soluble PVA as a template, prevented the possible degradation of optical performance, which possibly occurred by leftover residues during the transfer process. Interestingly, the line edge of transferred Ag nano-gratings was found to be slightly smoother and rounded compared to the ones on the donor substrate from the tilted SEM

images (Figure 3.4), because the applied external heat and pressure during the bonding process probably caused gentle deformation of nano-scaled structures [90].

3.4.2 Nano-gratings for Gold (Au) Transfer

Au was employed as a source material for this experiment to investigate the versatility of GTP for various materials. The same structural nano-gratings as the above were used with a larger area. Remarkably, 1 nm Ge and 50 nm Au nano-gratings were also successfully transferred via the GTP process with a centimeter scale (Figure 3.5(a) and (b)), although partially non-transferred areas were found on the transferred structures. A contact between the template and the top metal layer was formed by gentle rubbing of the tweezer, inducing possible trapped air and non-uniformly flow of melted PVA at the contact surface, which possibly yielded a non-transferrable area. To further improve this phenomenon, a non-sticky rubber roller would be employed to gently and uniformly press the template instead of using a tweezer [91].

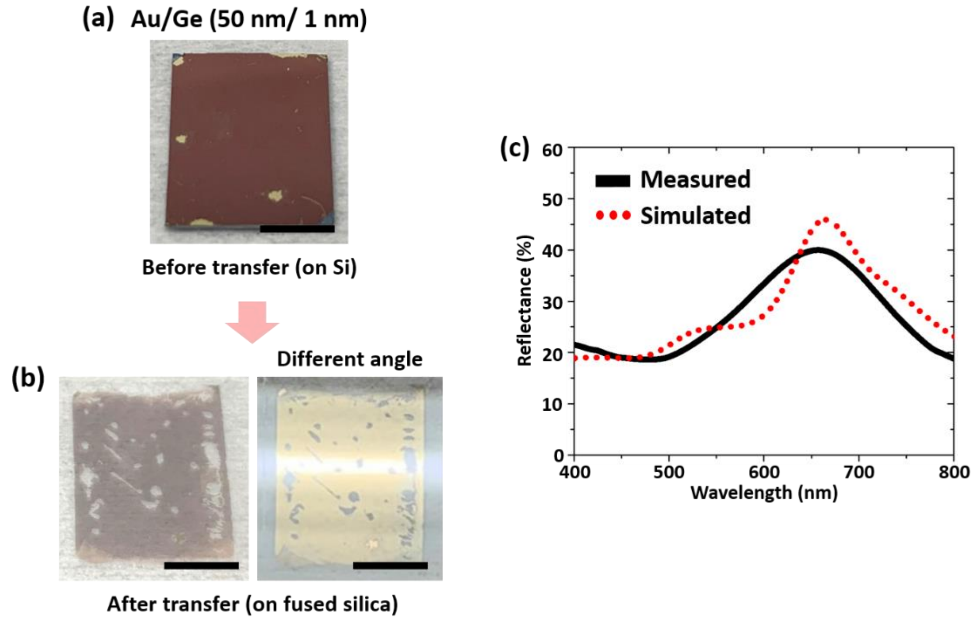

Figure 3.5: Experimental demonstration of the versatility of GTP using pre-fabricated nano-gratings. Photographic images of Au/Ge (50 nm/1 nm) on (a) SiO_2/Si donor substrate (before transfer) and (b) fused silica acceptor substrate (after transfer). Scale bar: 1 cm. (c) FDTD simulated reflectance spectra (red dotted lines) and experimentally measured reflectance spectra (black solid lines) for transferred nano-gratings.

FDTD simulations for transferred Au nano-gratings were conducted to investigate the quality of transferred Au nano-gratings. Periodic boundary conditions ($\pm x$, $\pm y$ direction) and perfectly matched layers ($\pm z$ direction, parallel to the propagation of electromagnetic waves) were used within a unit cell of 400 nm along the $\pm x$ and $\pm y$ direction. The unit cell consisted of Au nano-gratings and fused silica substrate. The plane wave in the visible wavelength range (400 – 800 nm) was used as the light source, which was incident perpendicular to the unit cell. The mesh sizes were set as 5 nm along the $\pm x$ and $\pm y$ directions and 1 nm along $\pm z$ direction. The Johnson and Christy model was employed for

calculation. The reflectance was monitored in the x–y plane, ~1000 nm away from the top surface of the structure. The reflectance spectra were examined by an ultra-violet-visible (UV-Vis) spectrometer (Horiba iHR320 imaging spectrometer) (Figure 3.5(c)). Noticeably, the measured reflectance spectra (black solid line) were consistent with simulated spectra (red dotted line), despite small discrepancies possibly attributed to differences in structural geometries and material properties between simulations and experiments. Nevertheless, these results convincingly implied that GTP would possibly have a broad range of material libraries for scalable and cost-effective manufacturing of high-quality nano-scaled metallic structures.

3.5 GTP for Arbitrary Bow-tie Nano-aperture

3.5.1 Dielectric Nano-aperture Fabrication

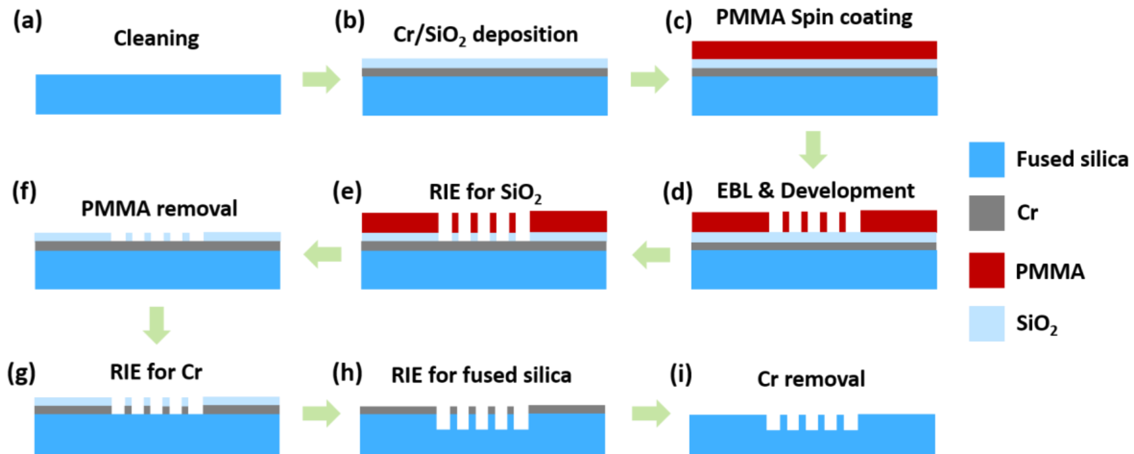

Figure 3.6: Bow-tie nano-aperture fabrication process flow. (a-b) Fused silica wafers were carefully cleaned, and Cr/SiO_2 was deposited. (c-d) PMMA was spin-coated, then EBL was carried out. (e-i) Sequential RIE steps were used to etch the SiO_2, Cr, and fused silica to create the nano-apertures. Then, Cr was removed.

To further study the feasibility of the GTP for transferring arbitrary structures, the dielectric bowtie nano-apertures were fabricated as the donor substrate (Figure 3.6). Fused silica substrate was solvent and RCA-1 cleaned to remove absorbed organic and inorganic contaminants. 10 nm Cr and 15 nm SiO_2 layers were deposited by using an electron beam (e-beam) evaporator (Kurt J. Lesker), respectively, without breaking the vacuum. The polymethyl methacrylate (PMMA) was spin-coated (PS-80, Headway Research Inc.) on the substrate post-baked 5 min at 180 ℃. The EBL was carried out (Jeol JBX-6000 FS/E) with an acceleration voltage of 50 kV and a beam current of 1 nA with a minimum step size of 10 nm. The various doses ranging from 600 μC cm^{-2} to 1100 μC cm^{-2} were used for exposure. After EBL, the patterns were developed in a 1:3 ratio (v/v) of methyl isobutyl ketone (MIBK)/isopropyl alcohol (IPA) solution for 2 minutes, rinsed in IPA, and dried with nitrogen blow. SiO_2 interlayer was etched by reactive-ion-etcher (RIE) (PlasmaTherm 790, CHF_3 = 25 sccm, O_2 = 1 sccm, 10 mTorr, 100 W) using PMMA as a hard mask. PMMA was stripped by remover PG for 30 min at 70 ℃, and oxygen plasma cleaning was employed (Tergeo plasma cleaner, 75 W, O_2 = 5 sccm) for 3 min to remove any contaminants on the sample completely. Then, Cr was dry-etched by RIE (Oxford 80, Cl_2 = 9 sccm, O_2 = 3 sccm, 10 mTorr, 150 W) using SiO_2 interlayer as a hard mask. Fused silica and SiO_2 interlayer were simultaneously etched together by RIE (PlasmaTherm 790, CHF_3 = 40 sccm, O_2 = 3 sccm, 40 mTorr, 250 W). Finally, a Cr hard mask was stripped by Cr etchant, and dielectric nano-apertures were fabricated as the donor substrate for the GTP process.

3.5.2 Characterization of Transferred Ag Nano-aperture

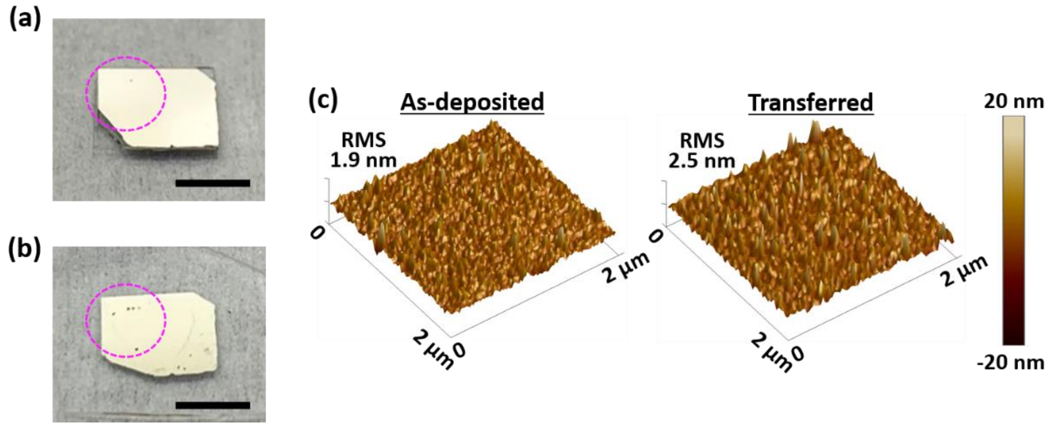

Figure 3.7: Experimental demonstration of GTP for arbitrary shape. Photographic images of Ag/Ge (50 nm/1 nm) on (a) donor substrate and (b) acceptor substrate. Pink dotted circles indicated the area of bowtie arrays. Scale bar: 5 mm. (c) 3D profile of AFM images for as-deposited Ag film (top) and transferred Ag film (bottom).

1 nm Ge and 50 nm Ag were deposited on the fabricated donor substrate, followed by the formation of SAMs, and then the top metal layer was transferred to bare fused silica substrate to fabricate Ag nano-apertures via the developed GTP process as the above explanation. Atomic force microscopy (AFM, Bruker Dimension, tapping mode, scan rate of 1 Hz) was used to investigate the surface morphology and roughness of the as-deposited and transferred Ag films (Figure 3.7). The transferred Ag film was found to be comparable to but slightly rougher (Root-mean-square (RMS) roughness 2.5 nm) than the as-deposited Ag film (RMS roughness 1.9 nm), as depicted in Figure 3.7(c). This minor difference could be attributed to the minimal deformation of Ag film, which might occur by heat and pressure during the bonding process rather than the remaining PVA or PMMA residues

[90]. Remarkably, various metallic structures were accomplished by utilizing the simple GTP process, evidently observed by SEM imaging (Figure 3.8). The 'before transfer' structure could be fabricated through simple metal deposition on the dielectric nano-apertures. However, 'buried' and 'after transfer' (Ag nano-apertures) structures required significantly complicated fabrication processes, e.g. EBL, metal deposition, lift-off, and RIE etching, which potentially increases manufacturing time and cost. Therefore, the developed GTP process would provide simpler and more degrees of freedom fabrication for various metallic structures.

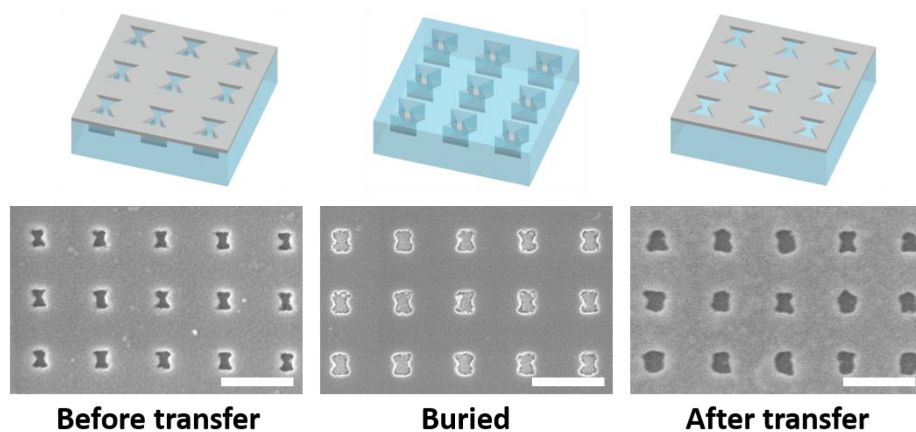

Figure 3.8: SEM images of various metallic structures accomplished by the GTP. Scale bar: 500 nm.

Finally, FDTD simulations were conducted with the empirically measured structural dimensions to calculate the transmittance spectra and compared with the spectra measured by the UV-Vis spectrometer (Figure 3.9(d)). Remarkably, the measured transmittance spectra (solid lines) clearly indicated polarization-dependent resonances in terms of

transmittance, e.g., the resonance found at 680 nm with the transmittance of 35 % with 0°, on the other hand, the one found at 850 nm with the transmittance of 27 % with 90° from 'Buried' structure (Figure 3.9(b)), which was consistent with simulated spectra (dotted lines) for the all three different structures. Despite slightly different structural geometries and material properties possibly inducing small discrepancies between simulations and experiments, these results addressed that the high quality of transferred arbitrary metallic structures was successfully accomplished by the GTP process with the capability of a wide range of tunable optical resonances.

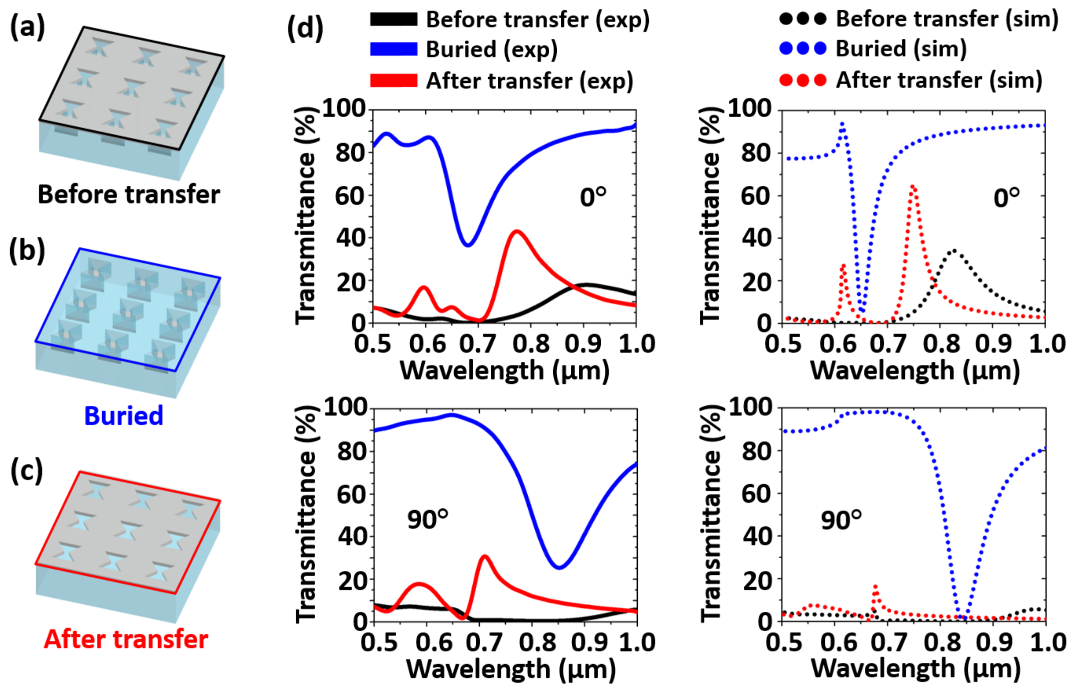

Figure 3.9: Simulated and experimentally measured spectra. (a-c) Corresponding structures for each spectrum. (d) Measured (solid lines) and simulated (dotted lines) transmittance spectra according to polarization angle. Top: 0° and bottom: 90° along the x-direction.

3.6 Summary

In summary, a new approach to fabricating nano-scaled metallic apertures has been demonstrated by employing a scalable and cost-effective GTP process. The ultra-thin Ge layer acted well as a nucleation layer during Ag thin film deposition, which facilitated smoother surface morphology and maintained arbitrary aperture shape. The developed GTP could effectively transfer sub-100 nm resolution structures with a centimeter scale and had the versatility to transfer various noble metals, e.g. Ag and Au. The GTP for arbitrary structures was also successfully demonstrated using the fabricated dielectric nano-aperture as the donor substrate. Various metallic structures with a wide range of tunable optical resonances were accomplished by simply the GTP process. These demonstrations strongly implied that the developed GTP process would be employed as an alternative method of manufacturing metallic nano-aperture structures as a fast, scalable, and cost-effective method in a wide range of optical applications, including optical lithography, fluorescence enhancement, and single photon detection system.

CHAPTER 4

SCALABLE MANUFACTURING FOR ULTRA-COMPACT POLARIMETRIC IMAGING SYSTEM USING NANOIMPRINT LITHOGRAPHY

4.1 Introduction

Polarimetric imaging system, which characterizes polarization states of light scattered from the objectives, has been received great attention in various research fields such as remote sensing [92,93], target detection [94-96], underwater vision [97,98], and biomedical diagnostics [99-101], which are usually being a challenge to be monitored by conventional intensity-based imaging system. Traditional polarimetric imaging systems are usually bulky due to the required several optical components such as polarizers and waveplates to characterize circularly polarized light (CPL) for full stokes polarimetric operation, which limits the size of the imaging system [102]. With the development of state-of-the-art micro/nanofabrication technology, an ultra-compact polarimetric imaging system has been accomplished by utilizing double-layered metasurface structures [103-105]. The chiral metasurface is integrated with linear polarization (LP) filters and works as a quarter waveplate on the same device, which enables detecting CPL directly without additional optical components and ultra-compactness of the device. Therefore, this structure can provide the full stokes polarimetric imaging operation and eligibility of on-chip integration with complementary metal-oxide-semiconductor (CMOS) imaging sensor [106].

To engineer full stokes polarimetric imaging using double-layered metasurface structures, requires precisely defined structural dimensions at nanometer scale and accurately aligned two metasurfaces to characterize each polarization state [105,106]. Electron beam lithography (EBL) has been widely used to fabricate nm-scaled metasurfaces, and a dielectric layer, e.g., silicon dioxide (SiO_2), is typically deposited using sputtering or chemical vapor deposition (CVD) as a spacing layer prior to integrating another metasurface on it. This process demonstrated the feasibility of integrating two metasurfaces, however, it can seriously increase the whole process time and cost in scalable manufacturing due to the single-line scan nature of EBL. Furthermore, the protruded the first metasurface can cause non-conformal spacing layer deposition, resulting in surface modulation and lowering of device performance such as linear polarization extinction ratios (LPERs) and circular polarization ERs (CPERs) [106]. To overcome the low throughput of EBL process, nanoimprint lithography (NIL) has been chosen as a promising alternative method to fabricate metasurfaces due to its layer-by-layer nature in the patterning process [107]. So far, many researchers have demonstrated their NIL process in a fast and scalable manufacturing of metasurfaces, however, they mostly focused on a single-layer fabrication [108-112]. In a typical NIL process, the mold and substrate are physically pressed together to make a resist be filled into the mold. Due to this unique characteristic, NIL usually requires a flat surface to effectively flow a resist on the surface during the process [113]. However, the formed metasurface generates nm-scaled surface modulation even after a spacing layer deposition, which disrupts the flow of a resist or traps air bubbles during the NIL process for the next layer. Moreover, unlike the EBL process, which enables the dynamic alignment of two metasurfaces by detecting alignment

markers on the substrate using an electron beam [114], the precise control of alignment in NIL is difficult due to the absence of a dynamic alignment method since the mold and substrate move toward each other and are being contacted to pattern the whole structures at once. Therefore, the integration of two metasurfaces using the NIL process for optical applications is still challenging.

In this chapter, the scalable manufacturing process for the polarimetric imaging system composed of double-layered chiral metasurface (DLCM) structures will be demonstrated using the NIL process. The first amorphous silicon (a-Si) metasurface layer is fabricated by employing thermal-NIL with a tri-layer scheme. Then, a mask aligner with Moiré fringe will be utilized to obtain relatively higher alignment accuracy, i.e., less than 200 nm in both x- and y-direction, then conventional photolithography during the second layer ultra-violet (UV) (UV-NIL) process. Importantly, the UV cured resist from the second NIL acts as spacing and planarization layer as well as patterns dielectric, i.e., SiO_x, grating layer simultaneously without any additional fabrication processes, e.g., lift-off, dry-etching, and sputtering deposition, which dramatically reduces potential cost and time in the fabrication process. As deposited aluminum (Al) on the dielectric gratings, the vertically coupled Al double-layered gratings (VCADGs) are fabricated on the first layer without surface modulation due to the planarized spacing layer from the second NIL. Remarkably, the improved device performance, i.e., LPER and CPER, was clearly observed compared to the previously EBL-based fabricated device, expecting to obtain the enhanced polarimetric imaging performance. This new NIL-based metasurface integration technology is expected

to have broad use in several applications such as polarimetric navigation, mirror soiling detection, and polarimetric microscopy system.

4.2 Chip-Integrated Polarimetric CMOS Imaging Sensor

The same design concept was employed from the previous work to demonstrate the scalable manufacturing process for polarimetric imaging sensors [106]. Briefly, the vertically coupled Al double-layered gratings (VCADGs) formed four LP filters and two pairs of the metal-dielectric hybrid chiral metasurface, i.e., top a-Si metasurface, dielectric spacing layer, and bottom VCADGs, made circular polarization (CP) filters in the super-pixel, and then they were bonded on the CMOS sensor, accomplished a chip integrated full stokes polarimetric CMOS imaging sensor (Figure 4.1). In addition to the previous work, another two pairs of CP filters were added, which worked at different wavelengths to enable the sensor operation in the visible wavelength range. Furthermore, the number of super-pixels were enlarged to over 43000 to demonstrate its scalability.

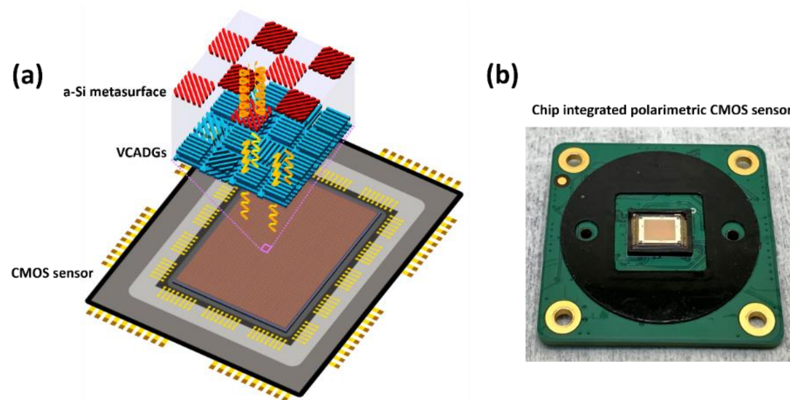

Figure 4.1: Chip-integrated polarimetric CMOS imaging sensor. (a) Conceptual 3D schematic illustration of the desired structures. (b) Photographic image of the fabricated sample bonded onto CMOS image sensor.

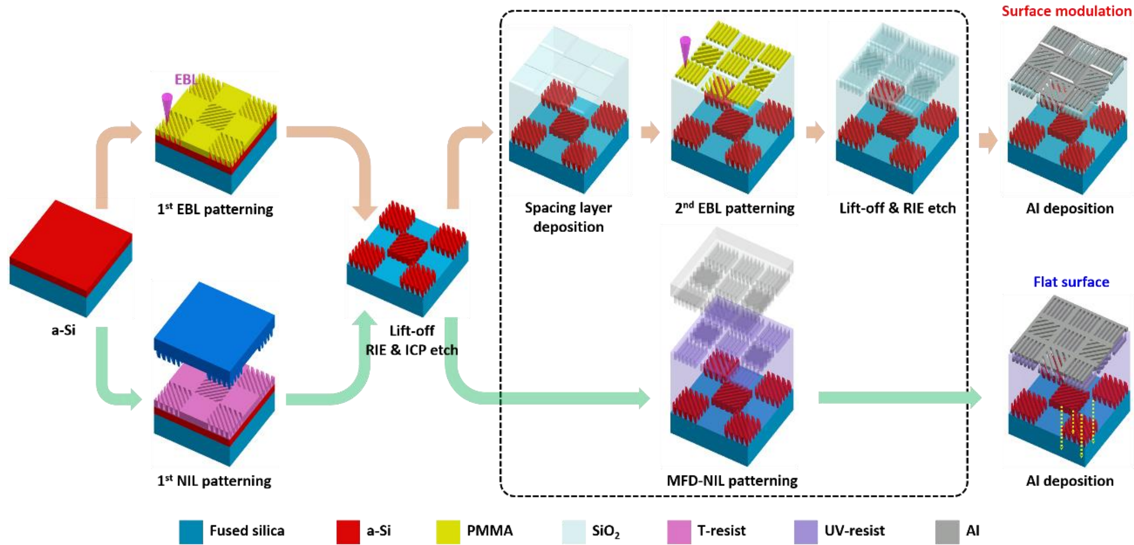

Figure 4.2: Schematic illustration of two different fabrication processes for double-layer chiral metasurface (DLCM). (Orange arrow) Conventional fabrication process based on EBL. (Green arrow) Developed multi-functional-direct (MFD)-NIL process.

In the previous work, the EBL-based conventional process was used for device fabrication (Figure 4.2, indicated process along orange arrows) [106]. In short, the first EBL was carried out, followed by a-Si deposition on a fused silica substrate. The chromium (Cr) hard mask was formed with the Cr deposition and lift-off process, and several dry-etching steps were performed to fabricate the a-Si metasurface. A dielectric, i.e., SiO_2 layer, was sputtered on the formed metasurface as a spacing layer, and the processes mentioned above, e.g., EBL, lift-off, and dry-etching, were repeated to make SiO_2 gratings, then Al was evaporated to form VCADGs structures. These fabrication processes typically resulted in long processing time and increased cost, especially mm-scaled devices, because of extensive EBL writing time due to its line scanning behavior, repeated lift-off and dry-

etching processes for each metasurface, and relatively slow spacing layer deposition process. Moreover, importantly, the deposited SiO_2 spacing layer provided relatively rough and modulated surface for VCADGs over a-Si metasurface due to non-conformal deposition on the formed structures, which seriously degraded device performances, e.g. LPER and CPER, as they were observed previously [106].

To overcome those disadvantages, the new scalable manufacturing technology for polarimetric imaging sensors was developed using the NIL process (Figure 4.2, indicated process along green arrows). The a-Si metasurface was first patterned through the thermal-NIL (T-NIL) process followed by a-Si deposition on the substrate and fabricated as went-through the similar processes as the above EBL-based one. Due to the unique characteristic of the NIL process, mm-scaled nano-structures were patterned with a single pressing of the mold, which significantly reduced the processing time. Remarkably, the multi-functional-direct-NIL (MFD-NIL) process was developed and employed to fabricate VCADGs on the formed a-Si metasurface. Unlike the above complicated EBL-based process, the MFD-NIL process provided several functionalities with a single UV-NIL process. First, the UV resist was pressed by the ultra-flat transparent mold during the NIL process, which served the proper flow of resist on the patterned structures and yielded the planarized surface over the a-Si metasurface. Second, the cross-linked UV resist under the UV exposure became a SiO_x dielectric material which was resistant to solvents and acted as a spacing layer. Third, the SiO_x gratings were simultaneously formed during the NIL process without any additional processes such as lift-off and dry-etching, which tremendously reduced potential cost and time in the fabrication process.

Furthermore, the advanced alignment method employed in the MFD-NIL process resulted in relatively higher alignment accuracy between two metasurfaces. The VCADGs were simply fabricated, followed by Al deposition on the patterned SiO_x gratings, which potentially improved device performance compared to the EBL-based one due to relatively flat surface morphology. Noticeably, the estimated total fabrication time for the same sized device, i.e., 5 mm x 4 mm, using the developed technology was 3.9 times faster than the EBL-based one in a single device fabrication (Table 3.1). Furthermore, the processing time of the developed technology would be maintained the same even with scale-up devices, e.g., 1 cm × 1 cm, because of the layer-by-layer patterning behavior of the NIL process while the EBL based one would be significantly increased due to extensive increment of pattern writing time. This developed new process technology would be expected to dramatically reduce the manufacturing time and potential cost in mass-production with enhanced optical performance in various optical applications.

	a-Si & SiO2 deposition	1st EBL	Cr lift-off	Dry-etch & Cr strip	Spacer deposition	2nd EBL	Cr lift-off	Dry-etch & Cr strip	Al deposition	Estimate time
EBL	0.5	16	2	1.5	4	16	2	1	6	**49**
	a-Si & SiO2 deposition	1st NIL	Tri-layer dry-etch	Cr lift-off	Dry-etch & Cr strip	2nd NIL			Al deposition	Estimate time
MFD NIL	0.5	1.5	1	2	1.5	0.05			6	**12.55**

Table 4.1 Total estimated fabrication processing time for DLCM structures. (Unit: hour)

4.4 Mold Fabrication for NIL

4.4.1 Mold for a-Si Metasurface

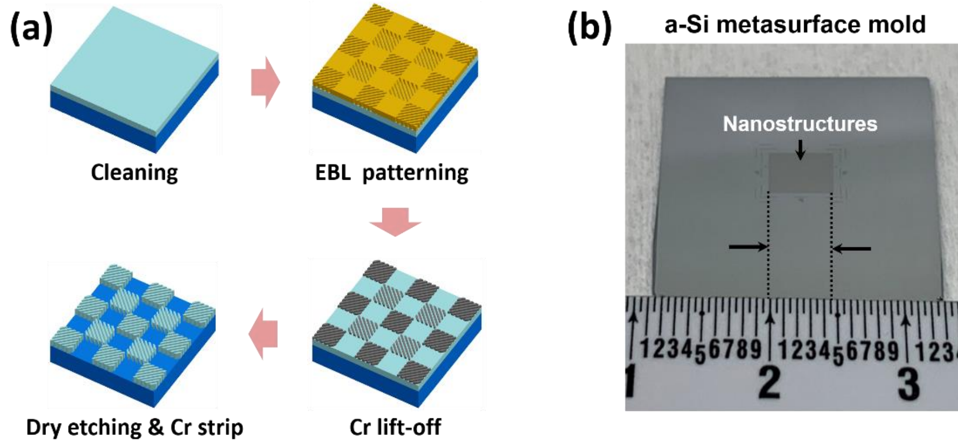

Figure 4.3: Mold fabrication for a-Si metasurface. (a) Schematic illustration of mold fabrication process flow using EBL. (b) Photographic image of fabricated mm-scaled a-Si metasurface mold.

The a-Si metasurface mold for the NIL process was fabricated using EBL (Figure 4.3). The polymethyl methacrylate (PMMA) bi-layer was spin-coated (PS-80, Headway Research Inc.) on the solvent and RCA-1 cleaned SiO_2 on silicon (Si) substrate and post-baked 5 min at 180 ℃. 10 nm Cr layer was deposited as discharging layer for the EBL by using thermal evaporator (Denton Bench Top Turbo, Denton Vacuum, LLC) with a deposition rate of 0.2 Å s^{-1}. The EBL was carried out (ELS-7000, Elionix) with an acceleration voltage of 100 kV, a beam current of 1 nA, and a field size of 300 μm with a minimum step size of 5 nm. An exposure dose of 1200 μC cm^{-2} was used for the entire pattern. After EBL, the patterns were developed in a 1:3 ratio (v/v) of methyl isobutyl

ketone (MIBK)/isopropyl alcohol (IPA) solution for 2 minutes, rinsed in IPA, and dried with nitrogen blow. Then, a 10 nm Cr layer was deposited by using thermal evaporator followed by an oxygen plasma descum (Tergeo plasma cleaner, 20 W, 10 sccm, 40 s) process. The sample was immersed in remover PG solution for 15 minutes at 80 ℃ for the lift-off process, and rinsed with IPA and DI water, respectively. The 80 nm SiO_2 layer was etched by reactive-ion-etcher (RIE) (PlasmaTherm 790, CHF_3 = 40 sccm, O_2 = 3 sccm, 40 mTorr, 250 W) using Cr as a hard mask. Finally, the a-Si mold fabrication was completed as Cr hard mask was stripped by the Cr etchant.

4.4.2 Mold for Vertically Coupled Al Double-layered Gratings (VCADGs)

To fabricate NIL mold for the VCADGs, thick fused silica (6 mm) was chosen rather than a conventional fused silica wafer (500 μm) as the substrate (Figure 4.4). The transparent and thick substrate not only made it feasible for the second layer alignment process but also would minimize mold bending during the NIL process, yielding better imprint uniformity and feature resolution. The sample underwent the same EBL process until the Cr lift-off step as the a-Si metasurface, except for exposure doses due to different feature dimensions. Followed by Cr lift-off, 150 nm fused silica was etched by RIE using the same recipe as aforementioned. Noticeably, the MESA structure (1.5 cm^2, height = 2 μm) was intentionally fabricated with an additional RIE process to accumulate pressure in the imprint region. To investigate this phenomenon, the test mold was fabricated, and NIL was performed with and without the MESA structure. Remarkably, the mold with MESA provided uniformly imprinted structures up to a centimeter scale (Figure 4.5(a)). From the

optical microscopic images, the imprinted a-Si metasurface at the center and edges (1 cm apart from each other) showed similar colors, which indicated the similar thickness of resist after the NIL process (Figure 4.5(b)). The color difference at the edge #1 was due to the initial defect, as indicated as red arrow, which prevented resist flow during the NIL.

Both molds were solvent and RCA-1 cleaned, and they were treated using trichloro(1*H*,1*H*,2*H*,2*H*-perfluorooctyl)silane in the vacuum oven for 30 min at 100 ℃ to form the self-assembled monolayers (SAMs) on the surface which acted as an anti-sticking layer during the NIL process [115].

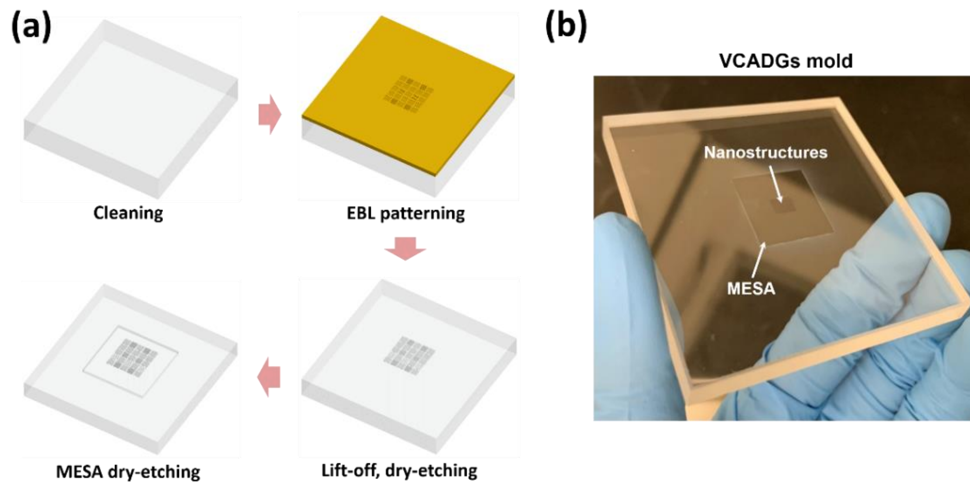

Figure 4.4: Mold fabrication for VCADGs. (a) Schematic illustration of mold fabrication process flow using EBL. (b) Photographic image of fabricated mm-scaled VCADG mold.

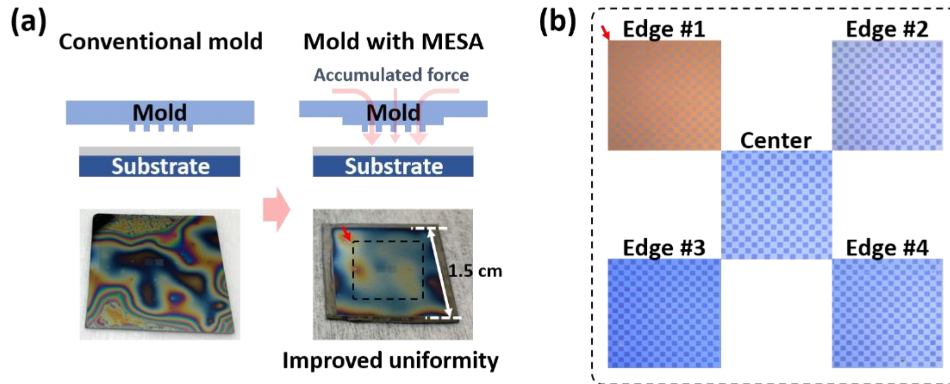

Figure 4.5: NIL with a conventional mold and a MESA mold. (a) Simple schematic illustration of the mold with and without MESA (top) & photographic images of imprinted structures on Si substrate (bottom). (b) Microscopic images of imprinted arrays of nano-structures using MESA mold at five different points.

4.5 Fabrication of Metasurfaces Using NIL

4.5.1 a-Si Metasurface by T-NIL

The a-Si metasurface was fabricated using T-NIL with a tri-layer scheme (Figure 4.6). Prior to the T-NIL process, 130 nm a-Si was deposited on the pre-cleaned fused silica substrate using plasma-enhanced CVD (PECVD) (Oxford Plasmalab 100, SiH_4 = 480 sccm, 1200 mTorr, 15 W, 350 ℃) and 60 nm SiO_2 was continuously deposited as a hard mask using the same system (SiH_4 = 170 sccm, N_2O = 710 sccm, 1000 mTorr, 20 W, 350 ℃) without breaking chamber vacuum. After the substrate preparation, the tri-layer structure was employed for the T-NIL process. The tri-layer structure has been widely used in the NIL process due to its various advantages, such as high etching selectivity to imprint resist, convenient resist strip, and large-scale pattern uniformity [116-118]. The developed tri-layer structure consisting of solvent-soluble polymer (PMMA), SiO_2, and lab-made

thermal resist (T-resist) would improve pattern uniformity for scalable manufacturing. The PMMA 950 A2 was spin-coated on the substrate with an acceleration speed of 4000 rpm and post-baked 5 min at 200 ℃ on the hot plate, then 10 to 15 nm SiO_2 mid-layer was deposited by using an electron beam (e-beam) evaporator (Kurt J. Lesker) with a deposition rate of 0.5 Å s^{-1}. 4 wt% T-resist was prepared by diluting thermoplastic polymer (poly(benzyl methacrylate) (PBMA)) in Propylene glycol monomethyl ether acetate (PMA) as a solvent, and the small amount of BYK-310 was added as a surface additive for lowering surface tension of the resist. The prepared resist was spin-coated and post-baked 5 min at 180 ℃ forming the tri-layer structure. The T-NIL was carried out with the fabricated a-Si mold using the nanoimprinter (THU400, Zhenjiang Lehua Electronic Technology Co. Ltd.) with the temperature of 55 ℃ and pressure of 750 KPa for 15 min under vacuum. After T-NIL, the residual layer of T-resist was RIE etched by oxygen plasma (O_2 = 10 sccm, 10 mTorr, 100 W), where SiO_2 mid-layer acted as the etch-stop layer to enable extension of over etching time to remove the residual layer completely. The patterns in the T-resist were transferred to SiO_2 mid-layer by another RIE etching (CHF_3 = 25 sccm, O_2 = 1 sccm, 10 mTorr, 100 W) process. Here, a small amount of oxygen gas flow was used to minimize the etching of the top T-resist to achieve high-fidelity pattern transfer to the mid-layer. Then, the PMMA bottom layer was RIE etched by oxygen plasma (O_2 = 10 sccm, 10 mTorr, 30 W). The high etching selectivity between SiO_2 and PMMA is beneficial not only for reliable patterning in a relatively thick PMMA layer, but also for forming mushroom-like structure due to slight lateral etching of PMMA, which could be advantageous to minimize accumulation of metal on the sidewall of PMMA nano-structures during metal deposition, facilitated high-yield lift-off process and minimized

feature distortion. The sample was immersed in remover PG solution for 15 minutes at 80 °C for the lift-off process and rinsed with IPA and DI water, respectively, followed by 10 nm Cr layer deposition using the thermal evaporator. The 60 nm SiO_2 layer was etched by RIE (CHF_3 = 40 sccm, O_2 = 3 sccm, 40 mTorr, 250 W) using Cr as a hard mask, and Cr was stripped by wet etching. Finally, the 130 nm a-Si was etched using inductively coupled plasma (ICP) RIE (PlasmaTherm Apex ICP, Cl_2 = 100 sccm, Ar = 5 sccm, 10 mTorr, 250 W) using SiO_2 as a hard mask to complete a-Si metasurface fabrication.

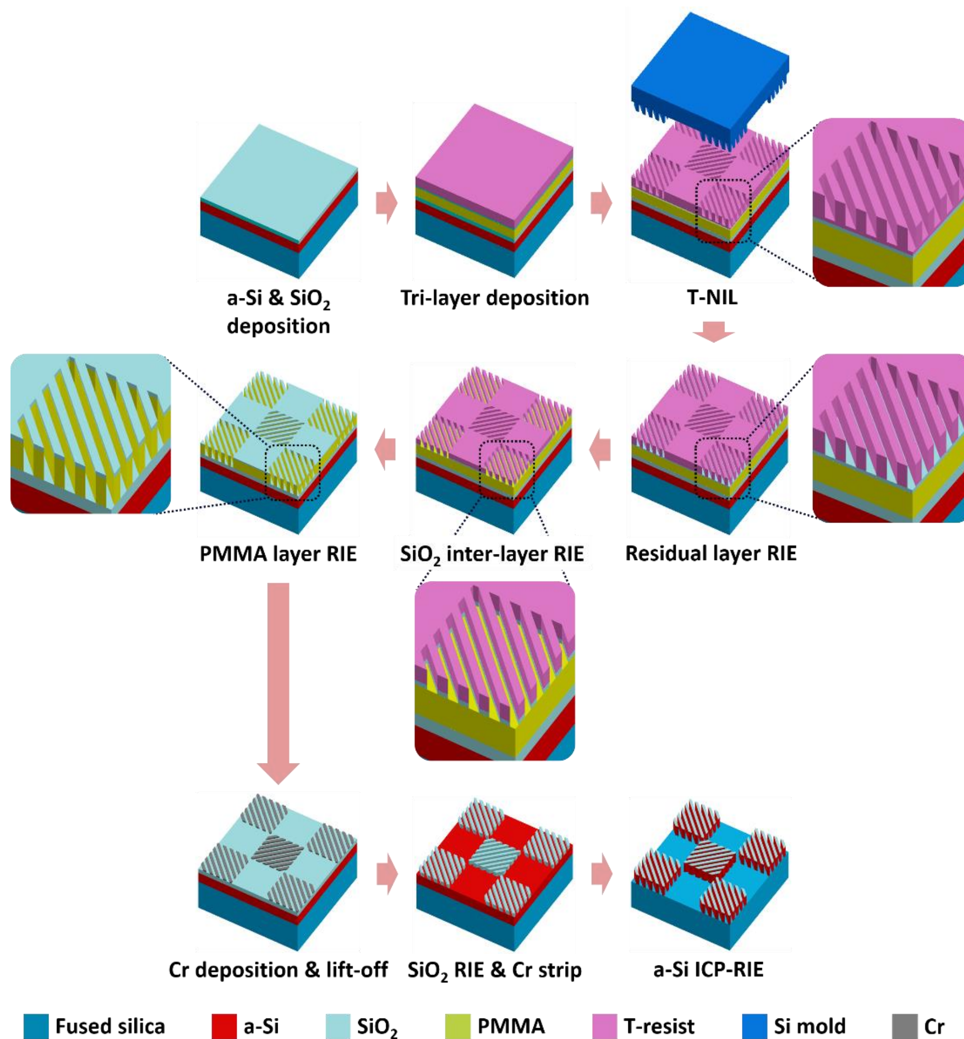

Figure 4.6: Schematic illustration of a-Si metasurface fabrication using T-NIL with tri-layer structure.

Additionally, the linewidth and corresponding duty cycle could be adjusted within a range of 20 to 30 nm by modulating the over-etching time of the T-resist residual layer using the SiO_2 inter-layer as etch stop layer. The linewidth of the metasurface would be slightly expanded during the SiO_2 hard mask and a-Si dry-etching steps, respectively, due to the undesired lateral etching, however the dominant factor to determine the dimensional parameter of the final structure was the linewidth dimension after the residual layer etching (Figure 4.7). Therefore, the developed tri-layer scheme would not only provide improved pattern transfer fidelity but also enhance the degree of freedom in metasurface fabrication by controlling dimensions as designed, which was essentially desired in metasurface fabrication.

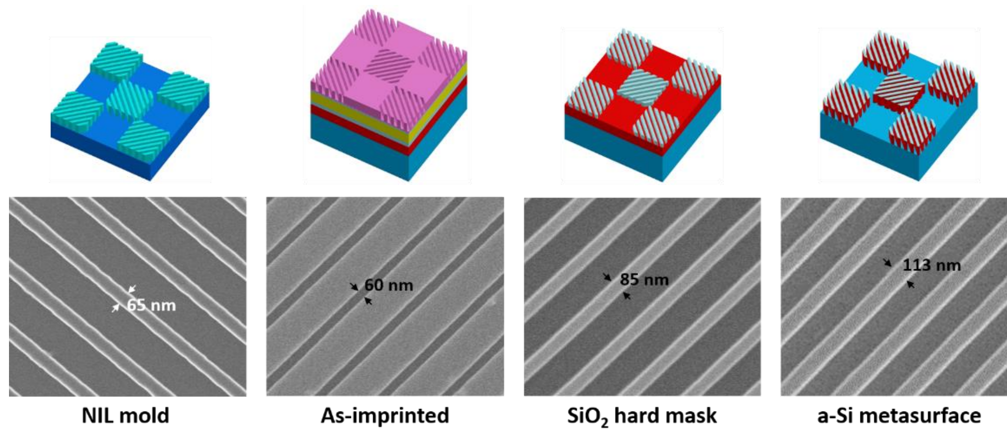

Figure 4.7: SEM images and measured linewidth for each step of the T-NIL process with the tri-layer structure for a-Si metasurface fabrication.

4.5.2 VCADGs by UV-NIL

4.5.2.1 MFD-NIL

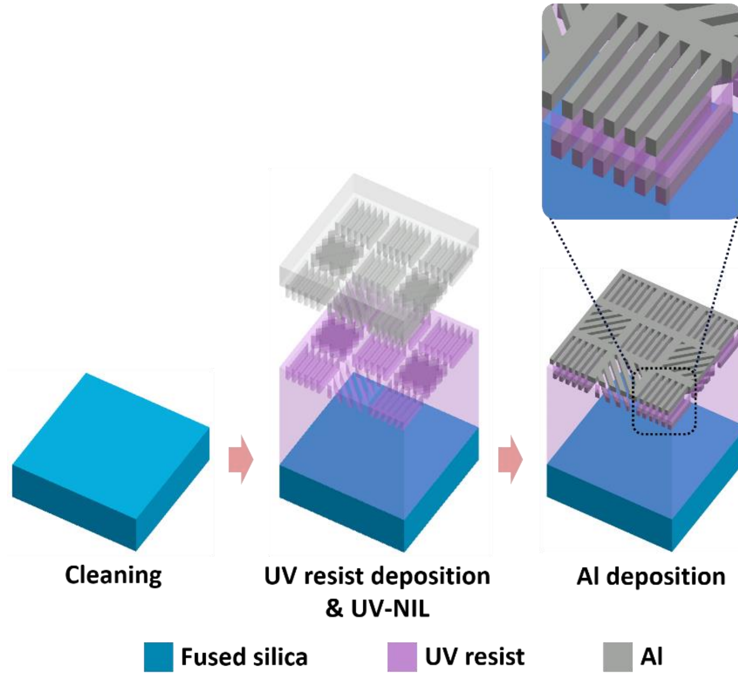

Figure 4.8: Schematic illustration of VCADG fabrication using MFD-NIL.

The VCADGs were manufactured employing a significantly simpler fabrication process (Figure 4.8). The AMOPRIME was spin-coated on the pre-cleaned fused silica substrate with an acceleration speed of 3000 rpm as an adhesion promoter and post-baked 10 min at 115 ℃ on the hot plate. The ultra-violet (UV) resist was prepared by diluting the monomer ((Acryloxypropyl)methylsiloxane homopolymer), cross-linker (Pentaerythritol tetraacrylate), surface additive (BYK-3570), and photoinitiators (Omnirad 1173 and Omnirad TPO) in Isobutyl methacrylate (IBMA), then it was spin-coated on the substrate with an acceleration speed of 4500 rpm. The MFD-NIL was preformed directly using the

fabricated transparent mold and mask aligner (MJB4, Suss MicroTec) with 1.5 s UV exposure time to cross-link the resist as SiO_x dielectric material under 100 KPa pressure. The prepared UV resist had much lower viscosity than T-resist, therefore, the resist was easily filled into the mold with relatively lower pressure [119]. Noticeably, the measured refractive index (UV-NIR spectroscopic ellipsometry, J.A. Woollam, M-2000) of cross-linked resist showed a similar refractive index as sputtered SiO_2 (Figure 4.9), therefore, the patterned resist structures during the NIL process enabled the direct replacement of SiO_2 gratings, which generally required several additional fabrication processes such as deposition, lift-off, and dry-etching, with negligible changes in optical performance.

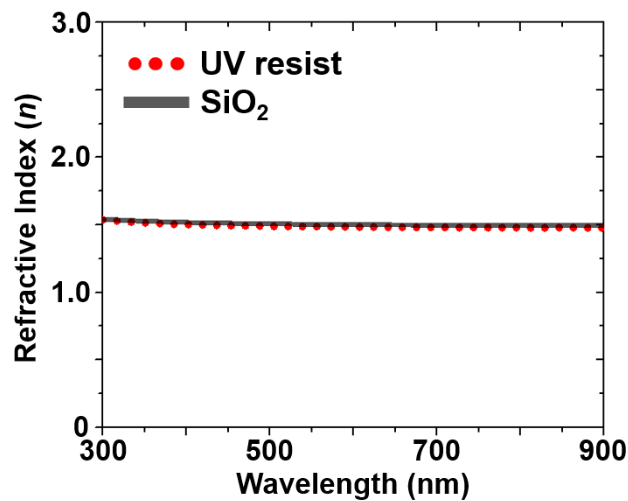

Figure 4.9: Measured refractive index of SiO_2 and UV resist using ellipsometry.

After MFD-NIL, the patterned resist surface was treated using a mild oxygen plasma process (O_2 = 10 sccm, 10 mTorr, 30 W). The UV resist consisted of organic and inorganic materials, resulting in the absence of hydroxyl groups on the surface after the NIL process [120]. Oxygen plasma generated more hydroxyl groups as oxygen atoms bonded with

dangling hydrogen bonds on the surface, which helped to create intimate contact between the cross-linked SiO_x gratings and the deposited metal to possibly minimize overhanging of metal on the top of dielectric gratings [121]. An ultra-thin layer of Cr was evaporated using an e-beam evaporator as an adhesion layer, and then Al thin film was deposited at 2.5 Å s^{-1} with the same evaporator to form the double layer gratings as followed by oxygen plasma treatment. Remarkably, the base vacuum pressure level was required to be achieved within the range of 1 to 3×10^{-7} Torr prior to Al deposition to obtain smoother surface morphology of VCADG by decreasing residual gases in the chamber because the residual gases possibly incorporated as contaminants and deteriorated the morphology of metallic thin film, which might yield degradation of optical performance [122]. The scanning electron microscopy (SEM) (Hitachi S-4700 FESEM, an acceleration voltage of 15 keV and current of 10 μA) images of VCADGs clearly indicated the effect of the base pressure on the surface morphology of deposited Al film as showing the superior surface morphology with lower base pressure (1×10^{-7} Torr) (Figure 4.10). Finally, the 200 nm SiO_2 layer was deposited as an encapsulation layer to avoid further oxidation of the Al surface by using a radio-frequency (RF) sputtering system (Kurt J. Lesker) with a deposition rate of 0.5 Å s^{-1}.

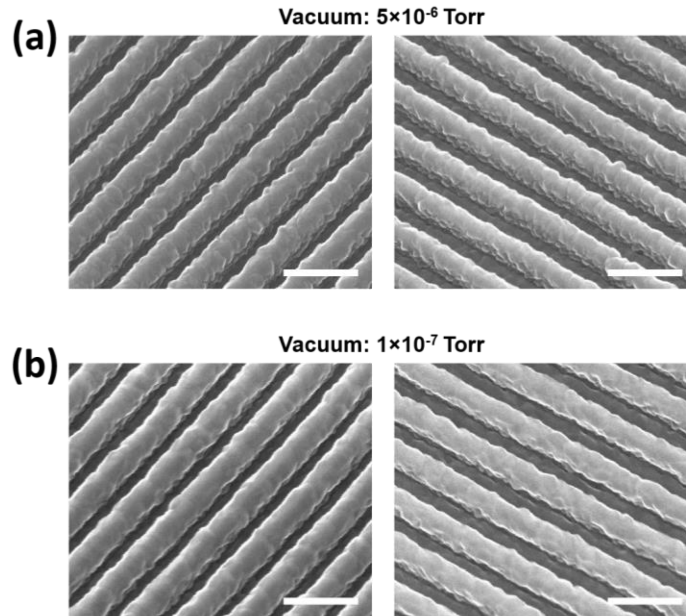

Figure 4.10: SEM images of the effect of chamber base pressure on the surface morphology of VCADGs. 80 nm Al was deposited with the base pressure of (a) 5×10^{-6} Torr and (b) 1×10^{-7} Torr, respectively. Scale bar: 300 nm.

4.5.2.2 Al Thickness Optimization

To optimize Al thickness for VCADGs, various thicknesses of Al (t_{Al}), i.e., 60 nm, 80 nm, and 100 nm, respectively, were deposited on the imprinted structures as aforementioned. UV-visible spectrometer was employed to examine the transmission efficiency and the LPER in the visible wavelength range to characterize the capability of VCADGs as LP filter in the polarimetric imaging device. Previously, it was confirmed that the vertical gap between the top and bottom Al gratings played a crucial role in accomplishing the higher efficiency and increased LPER since the excited dipoles by an electromagnetic waves along the top and bottom gratings were vertically coupled and generated a strong electric field, moreover, the coupling strength increased when the G was

smaller [106]. However, the phenomena were slightly different in the MFD-NIL based fabricated VCADG structures. The measured efficiency and LPER of t_{Al} = 80 nm (11.2 % and 36.78) were similar to t_{Al} = 100 nm (10.6 % and 36.38) at 510 nm, however, t_{Al} = 80 nm (28 % and 98.74) indicated higher efficiency and LPER than t_{Al} = 100 nm (24.5 % and 56.58) at 650 nm, while t_{Al} = 60 nm showed the lowest LPER (10.34 at 510 nm and 21.64 at 650 nm, respectively) and similar efficiency (10.73 % at 510 nm and 30.4 % at 650 nm, respectively) as t_{Al} = 80 nm along the wavelength range (Figure 4.11). Although t_{Al} = 100 nm would have a smaller gap size, i.e., estimated as 20 nm, some parts of the gap were blocked by over-hanged metal due to larger grain size, which was proportional to the thickness [123]. Therefore, t_{Al} = 80 nm was chosen to be used for actual device fabrication.

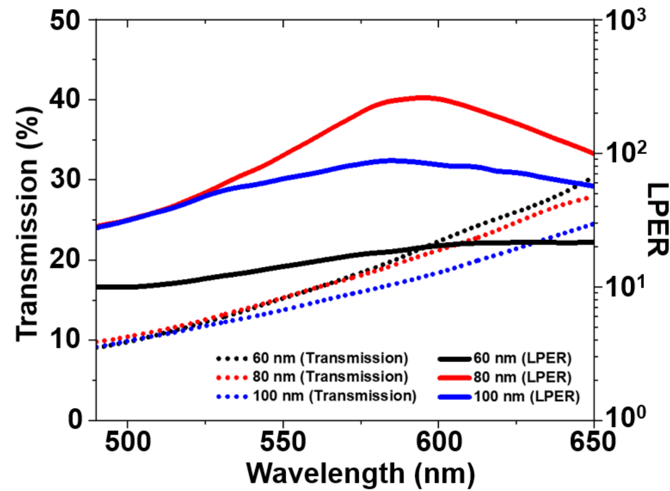

Figure 4.11: Experimentally measured transmission efficiency and calculated LPER with respect to the deposited Al thickness. 80 nm Al indicated the highest LPER (red solid line). (acknowledged *Jiawei Zuo & Nabasindhu Das* for measurements)

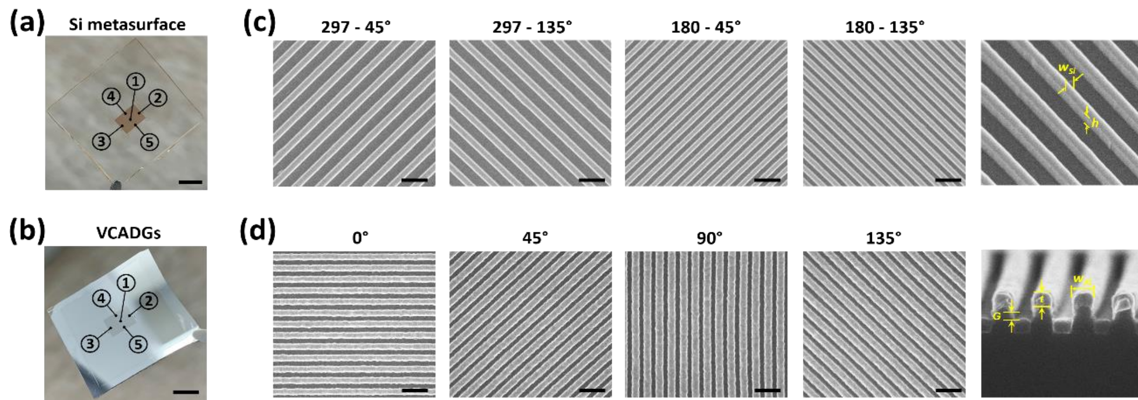

Figure 4.12: Uniformity study of the fabricated metasurface. Photographic images of fabricated (a) a-Si metasurface and (b) VCADG, indicating five different points. Scale bar: 5mm. SEM images of unit pixel arrays from (c) a-Si metasurface and (d) VCADG. Scale bar: 300 nm.

4.6 Uniformity of Fabricated Metasurfaces

The mm-scaled a-Si metasurface and VCADGs were further examined using SEM to characterize the developed NIL processes for metasurface fabrication. The SEM images of all the unit pixels of each metasurface (Figure 4.12(c) and (d)) were taken at five different points as shown in the photographic images (Figure 4.12(a) and (b)) (① $_{\text{Center}}$, ② $_{\text{Right}}$, ③ $_{\text{Left}}$, ④ $_{\text{Top}}$, and ⑤ $_{\text{Bottom}}$, respectively) to investigate the uniformity of the developed NIL process by measuring the linewidth of ten series of gratings at each point. Remarkably, the standard deviations (SDs) of all the measured linewidth of each unit pixel were maintained at less than 5 nm, implying the good uniformity of the developed process for large-scale devices (Table 4.2). Noticeably, the fabricated VCADGs showed much improved uniformity in terms of the average linewidth difference and SD (< 2 nm) because its

simplified fabrication process based on the MFD-NIL prevented any additional pattern distortion, which occurred during the other fabrication steps, such as lift-off and dry-etching. The linewidth difference between slanted gratings (116 nm for 45° and 135°, respectively) and vertical and horizontal gratings (109 nm for 90° and 0°, respectively) of VCADGs was possibly contributed by EBL based mold fabrication due to the different ways of writing patterns according to the orientation of gratings [124]. Nevertheless, these demonstrations clearly implied the feasibility of the developed NIL-based fabrication process for scalable manufacturing of polarimetric imaging sensors.

	a-Si metasurface				VCADGs			
	$W_{si_297_45°}$	$W_{si_297_135°}$	$W_{si_180_45°}$	$W_{si_180_135°}$	$W_{Al_0°}$	$W_{Al_90°}$	$W_{Al_45°}$	$W_{Al_135°}$
①Center	111.24±1.89	112.90±2.84	91.87±1.40	91.70±1.75	116.06±1.54	115.80±1.37	109.20±0.95	109.49±1.68
②Right	113.35±2.40	113.72±1.89	91.89±1.68	89.57±1.40	116.21±0.98	115.94±0.87	109.06±1.31	109.27±1.70
③Left	113.03±2.14	113.17±2.36	92.25±1.68	90.87±1.86	116.06±1.45	115.95±1.41	109.29±1.37	109.09±1.79
④Top	116.27±1.74	109.16±2.16	91.63±1.54	88.78±1.60	116.55±1.49	116.09±1.53	109.21±1.76	108.60±1.64
⑤Bottom	114.93±1.81	119.08±1.24	95.52±1.59	95.09±1.51	116.62±1.31	116.25±1.06	110.01±1.48	108.89±1.64
Total	113.73±2.57	113.61±3.82	92.63±2.11	91.08±2.70	116.30±1.33	116.01±1.30	109.35±1.38	109.07±1.65

Table 4.2 Measured linewidth dimensions from SEM images for each unit pixel at five different points for uniformity study of the developed NIL process. (Unit: nm)

4.7 Integration of Double-Layered Chiral Metasurface (DLCM)

4.7.1 Introduction – Moiré Fringe

The unit pixel size of designed structures for each metasurface was relatively small, i.e., 7.8 μm × 7.8 μm for a-Si metasurface and 4.65 μm × 4.65 μm for VCADG, respectively, therefore, the precise control of alignment was desired during the integration of two metasurfaces, especially for scalable manufacturing, since the minimal misalignment on one side would possibly yield large deviation on the whole device. In typical EBL or projection lithography-based fabrication processes, the alignment was performed by detecting alignment markers on the patterned substrate by scanning an electron beam on the markers or acquiring intensity difference from the markers, which enabled dynamic alignment with high accuracy [114, 125]. On the other hand, the alignment in contact lithography, such as the NIL process, was still challenging because the mold and substrate were required to be attached to each other to pattern the structures at once, therefore, the alignment needed to be completed prior to contacting the mold and substrate, which was static and induced potential alignment errors.

To overcome this limitation, Moiré pattern based alignment methods have been widely used in the NIL process to improve its alignment accuracy [126-129]. Two sets of micro/nano-gratings with slightly different periods were patterned on the substrate (P_1) and the mold (P_2). When the substrate and mold moved toward each other and had a very small gap between them (less than 10 μm), dark and bright periodic images were formed under

the white light illumination due to interference of two sets of gratings, which called Moiré fringe. The period of Moiré fringe (P_{fringe}) was simply calculated as

$$P_{fringe} = P_1 \cdot P_2/(P_1 - P_2) \qquad (3.1)$$

, which was significantly larger than P_1 and P_2, enabled amplified visualization of reference images during the alignment. Furthermore, the actual sample displacement (Δ) was closely related to the Moiré fringe displacement (d) as follows equation,

$$d = \Delta \cdot (P_{fringe}/P_2) \qquad (3.2)$$

where $P_{fringe}/P_2 > 1$, therefore, the alignment behavior could be monitored and adjusted in real-time by observing the movement of Moiré fringe, resulting in nanometer-scaled alignment accuracy.

4.7.2 Metasurface Alignment Using Moiré Fringe

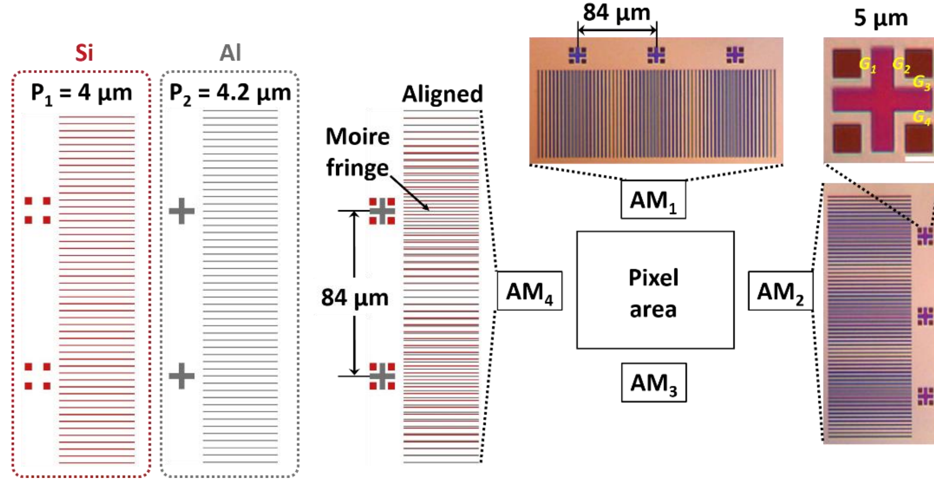

Figure 4.13: Moiré fringe based alignment technique for the integration of DLCM. Schematic illustration of design concept and microscopic images of fabricated two metasurfaces after alignment process. The magnified image indicated the aligned first (squares) and second (cross) layers (scale bar: 5µm).

Take the advantage the Moiré fringe based alignment technique was employed for the integration of two metasurfaces to manufacture the integrated DLCM (Figure 4.13). The fabricated periodic gratings through the tri-layer T-NIL process used as a-Si metasurface alignment marker ($P_1 = 4\ \mu m$), and the SiO_2 gratings on the thick transparent mold employed as VCADGs alignment marker ($P_2 = 4.2\ \mu m$). To minimize the alignment error, the total four sets of alignment markers (AM_1, AM_2, AM_3, and AM_4, respectively) were located next to the pixel area, which was 7.2 mm horizontally and 5.6 mm vertically apart from each other. The P_{fringe} was calculated as 84 µm, which enabled to monitor of three different fringes simultaneously through the screen of the mask aligner as intended due to

the limited screen field of view. Noticeably, the fringes were also observed in the layout software (Layout Editor) when two layers were overlaid, thus, small squares for a-Si metasurface and crosses for VCADGs, respectively, were added next to the minima of Moiré fringes to ease the initial alignment process. In addition, it was not required to perform any additional metal deposition on the a-Si metasurface alignment markers for improving the contrast of fringes during the alignment process [126,127], because the deposited a-Si indicated significantly different refractive index (n = 3.51 at 632 nm) from SiO_2 (n = 1.49 at 632 nm), which provided decent distinguishable contrast during the alignment process. The MFD-NIL was performed on the fabricated a-Si metasurface combined with the developed alignment process. The three Moiré fringe minima clearly appeared next to the small squares and crosses in both top (AM_1) and right (AM_2) alignment markers, respectively, as shown in the microscopic images in Figure 4.13, which indicated the appropriate alignment of two metasurfaces.

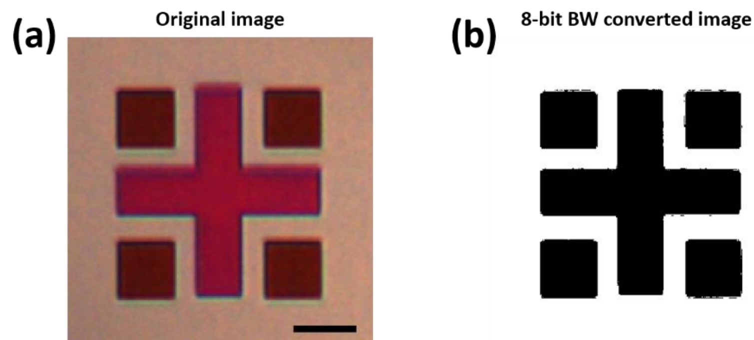

Figure 4.14: Processed microscopic images for alignment error measurement. (a) The original microscopic image. Scale bar: 5μm. (b) The converted 8-bit black and white image with the color threshold.

To further investigate the alignment accuracy, the four gaps (G_1, G_2, G_3, and G_4) between squares (a-Si metasurface) and cross (VCADGs) were measured based on the microscopy images. It was inevitable to use an optical microscope instead of SEM to take images since the secondary electron from the a-Si metasurface was not detectable due to the thick spacer layer (~ 500 nm) between the two metasurfaces. To minimize the measurement error due to the blurred edges from the microscopic images, the images were first converted to 8-bit black and white images and processed as setting the color threshold, then the dimension of gaps were measured (Figure 4.14). Remarkably, the average alignment errors were obtained below 200 nm in both x- and y-direction within the mm-scaled structure (Table 4.3), which strongly implied that the developed alignment method for NIL process would provide significantly improved alignment accuracy in the integration of multi-layered metasurfaces for scalable manufacturing, which has been a challenge to be accomplished by NIL process.

	x-direction			**y-direction**		
	G_1	G_2	**Error**	G_3	G_4	**Error**
AM_1	1.69	1.79	0.05	1.59	1.89	0.15
AM_2	1.64	1.84	0.10	1.64	1.85	0.10
AM_3	1.82	1.64	0.09	1.82	1.65	0.09
AM_4	1.86	1.62	0.12	1.93	1.55	0.19

Table 4.3 Measured gap dimensions for alignment error calculation. The error was calculated by subtracting the measured gap dimension from the median value between two gaps, e.g. $(G_1 + G_2)/2 - G_1$. (Unit: μm)

4.8 Characterizations of Integrated DLCM

Followed by Al deposition on the formed SiO_x gratings, the integration of DLCM was successfully completed. The additional 200 nm SiO_2 was deposited using a radio-frequency (RF) sputtering system (Kurt J. Lesker) on the DLCM as an encapsulation layer to avoid oxidation of Al surface and protect the structures during the sample dicing process. The photographic images of diced sample intuitively showed the integrated DLCM as indicating different metasurfaces on the front and back side of the sample (Figure 4.15(a)). The total size of the integrated DLCM was 4 mm × 5.2 mm, consisting of over 43,000 super-pixels, which demonstrated the scalability of the developed NIL process. The microscopic and SEM images of the integrated DLCM showed periodically formed super-pixels and detailed orientations and dimensional parameters of each unit pixel in one super-pixel, respectively (Figure 4.15(b)).

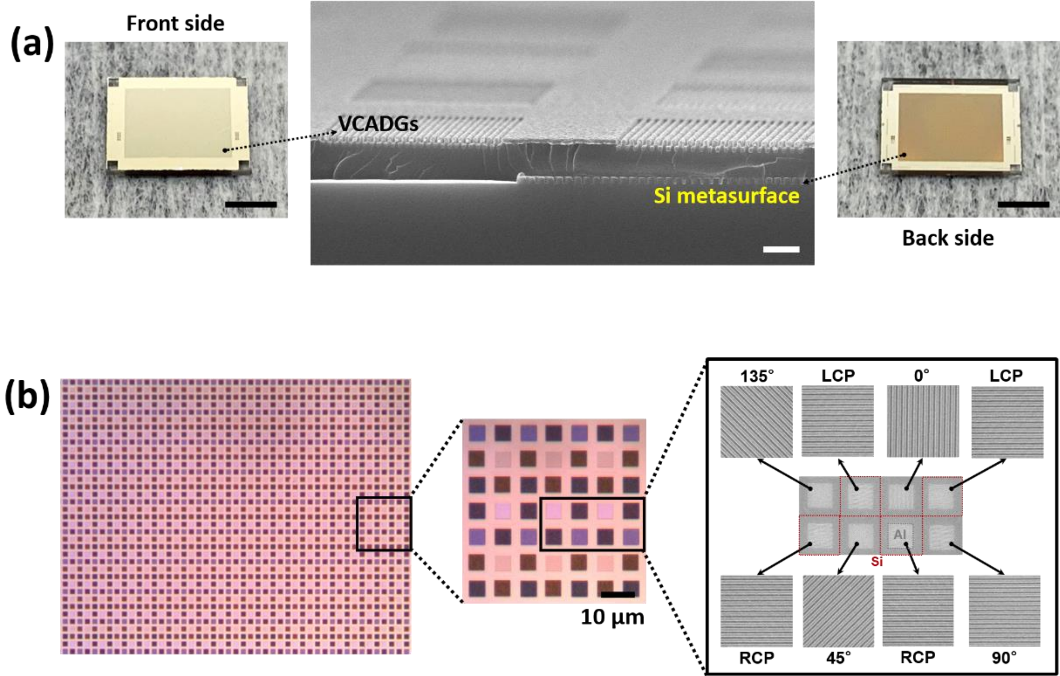

Figure 4.15: Integrated DLCM. (a) Cross-sectional SEM image (middle, scale bar: 1 μm) and photographic images (left: front & right: back, scale bar: 3 mm) of the integrated DLCM. (b) The microscopic images of the integrated DLCM with various magnifications (left: 10x and middle: 50x, scale bar: 10 μm) and SEM images of individual super-pixel (right).

Prior to bond the integrated DLCM to the CMOS sensor, the optical measurements and the finite-difference time-domain (FDTD) simulations were performed to investigate the device performance. The FDTD simulations were carried out mainly to calculate transmission efficiency and LPER and CPER of the integrated DLCM as the previous study [106]. Briefly, periodic boundary conditions ($\pm x$, $\pm y$ direction) and perfectly matched layers ($\pm z$ direction, parallel to the propagation of electromagnetic waves) were used within a unit cell along the in-plain direction. The plane wave was applied along the grating $\pm x$ and $\pm y$ direction to calculate LPER and efficiency, and the super-positioned two linearly

polarized waves were used to obtain RCP/LCP light input to calculate CPER. The over-hanged structure of the top layer of VCADGs and the tilted angle of 6° of the a-Si gratings were considered in the simulations. The mesh sizes were set to 5 nm for higher accuracy. All the spectra were examined by UV-Visible (Vis) spectrometer (Horiba iHR320 imaging spectrometer).

Noticeably, the measured LPER of the device indicated over 100 in the wavelength range from 500 nm to 700 nm, which implied its capability to be worked as a broadband linearly polarized light (LPL) detector (Figure 4.16(a)). Two peaks were observed in CPER measurements for the right-handed chiral metasurface, which were found 19 at 500 nm with the transmission efficiency of 4 % and 80 at 600 nm with the efficiency of 18 %, respectively, demonstrating the dual-wavelength operation of the fabricated polarimetric imaging system (Figure 4.16(b)). In addition, the CPER of the left-handed chiral metasurface showed similar results as the right-handed one (Figure 4.17), which proved the fabricated device would efficiently detect both right and left CPL with high accuracy. Remarkably, the measured both LPER and CPER values were significantly improved, e.g., 10 times higher CPER around 500 nm, compared to the results from the previous device which were fabricated by the conventional EBL-based process [106].

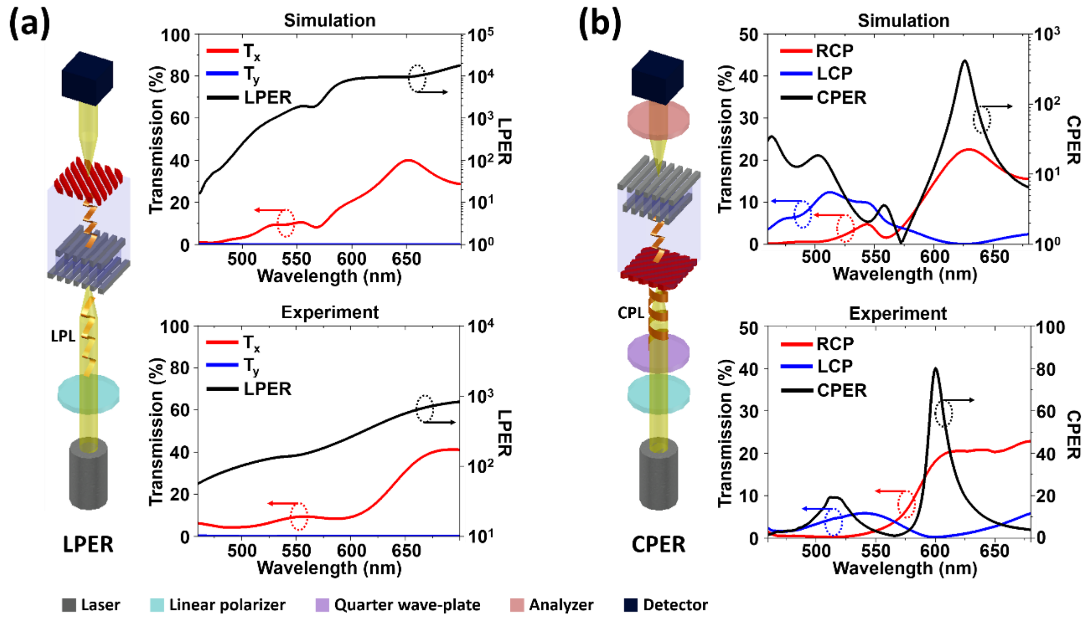

Figure 4.16: Optical performance of the integrated DLCM. Simulated and experimentally measured (a) transmission efficiency and LPER and (b) transmission efficiency and CPER for RCP detector, respectively. (acknowledged *Jiawei Zuo & Nabasindhu Das* for simulations and measurements)

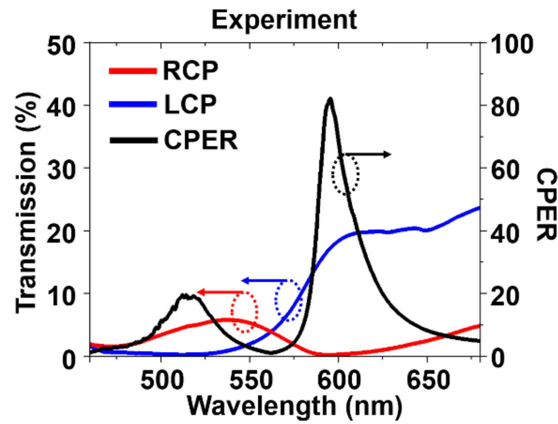

Figure 4.17: Optical performance of the integrated DLCM. Simulated and experimentally measured transmission efficiency and CPER for LCP detector. (acknowledged *Jiawei Zuo & Nabasindhu Das* for measurements)

During the SiO_2 spacing layer deposition, the modulated surface was formed between not only the chiral metasurface arrays but also the single a-Si gratings due to the non-conformal sputtering of material. As the VCADGs were fabricated on the spacing layer through the EBL, lift-off, and dry etching processes, those structures formed a large amount of leaky paths of the incident light between the surface of the modulated spacing layer and underneath the VCADG structures, which adversely degraded their optical performance. On the other hand, the developed MFD-NIL provided planarized surface as well as the spacing layer for the VCADGs, which prevented forming of leakage paths, therefore, the highly improved optical performance was achieved. This phenomenon was strongly supported by SEM images of each integrated device, where the integrated DLCM by the developed NIL showed smoothly integrated metasurface (Figure 4.18(a)), while the integrated one by EBL-based process indicated significant possible leaky paths (Figure 4.18(b) [106]).

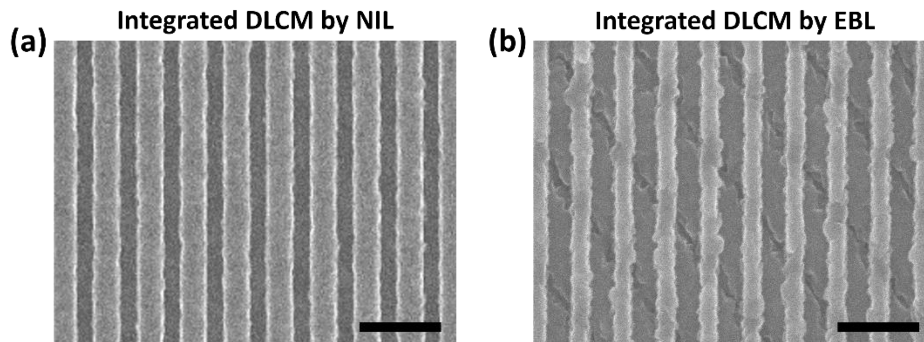

Figure 4.18: SEM images of the integrated DLCM (a) by the developed NIL process and (b) by the EBL-based conventional process [106]. Scale bar: 300 nm.

Despite small discrepancies possibly attributed to differences in structural geometries and material properties between experiments and simulations, the experimental results were well consistent with the simulation results (Figure 4.16). Noticeably, the integrated DLCM indicated relatively lower efficiency in both simulation and measurement. The major contribution of this phenomenon was due to less anisotropic etching during the NIL mold fabrication for VCADGs. During the RIE etching process, the substrate material, i.e., thick fused silica, was etched without an etch stop layer, thus it induced rounded edges rather than sharp edges due to a slight different etch rate at the center and edges of patterns [130]. As a consequence, the rounded edges were obtained in the imprinted SiO_x gratings (Figure 4.19(a)), resulted in the over-hanged structures after Al deposition process (Figure 4.19(b)), which degraded the efficiency as metal blocked partial gaps between top and bottom Al gratings due to varied grain size. The efficiency can be further improved by modifying the etching recipe during the mold fabrication in future study. Nonetheless, these demonstrations strongly addressed that the developed NIL process would not only significantly reduce fabrication processing time and cost in scalable manufacturing, but also greatly improve device performance in polarimetric imaging.

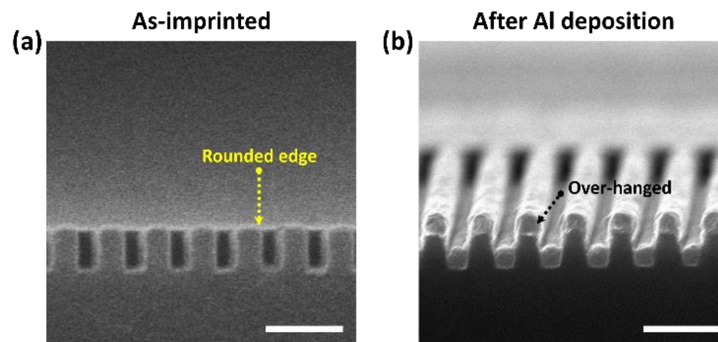

Figure 4.19: SEM images of the VCADGs. (a) As-imprinted and (b) after Al deposition. Scale bar: 300 nm.

4.9 Summary

In summary, the scalable manufacturing process for polarimetric CMOS imaging system has been successfully demonstrated using the NIL process. The developed tri-layer structure for T-NIL facilitated the lift-off process to increase yield potentially and enhance the degree of freedom in fabrication by providing the capability of adjustable linewidth dimension. Both fabricated a-Si metasurface and VCADG structures also indicated good pattern transferability and uniformity in terms of linewidth dimension over mm-scale. Due to the layer-by-layer nature of the NIL process, the developed NIL process proved to have higher throughput than EBL-based fabrication. The Moiré fringe based alignment technique enabled the alignment accuracy of two metasurfaces less than 200 nm in both x- and y-direction, which was found to be sufficient for the integration of DLCM. Importantly, the significantly improved device performance, i.e., LPER and CPER, was observed compared to the previous EBL fabricated device due to the planarized surface of VCADG structures with the advantage of MFD-NIL process, which prevented a large amount of leakage paths underneath the structures. This demonstration strongly implied that the newly developed NIL-based metasurface integration technology is opening new paths to have broad use in optical application fields such as metalens, augmented reality, and holographic with high throughput and low cost.

CHAPTER 5

CONCLUSION

This dissertation has elucidated the details of the development process of various patterning technologies for accessible, cost-effective, scalable manufacturing, especially in the potential advanced optical applications.

The developed polymer-assisted photochemical deposition (PPD) based structural color printing (SCP) has opened a new approach to generating micro-scaled structural colors. Unlike other micro/nano-lithography technologies, PPD can pattern micro-scaled metallic structures directly on the substrate by ultra-violet (UV) illumination even in ambient and room-temperature conditions, which can eliminate complex requirements for conventional lithography processes and broaden a range of applicable substrates. PPD-based SCP has been demonstrated by printing ultra-thin films on the simple Fabry-Pérot cavity and exhibited vivid color by providing large modulation of reflectance with the advantage of the lossy characteristic of PPD film (Chapter 1).

The metallic nano-apertures have attracted tremendous attention in various potential optical applications due to their geometrical advantages, however, a complicated fabrication process has limited their usage. The developed germanium (Ge) assisted transfer printing (GTP) has demonstrated a new path of scalable and cost-effective fabrication of nano-scaled metallic aperture structures. With the advantage of an ultra-thin Ge nucleation layer, the nano-apertures have not only minimized their structural distortion

but also retained smoother surface morphology. The versatility of GTP regarding materials and structural geometries has been demonstrated by transferring noble metallic nano-gratings and nano-apertures, i.e., silver (Ag) and gold (Au), with sub-100 nm resolution up to 50 nm thickness (Chapter 2).

Nanoimprint lithography (NIL) has been successfully utilized to develop a scalable manufacturing processes for polarimetric CMOS imaging system. NIL is capable of patterning nanometer-scaled structures over mm-scale within a minute, enabling high throughput with high resolution, which is suitable for cost-effective and scalable manufacturing. The developed NIL process has demonstrated its capability of fabricating both a-Si metasurface and vertically coupled aluminum double-layered gratings (VCADGs) with superior pattern transferability and uniformity. The two structures have been successfully integrated to form the double-layered chiral metasurface for full-stokes polarimetric imaging operation employing the developed multi-functional-direct (MFD) NIL and Moiré fringe based alignment method. The developed NIL process has significantly improved device performance as supplementing drawbacks from the electron beam lithography (EBL) based process (Chapter 3).

Although the developed patterning technologies have been limited in optical applications in this dissertation, they can be enlarged to other related applications. To mention examples, PPD can be used to fabricate highly transparent ultra-thin conductive metallic film for electronic applications, GTP can be accommodated to transfer various structures such as nano-ribbons for bio-molecular sensing applications, and NIL based two

layers integration can potentially be employed in the manufacturing of integrated circuits (ICs). These demonstrated economic and versatile advanced patterning technologies would be expected to fruitful the degree of freedom in product manufacturing of various applications.

REFERENCES

[59] Carlson, A., Bowen, A. M., Huang, Y., Nuzzo, R. G. & Rogers, J. A. Transfer printing techniques for materials assembly and micro/nanodevice fabrication. Advanced Materials, **24**(39), 5284-5318 (2012).

[60] Loo, Y. L., Lang, D. V., Rogers, J. A. & Hsu, J. W. P. Electrical contacts to molecular layers by nanotransfer printing. Nano Letters, **3**(7), 913-917 (2003).

[61] Yao, J. J. RF MEMS from a device perspective. Journal of Micromechanics and Microengineering, **10**, R9-R38 (2000).

[62] Prinz, V. Y., Seleznev, V. A., Prinz, A. V. & Kopylov, A. V. 3D heterostructures and systems for novel MEMS/NEMS. Science and Technology of Advanced Materials, **10**, 034502 (2009).

[63] Judy, J. W. Microelectromechanical systems (MEMS): fabrication, design and applications. Smart Materials and Structures, **10**(6), 115-1134 (2001).

[64] Sirkar, K., Revzin, A. & Pishko, M. V. Glucose and lactate biosensors based on redox polymer/oxidoreductase nanocomposite thin films. Analytical Chemistry, **72**(13), 2930-2936 (2000).

[65] Wells, M. & Crooks, R. M. Interactions between organized, surface-confined monolayers and vapor-phase probe molecules. Journal of American Chemical Society, **118**, 3988-3989 (1996).

[66] Park, J. S., Kim, T. W., Stryakhilev, D., Lee, J. S., An, S. G., Pyo, Y. S., Lee, D. B., Mo, Y. G., Jin, D. U. & Chung, H. K. Flexible full color organic lifht-emitting diode display on polyimide plastic substrate driven by amorphous indium gallium zinc oxide thin-film transistors. Applied Physics Letters, **95**(1), 013503 (2009).

[67] Striakhilev, D., Nathan, A., Vygranenko, Y., Servati, P., Lee, C. H. & Sazonov, A. Amorphous silicon display backplanes on plastic substrates. Journal of Display Technology, **2**(4), 364-371 (2006).

[68] Li, Y., Qian, F., Xiang, J. & Leiber, C. M. Nanowire electronic and optoelectronic devices. Materials Today, **9**(10), 18-27 (2006).

[69] Chen, Z., Cotterell, B., Wang, W., Guenther, E. & Chua, S. J. A mechanical assessment of flexible optoelectronic devices. Thin Solid Films, **394**(1-2), 202-206 (2001).

[70] Kim, S., Lee, W. S., Lee, J. & Park, I. Direct micro/nano metal patterning based on two-step transfer printing of ionic metal nano-ink. Nanotechnology, **23**(28), 285301 (2012).

[71] Kim, J. W., Yang, K. Y., Hong, S. H. & Lee, H. Formation of Au nano-patterns on various substrates using simplified nano-transfer printing method. Applied Surface Science, **254**(17), 5607-5611 (2008).

[72] Nagel, R. D., Haeberle, T., Schmidt, M., Lugil, P. & Scarpa, G. Large area nano-transfer printing of sub-50-nm metal nanostructures using low-cost semi-flexible hybrid templates. Nano Express, **11**, 143 (2016).

[73] Wang, Z., Yuan, J., Zhang, J., Xing, R., Yan, D. & Han, Y. Metal transfer printing and its application in organic field-effect transistor fabrication. Advanced Materials, **15**(12), 1009-1012 (2003).

[74] Chen, Y., Shu, Z., Feng, Z., Kong, L., Liu, Y. & Duan, H. Reliable patterning, transfer printing and post-assembly of multiscale adhesion-free metallic structures for nanogap device applications. Advanced Functional Materials, **30**(32), 2002549 (2020).

[75] Genet, C. & Ebbesen, T. W. Light in tiny holes. Nature, **445**, 39-46 (2007).

[76] Novotny, L. & Hulst, N. V. Antennas for light. Nature Photonics, **5**, 83-90 (2011).

[77] Wang, L, Jin, E. X., Uppuluri, S. M. & Xu, X. Contact optical nanolithography using nanoscale C-shaped apertures. Optics Express, **14**(21), 9902-9908 (2006).

[78] Wen, X., Datta, A., Traverso, L. M., Pan, L., Xu, X. & Moon, E. E. High throughput optical lithography by scanning a massive array of bowtie aperture antennas at near-field. Scientific Report, **5**, 16192 (2015).

[79] Han, K., Xu, W., Ruiz, A., Ruchhoeft, P. & Chellam, S. Fabrication and characterization of polymeric microfiltration membranes using aperture array lithography. Journal of Membrane Science, **249**(1-2), 193-206 (2005).

[80] Choy, J. T., Hausmann, B. J. M., Babinec, T. M., Bulu, I., Khan, M., Maletinsky, P., Yacoby, A. & Loncar, M. Enhanced single-photon emission from a diamond-silver aperture. Nature Photonics, **5**, 738-743 (2011).

[81] Korneeva, Y. P., Vodolazov, D. Y., Semenov, Floya, I. N., Simonov, N., Baeva, E., Korneev, A. A., Goltsman, G. N. & Klapwijk, T. M. Optical single-photon detection in micrometer-scale NbN bridges. Physical Review Applied, **9**, 064037 (2018).

[82] Peng, C., Jin, E. X., Clinton, T. W. & Seigler, M. A. Cutoff wavelength of ridge waveguide near field transducer for disk data storage. Optics Express, **16**(20), 16403-16051 (2008).

[83] Chen, W., Thoreson, M. D., Ishii, S., Kildishev, A. V. & Shalaev, V. M. Ultra-thin ultra-smooth and low-loss silver films on a germanium wetting layer. Optics Express, **18**(5), 5124-5134 (2010).

[84] Jeong, E., Zhao, G., Yu, S. M., Lee, S. G., Bae, J. S., Park, J., Rha, J., Lee, G. H. & Yun, J. Minimizing optical loss in ultrathin Ag films based on Ge wetting layer: Insights on Ge-mediated Ag growth. Applied Surface Science, **528**, 146989 (2020).

[85] Ciesielski, A., Skowronski, L., Trzcinski, M. & Szoplik, T. Controlling the optical parameters of self-assembled silver films with wetting layers and annealing. Applied Surface Science, **421**(B), 349-356 (2017).

[86] Sanghera, J. S., Busse, L. E. & Aggarwal, I. D. Effect of scattering centers on the optical loss of As_2S_3 glass fibers in the infrared. Journal of Applied Physics, **75**(10), 4885-4891 (1994).

[87] Schaper, C. D. Water-soluble polymer templates for high-resolution pattern formation and materials transfer printing. Journal of Microlithography Microfabrication and Microsystems, **3**(1), 174-185 (2004).

[88] Schaper, C. D. & Miahnahri, A. Polyvinyl alcohol templates for low cost, high resolution, complex printing. Journal of Vacuum Science & Technology B, **22**, 3323-3326 (2004).

[89] Gurarslan, A., Yu, Y., Su, L., Yu, Y., Suarez, F., Yao, S., Zhu, Y., Ozturk, M., Zhang, Y. & Cao, L. Surface-energy-assisted perfect transfer of centimeter-scale monolayer and few-layer MoS_2 films onto arbitrary substrates. ACS Nano, **8**(11), 11522-11528 (2014).

[90] Huang, X., Hansen, N. & Tsuji, N. Hardening by annealing and softening by deformation in nanostructured metals. Science, **312** (5771), 249-251 (2006).

[91] Chen, C. H., Yu, T. H., Lee, Y. C. & Hsiao, F. B. Infrared-assisted and roller-based direct metal contact transfer technology for flexible polarizer. Proceedings of 5th IEEE International Conference on Nano/Micro Engineered and Molecular Systems, Xiamen, China, 20-23 January (2010).

[92] Dubovik, O., Li, Z., Mishchenko, M. I., Tanre, D., Karol, Y., Bojkov, B., Cairns, B., Diner, D. J., Espinosa, W. R., Goloub, P., Gu, X., Hasekamp, O., Hong, J., Hou, W., Knobelspiesse, K. D., Landgraf, J., Li, L., Litvinov, P. & Yin, D. Polarimetric remote sensing of atmospheric aerosols: Instruments, methodologies, results, and perspectives. Journal of Quantitative Spectroscopy and Radiative Transfer, **224**, 474-511 (2019).

[93] Chen, W., Bai, S., Wang, D., Zhao, H., Sun, H. & Yi, L. Aerosol-induced changes in sky polarization pattern: potential hint on applications in polarimetric remote sensing. International Journal of Remote Sensing, **41**(13), 4963-4980 (2019).

[94] Huang, B., Liu, T., Han, J. & Hu, H. Polarimetric target detection under uneven illumination. Optics Express **23**(18), 23603-23612 (2015).

[95] Vannier, N., Goudail, F., Plassart, C., Boffety, M., Feneyrou, P., Leviandier, L., Galland, F. & Bertaux, N. Comparison of different active polarimetric imaging modes for target detection in outdoor environment. Applied Optics, **55**(11), 2881-2891 (2016).

[96] Tang, F., Gui, L., Liu, J., Chen, K., Lang, L. & Cheng, Y. Metal target detection method using passive millimeter-wave polarimetric imagery. Optics Express **28**(9), 13336-13351 (2020).

[97] Hu, H., Zhao, L., Huang, B., Li, X., Wang, H. & Liu, T. Enhancing visibility of polarimetric underwater image by transmittance correction. IEEE Photonics Journal, **9**(3), 6802310 (2017).

[98] Yang, L., Liang, J., Zhang, W., Ju, H., Ren, L. & Shao, X. Underwater polarimetric imaging for visibility enhancement utilizing active unpolarized illumination. Optcs Communications, **438**, 96-101 (2019).

[99] Ney, M. & Abdulhalim, I. Ultrahigh polarimetric image contrast enhancement for skin cancer diagnosis using InN plasmonic nanoparticles in the terahertz range. Journal of Biomedical Optics, **20**(12), 125007 (2015).

[100] Safrani, A., Aharon, O., Mor, S., Arnon, O., Rosenberg, L. & Abdulhalim II, I. S. Skin biomedical optical imaging system using dual-wavelength polarimetric control with liquid crystals. Journal of Biomedical Optics, **15**(2), 026024 (2010).

[101] Le, D. L., Nguyen, D. T., Le, T. H., Phan, Q. H., & Pham, T. T. H. Characterization of healthy and cancerous human skin utilizing stokes-mueller polarimetry technique. Optics Communications, **480**, 126460 (2021).

[102] Huber, D. F., Denes, L. J., Hebert, M., Gottlieb, M. S., Kaminsky, B. & Metes, P. A Spectro-polarimetric imager for intelligent transportation systems. Proceedings of SPIE – International Society for Optical Engineering, **3207** (1998).

[103] Dong, J. F., Zhou, J., Koschny, T. & Soukoulis, C. Bi-layer cross structure with strong optical activity and negative refractive index. Opics Express, **17**(16), 14172-14179 (2009).

[104] Zhu, A. Y., Chen, W. T., Zaidi, A., Huang, Y. W., Khorasaninejad, M., Sanjeev, V., Qiu, C. W. & Capasso, F. Giant intrinsic chiro-optical activity in planar dielectric nanostructures. Light: Science & Applications, **7**, 17158 (2018).

[105] Basiri, A., Chen, X., Bai, J., Amrollahi, P., Carpenter, J., Holman, Z., Wang, C. & Yao, Y. Nature-inspired chiral metasurfaces for circular polarization detection and full-stokes polarimetric measurements. Light: Science & Applications, **8**, 78 (2019).

[106] Zuo, J., Bai, J., Choi, S., Chen, X., Wang, C. & Yao, Y. Chip-integrated full-stokes polarimetric imaging sensor, Conference on Lasers and Electro-Optics (CLEO): Science and Innovations, San Jose, US, 15-20 May (2022).

[107] Chou, S. Y., Krauss, P. R. & Renstrom, P. J. Nanoimprint lithography. Journal of Vacuum Science & Technology B: Microelectronics and Nanometer Structures Processing, Measurement, and Phenomena, **14**, 4124 (1996).

[108] Lee, G. Y., Hong, J. Y., Hwang, S. H., Moon, S., Kang, H., Jeon, S., Kim, H., Jeong, J. H. & Lee, B. Metasurface eyepiece for augmented reality. Nature Communications, **9**, 4562 (2018).

[109] Pina-Hernandez, C., Koshelev, A., Dhuey, S., Sassolini, S., Sainato, M., Cabrini, S. & Munechika, K. Nanoimprinted high-refractive index active photonic nanostructures based on quantum dots for visible light. Scientific Reports, **7**, 17645 (2017).

[110] Yoon, G. Kim, K, Huh, D., Lee, H. & Rho, J. Single-step manufacturing of hierarchical dielectric metalens in the visible. Nature Communications, **11**, 2268 (2020).

[111] Joo, W. J., Kyung, J., Esfandyarpour, M., Lee, S. H., Song, S., Kwon, Y. N., Song, S. H., Bae, J. C. & Brongersma, M. L. Metasurface-driven OLED displays beyond 10000 pixels per inch. Science, **370**(6515), 459-463 (2020).

[112] Oh, D. K., Lee, T., Ko, B., Badloe, T., Ok, J. G. & Rho, J. Nanoimprint lithography for high-throughput fabrication of metasurfaces. Frontiers of Optoelectronics, **14**, 229-251 (2021).

[113] Guo, L. Nanoimprint lithography: methods and material requirements. Advanced Materials, **19**(4), 495-513 (2007).

[114] Gschrey, M., Schmidit, R., Schulze, J. H., Strittmatter, A., Rodt, S. & Reitzenstein, S. Resolution and alignment accuracy of low-temperature in situ electron beam lithography for nanophotonic device fabrication. Journal of Vacuum Science & Technology B, **33**(2), 021603 (2015).

[115] Jung, G. Y., Li, Z., Wu, W., Chen, Y., Olynick, D. L., Wang, S. Y., Tong, W. M. & Williams, R. S. Vapor-phase self-assembled monolayer for improved mold release in nanoimprint lithography. Langmuir, **21**(4), 1158-1161 (2005).

[116] Lebib, A., Chen, Y., Carcenac, F., Cambril, E., Manin, L., Couraud, L. & Launois, H. Tri-layer systems for nanoimprint lithography with an improved process latitude. Microelectronic Engineering, **53**(1-4), 175-178 (2000).

[117] Morton, K. J., Nieberg, G., Bai, S. & Chou, S. Y. Wafer-scale patterning of sub-40 nm diameter and high aspect ratio (>50:1) silicon pillar arrays by nanoimprint and etching. Nanotechnology, **19**(34), 345301 (2008).

[118] Hu, W., Zhang, M., Wilson, R. J., Koh, A. L., Wi, J. S., Tang, M., Sinclair, R. & Wang, S. X. Fabrication of planar, layered nanoparticles using tri-layer resist templates. Nanotechnology, **22**(18), 185302 (2011).

[119] Austin, M. D., Ge, H., Wu, W., Li, M., Yu, Z., Wasserman, D., Lyon, S. A. & Chou, S. Y. Fabrication of 5 nm linewidth and 14 nm pitch features by nanoimprint lithography. Applied Physics Letters, **84**(26), 5299 (2004).

[120] Li, M., Chen, Y., Luo, W. & Cheng, X. Demolding force dependence on mold surface modifications in UV nanoimprint lithography. Microelectronic Engineering, **236**, 111470 (2021).

[121] Faber, H., Hirschmann, J., Klaumunzer, M., Braunschweig, B., Peukert, W. & Halik, M. Impact of oxygen plasma treatment on the device performance of zinc oxide nanoparticle-based thin-film transistors. Applied Materials & Interfaces, **4**(3), 1693-1696 (2012).

[122] Englich, C. D., Shine, G., Dorgan, V. E., Saraswat, K. C. & Pop, E. Improved contacts to MoS_2 transistors by ultra-high vacuum metal deposition. Nano Letters, **16**(6), 3824-3830 (2016).

[123] Dulmaa, A., Cougnon, F. G., Dedoncker, R. & Depla, D. On the grain size-thickness correlation for thin films. Acta Materialia, **212**, 116896 (2021).

[124] Groves, T. R., Pickard, D., Rafferty, B., Crosland, N., Adam, D. & Schubert, G. Maskless electron beam lithography: prospects, progress, and challenges. Microelectronic Engineering, **61-62**, 285-293 (2002).

[125] Chen, W., Yan, W., Hu, S., Yang, Y. & Zhou, S. Extended dual-grating alignment method for optical projection lithography. Applied Optics, **49**(4), 708-713 (2010).

[126] Muhlberger, M., Bergmair, I., Schwinger, W., Gmainer, M., Schofner, R., Glinsner, T., Hasenfub, Ch., Hingerl, K., Vogler, M., Schmidt, H. & Kley, E. B. A Moiré method for high accuracy alignment in nanoimprint lithography. Microelectronic Engineering, **84**(5-8), 925-927 (2007).

[127] Li, N., Wu, W. & Chou, S. Y. Sub-20-nm alignment in nanoimprint lithography using Moiré fringe. Nano Letters, **6**(11), 2626-2629 (2006).

[128] Shao, J., Ding, Y., Tian, H., Li, X., Li, X. & Liu, H. Digital Moiré fringe measurement method for alignment in imprint lithography. Optics & Laser Technology, **44**(2), 446-451 (2012).

[129] Wang, N., Jiang, W. & Zhang, Y. Misalignment measurement with dual-frequency Moiré fringe in nanoimprint lithography. Optics Express **28**(5), 6755-6765 (2020).

[130] Ray, T., Zhu, H. & Meldrum, D. R. Deep reactive ion etching of fused silica using a single-coated soft mask layer for bio-analytical applications. Journal of Micromechanics and Microengineering, **20**, 097002 (2010).

APPENDIX A

SUPPLEMENTARY FIGURES FOR CHAPTER 2

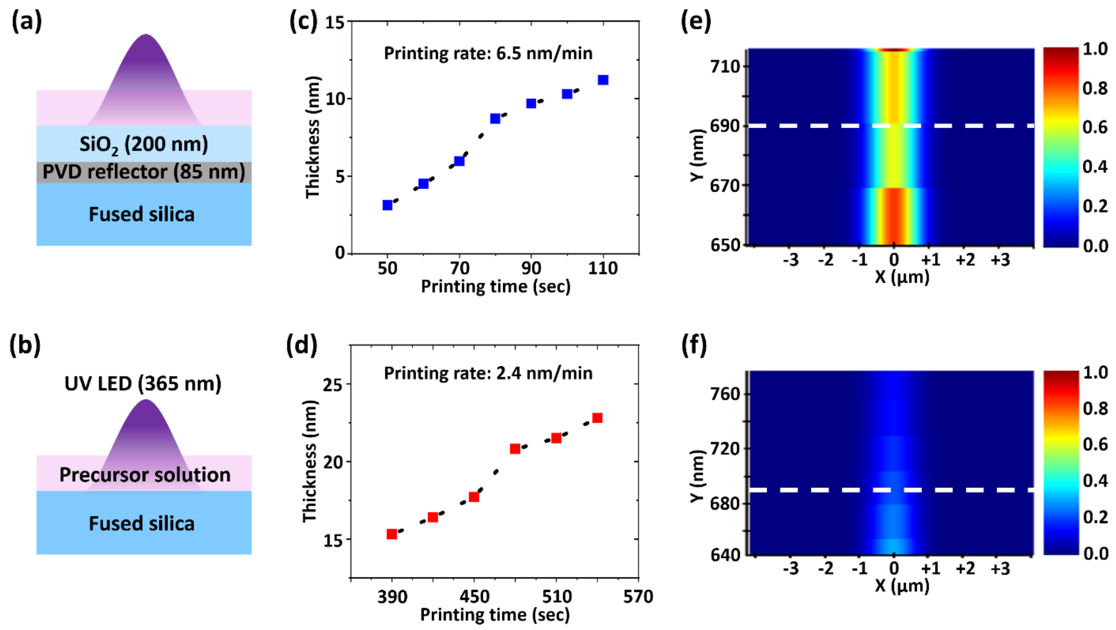

Figure A.1: Structure dependent printing behavior. Schematic cross-section view of printing substrate structures (a) with the SiO_2/PVD Ag reflector and (b) without the reflector. (c and d) Printed PPD film thickness as a function of printing time corresponding to (a) and (b), respectively. (e and f) FDTD simulated the electromagnetic field intensity distribution in corresponding to (a) and (b), respectively. White dashed line indicates the printing surface.

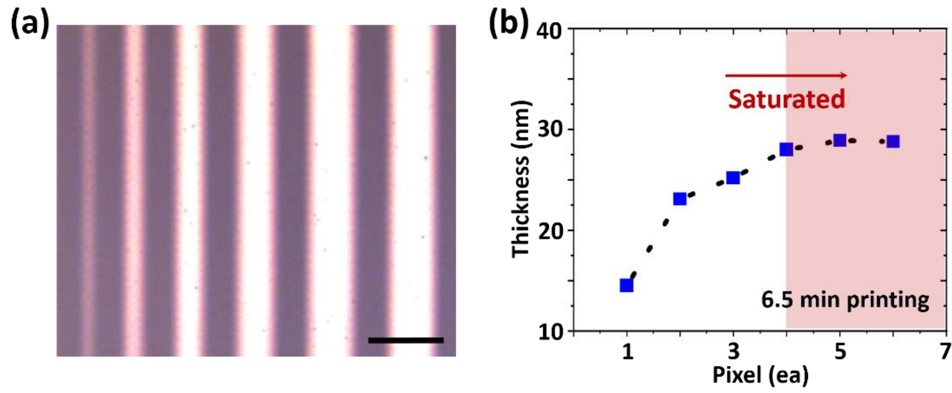

Figure A.2: Characterization of the printed PPD film. (a) Pixel-dependent PPD printing on the fused silica substrate. Scale bar: 50 μm. (b) Printed PPD film thickness as a function of pixel size extracted from (a). PPD film thickness saturated after 4 pixel.

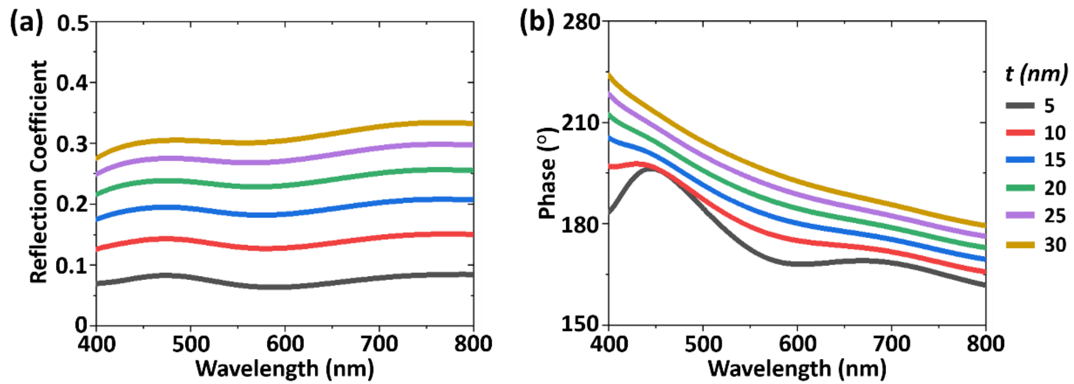

Figure A.3: FDTD simulation of the printed PPD film. Thickness-dependent (*t*) (a) reflection coefficient of PPD film and (b) phase shift accumulated at the PPD and fused silica interface.

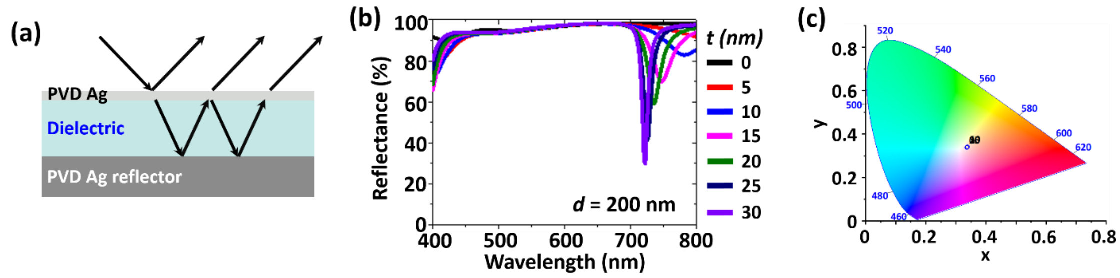

Figure A.4: FDTD simulated reflectance spectra for structural colors. (a) Basic configuration of an interference effect in the FP cavity. (b) Reflectance spectra according to the top PVD film thickness with fixed dielectric thickness (200 nm). (c) 1931 CIE color coordinates corresponding to (b).

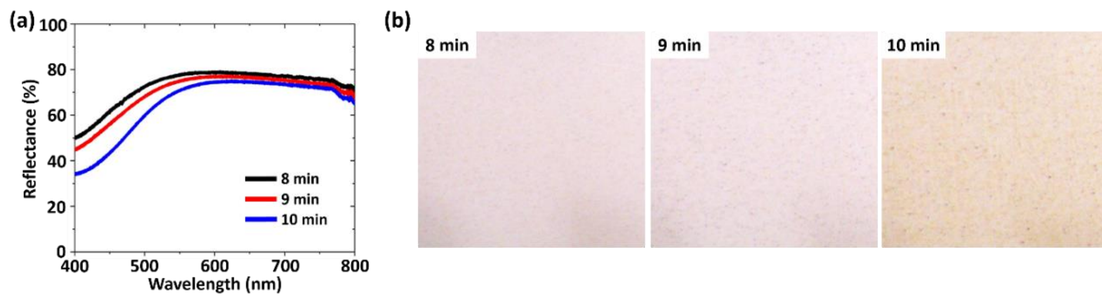

Figure A.5: Characterization of the PPD reflector. (a) Measured relative reflectance of the thick PPD Ag films prepared on fused silica substrate with various printing time. (b) Optical images of the time-dependent printed PPD films.

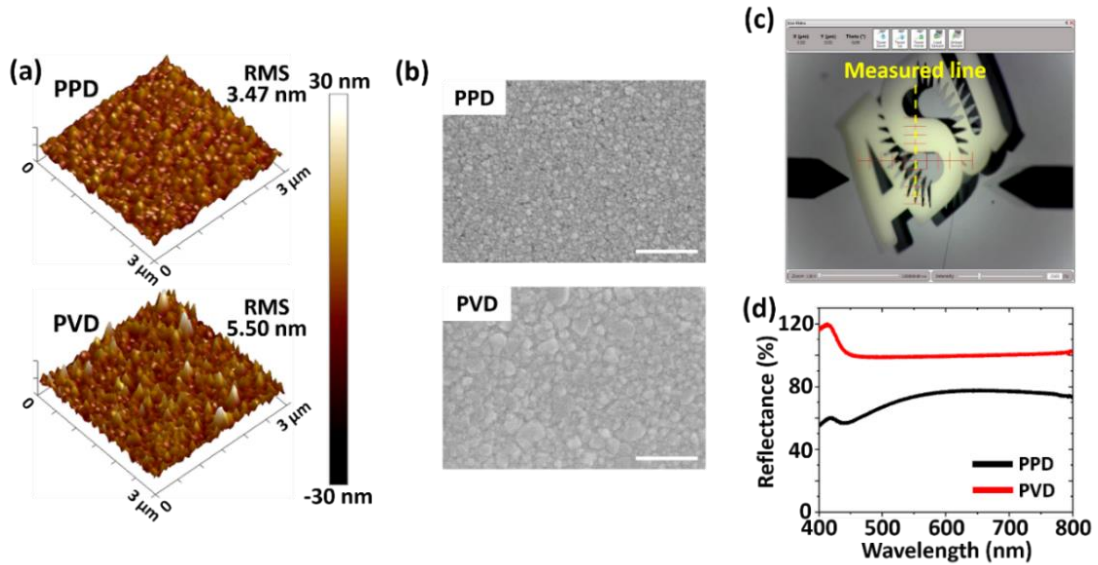

Figure A.6: Characterization of the PPD back reflector. (a) 3D profile of AFM images and (b) SEM images (scale bar: 500 nm) of the 85 nm Ag films prepared on fused silica substrate by PPD and PVD, respectively. (c) Optical image of the 85 nm printed ASU logo under surface profiler. (d) Measured relative reflectance of the 85 nm Ag films prepared on fused silica substrate by PPD and PVD, respectively.

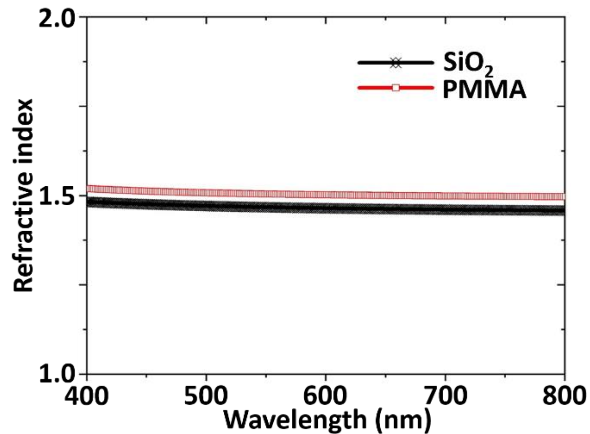

Figure A.7: Measured refractive index of SiO_2 and PMMA by using UV-NIR spectroscopic ellipsometry.

APPENDIX B

COLOR RETENTION TIME TESTS

The color retention time was also investigated by following experiments. Briefly, a 'Cactus' was printed on two dielectric-coated silver substrates with exactly the same film thicknesses (150 nm sputter-deposited SiO_2 on 85 nm evaporated Ag), then 50 nm PMMA was spin-coated on one of them as an encapsulation layer. The microscopic images and reflectance spectra were taken immediately after color printing and after 14 days, respectively. The samples were stored in ambient conditions during the whole experiment. The sample without an encapsulation layer showed a slightly faded color after 14 days (Figure B.1(a)). From the reflectance spectra, the smaller modulation depth in the visible wavelength was found after 14 days due to oxidation of printed silver, which corresponded to a less vivid color (Figure B.1(c)). On the other hand, the sample with an encapsulation layer still exhibited vivid color after 14 days in ambient conditions (Figure B.1(b)). Although the reflectance spectra indicated a slight red shift, probably due to the additional reaction between AgNPs and PMMA [131], the modulation depth was observed to be similar to the pristine color, which implied that the color was well preserved by an encapsulation layer. Interestingly, the spin-coated PMMA layer not only acted as an encapsulation layer but also increased color saturation behavior. Further investigation into the impact of various encapsulation layers on the color saturation and retention time will be studied.

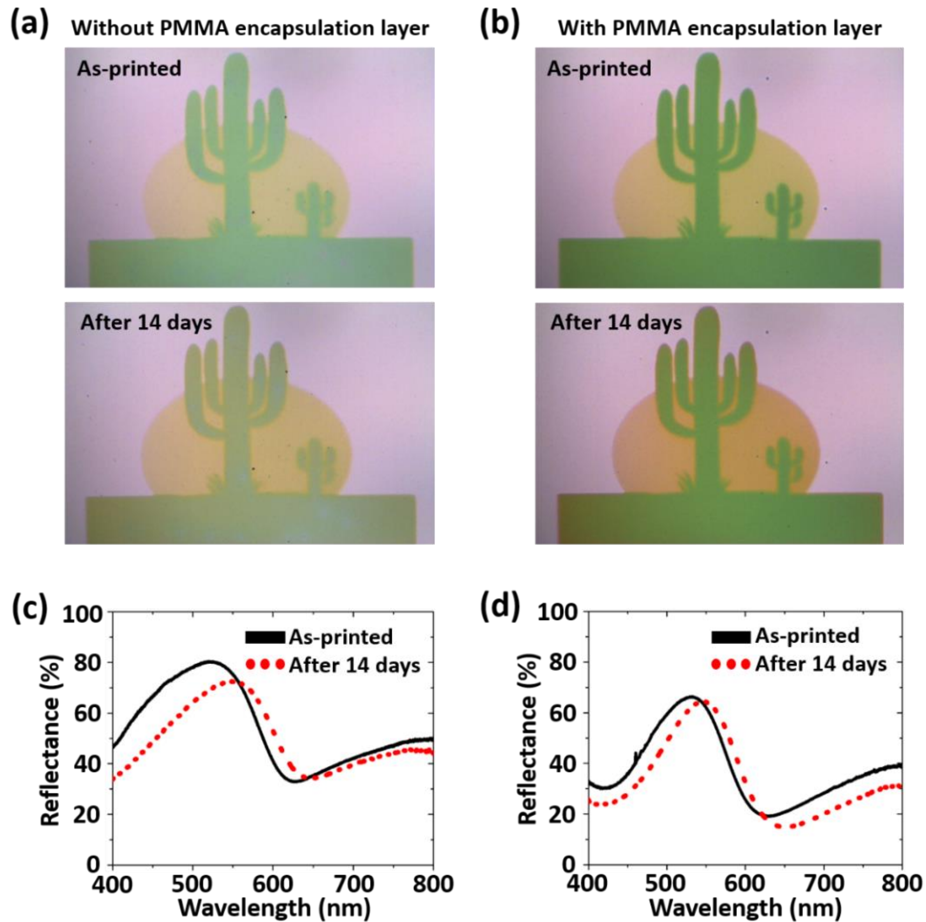

Figure B.1: The effect of encapsulation layer on color retention time. The microscopic images of printed 'Cactus' (a) without PMMA encapsulation layer and (b) with PMMA encapsulation layer. The measured relative reflectance of (c) without PMMA encapsulation layer and (d) with PMMA encapsulation layer.

Reference

[131] Singho, N. D., Johan, M. R. & Lah, N. A. C., Temperature-dependent properties of silver-poly(methylmethacrylate) nanocomposites synthesized by in-situ technique. Nanoscale Research Letters, **9,** 42 (2014).

APPENDIX C

EFFECTIVE MEDIUM THEORY

In the classical model of free electron metals, the damping (γ) is determined by the scattering of the electrons with phonons, lattice defects, or impurities [132]. However, when particle size is comparable or smaller than the mean free path of the conduction electrons in the bulk material, scattering of the conduction electrons from the particle surface results in reduced effective mean free path (L_{eff}) and increased γ through the relation:

$$\gamma(L_{eff}) = \gamma_0 + \frac{Av_F}{L_{eff}} \qquad (C.1)$$

where γ_0 is the electron relaxation rate in the bulk material, v_F is the Fermi velocity and A is a dimensionless fitting parameter related to scattering [133]. Take account of this phenomenon, the equation to calculate the permittivity of finite-sized metal nanoparticles (ε_{np}) must be modified as

$$\varepsilon_{np}(\omega) = \varepsilon_{bulk}(\omega) + \frac{\omega_p^2}{\omega(\omega + i\gamma_0)} - \frac{\omega_p^2}{\omega(\omega + i\gamma)}. \qquad (C.2)$$

Here, ω is the frequency of incident light, ε_{bulk} is the permittivity for a bulk material, and ω_p is the plasma frequency [134]. In our case, we assume that AgNPs have spherical shape, hence the modified effective mean free path ($L_{eff} = 0.82R$, where R is the radius of nanoparticle) is used for the calculation [135]. Figure C.1 shows ε_{np} of spherical AgNPs with various radius. In the visible wavelength range, the particle size effects are more

strongly manifested in the imaginary part, while the real part indicates a very minimal differences. Since our PPD film acts as the absorbing material in the FP cavity, it is important to have better understanding of the correlation between particle size and permittivity which is closely related to the absorbance of materials.

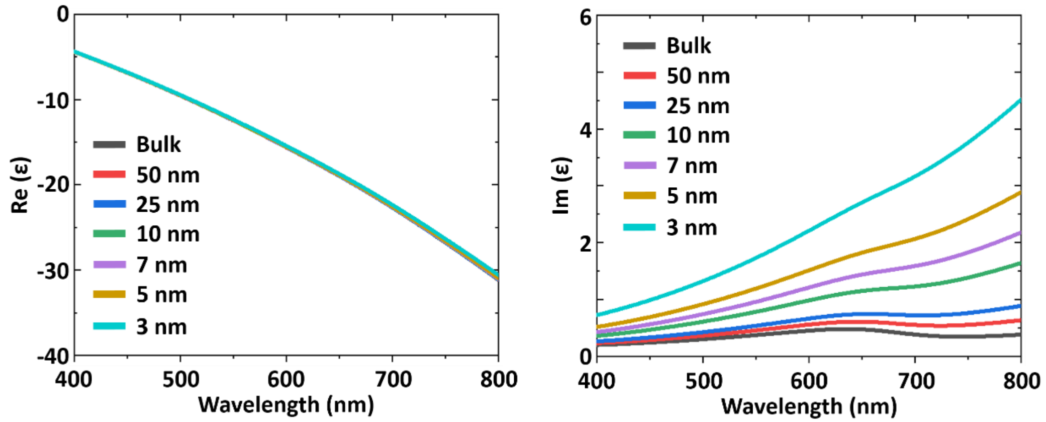

Figure C.1: Size-dependent complex permittivities of spherical AgNPs as a function of wavelength. Left: Real part. Right: Imaginary part.

Effective medium theory (EMT) has been widely used to characterize optical properties of inhomogeneous materials, e.g. metal/polymer nanocomposites [136]. Maxwell-Garnett introduced a separated-grain structure whose inclusion material is dispersed in a continuous host material, while Bruggeman suggested an aggregate structure which is filled with random mixture of the two constituents [137]. Since the reduction and polymer-assisted aggregation of AgNPs occur simultaneously in PPD process, we employ Bruggeman`s model to calculate the effective permittivity (ε_{eff}) of PPD film. The formula for ε_{eff} reads:

$$\varepsilon_{eff} = \varepsilon_p \left[1 + \frac{f(\varepsilon_{np} - \varepsilon_p)}{\varepsilon_p + n(1-f)(\varepsilon_{np} - \varepsilon_p)}\right] \qquad (C.3)$$

where ε_p = 1.91 [138] is the permittivity of polymer (pAAm) and f is the filling factor of AgNPs in the nanocomposite [139]. The shape of AgNPs is very irregular in the real case (Figure 1.2(b)), thus a shape factor n is introduced as a fitting parameter to generalize the equation. To investigate the average AgNP size, we performed pAAm concentration dependent PPD printing. From the SEM images with various pAAm concentration (Figure C.3), we observed particles from < 5 nm to 10 nm with distinguishable contrast, particularly in 30 mM of pAAm concentration, which probably attributed to higher pAAm capping efficiency for AgNPs (Figure C.3(e)). Therefore, the average size of AgNPs was set as 10 nm in diameter for the purpose of calculating ε_{np} using our model. The measured complex permittivity ($\varepsilon_m = \varepsilon_{re} + i\varepsilon_{im}$) of PPD film is obtained from the extracted spectroscopic ellipsometry data (Figure 2.2(d)) through the relations, $\varepsilon_{re} = n^2 - k^2$ and $\varepsilon_{im} = 2nk$ for real and imaginary part, respectively. Figure C.2 shows ε_m and ε_{eff} of PPD film according to f, where n is set as 4.1. Importantly, when f is 0.81 (short-dotted pink line), calculated ε_{eff} is comparable to measured ε_m, which implies highly concentrated AgNPs in the PPD film. Consequently, those densely packed AgNPs absorb significant amount of incident light, which yields strong modulation of reflectance spectra in the visible wavelength range.

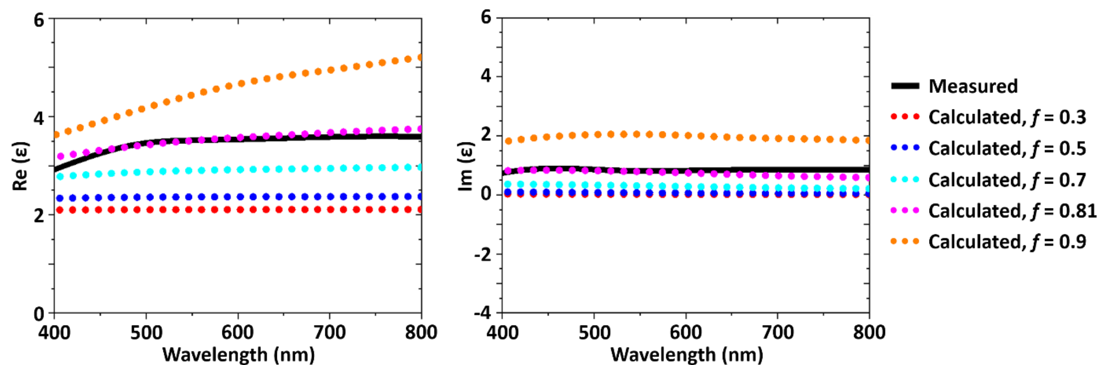

Figure C.2: Measured complex permittivity (solid line) and calculated effective permittivity (dotted line) of AgNPs/pAAm nanocomposites as a function of wavelength. Calculation performed according to filling factor *f*. Left: Real part. Right: Imaginary part.

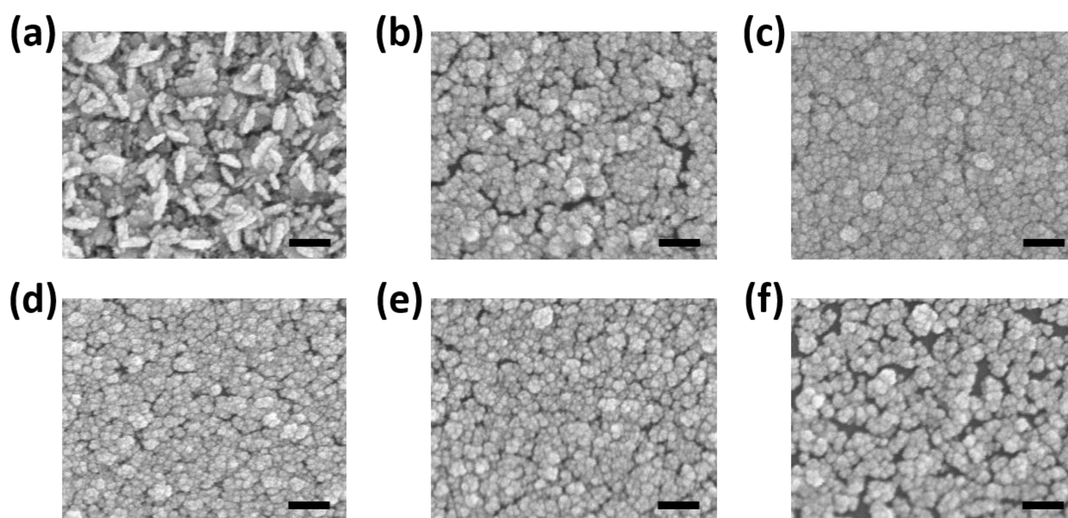

Figure C.3: The effect of pAAm concentration on PPD film. (a) 0 mM, (b) 10 mM, (c) 16 mM, (d) 20 mM, (e) 30 mM, and (f) 40 mM of pAAm was mixed in Ag precursor solution, respectively, for printing PPD film (scale bar: 100 nm).

Reference

[132] Vollmer, M. & Kreibig, U. Optical Properties of Metal Clusters 1st edn, vol. 25 (eds Toennies, J. P.) Ch. 2 (New York: Springer, 1995).

[133] Coronado, E. A. & Schatz, G. C. Surface plasmon broadening for arbitrary shape nanoparticles: A geometrical probability approach. Journal of Chemical Physics, **119**(7), 3926-3934 (2003).

[134] Barma, M. & Subrahmanyam, V. Optical absorption in small metal particles. Journal of Physics: Condensed Matter, **1**(41), 7681-7688 (1989).

[135] Cai, W. & Shalaev, V. Optical Metamaterials: Fundamentals and Applications 2010th edn, Ch. 2 (New York: Springer, 2010).

[136] Niklasson, G. A., Granqvist, C. G. & Hunderi, O. Effective medium models for the optical properties of inhomogeneous materials. Applied Optics, **20**(1), 26-30 (1981).

[137] Bardini, L., Ceccato, M., Hinge, M., Pedersen, S. U., Daasbjerg, K., Marcaccio, M. & Paolucci, F. Electrochemical Polymerization of Allylamine Copolymers. Langmuir, **29**(11), 3791-3796 (2013).

[138] Rao, Y., Qu, J., Marinis, T. & Wong, C. P. A Precise Numerical Prediction of Effective Dielectric Constant for Polymer-Ceramic Composite Based on Effective-Medium Theory. IEEE Transactions on Components and Packaging Technologies, **23**(4), 680-683, (2000).

APPENDIX D

BONDING PROCESS DEVELOPMENT FOR CMOS INTEGRATION

The integrated DLCM was diced and bonded onto the customized CMOS sensor as followed by the developed bonding process to investigate its imaging performance (Figure D.1). The AZ-1505 photoresist (PR) was spin-coated on both sides of the fabricated sample with an acceleration speed of 2000 rpm as a protection layer during the dicing process and post-baked 1 min at 90 ℃ on the hot plate, then the sample was diced into 7.2 mm × 5.6 mm rectangular shape using a dicing saw (DAD320, DISCO Corporation). After dicing, the sample was immersed in acetone to remove PR, rinsed in IPA, and dried with nitrogen blow. The thin PDMS film was delaminated from a commercially available Gel-box and attached to the 4-inch borosilicate substrate using spontaneous bonding as an intermediate layer, then the sample was placed on the film. Since the PDMS was sticky enough to hold the sample during the bonding process, it was not required to use any additional materials for sample mounting, which would potentially leave undesired residues on the sample surface. A customized CMOS sensor was brought together with a printed circuit board (PCB) [106]. Glass slides were cut, multi-stacked, and fixed using double-sided tape on the 4-inch Si wafer as the CMOS PCB supporting layer to maintain the surface evenness during the bonding process since the backside of PCB was not flat due to several protruded electrical components. For the CMOS bonding process, another UV resist (B-UV resist) was prepared by adding the monomer (SR-9003-B), oligomers (CN-292 and CN-975), cross-linker (Octadecyl acrylate), the surface additive (1*H*,1*H*,2*H*,2*H*-Perfluoro-1-decanol BYK-3570), and photoinitiators (Omnirad 1173 and Omnirad TPO) into IBMA solvent to improve cross-linking efficiency and bonding strength. The CMOS PCB was mounted on the glass slides using Kapton tape, then 90 wt% B-UV resist was spin-coated on the CMOS with an acceleration speed of 3000 rpm. Then, the mounted sample and spin-coated CMOS

PCB were loaded into the mask aligner (MJB4, Suss MicroTec) to perform the bonding process. After precise alignment of the sample and CMOS using x, y, and θ knobs, the CMOS PCB was moved up in the z-direction and made contact with the sample, which initiated the flow of resist between them. Once the resist fully flowed on the surface, the resist was cross-linked under the UV exposure (365 nm, 350 W) for 10 min to accomplish appropriate bonding between the sample and the CMOS sensor.

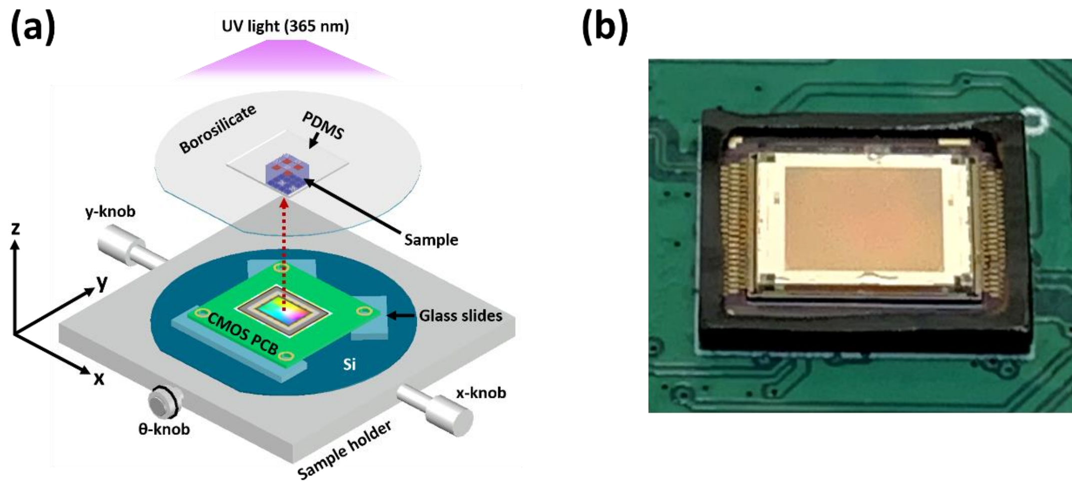

Figure D.1: Developed CMOS bonding process. (a) Conceptual 3D schematic illustration of the CMOS bonding process using mask aligner. (b) Photographic image of the fabricated sample bonded onto CMOS image sensor.

APPENDIX E

PERMISSION FOR PREVIOUSLY PUBLISHED WORK IN A CULMINATING EXPERIENCE DOCUMENT

Previously published and/or publishable work has been used in the preparation of this dissertation. All co-authors have been granted permission to reuse the corresponding contents in the current document. Appropriate citations and acknowledgments are also inserted in the document whenever applicable.